Wetting and Heat transfer in Graphene-Based Composites - Multiscale Molecular Simulations

Dissertation
Vikram Reddy Ardham
Darmstadt, 2018 – D17

TECHNISCHE
UNIVERSITÄT
DARMSTADT

Wetting and Heat transfer in Graphene-Based Composites – Multiscale Molecular Simulations

vom Fachbereich Chemie
der Technischen Universität Darmstadt

zur Erlangung des Grades

Doctor rerum naturalium
(Dr. rer. nat.)

Dissertation
von Vikram Reddy Ardham

Erstgutachter	:	Prof. Dr. Florian Müller-Plathe
Zweitgutachter	:	Prof. Dr. Nico van der Vegt

Darmstadt 2018

Tag der Einreichnung	:	05. Februar 2018
Tag der mündlichen Prüfung	:	20. März 2018

The current PhD thesis has been conducted under the supervision of P.D. Dr. Frédéric Leroy and Prof. Dr. Florian Müller-Plathe of the Eduard-Zintl-Institut für Anorganische und Physikalische Chemie at the Technische Universität Darmstadt. The research has been partly conducted in collaboration with Prof. Dr. Nico van der Vegt of the same department. This work is a part of the Sonderforschungsbereiche und Transregio (SFB TRR)146, titled "Multiscale Simulation Methods for Soft Matter Systems" funded by the DFG. The research activity conducted during this thesis resulted in the following journal articles in peer-reviewed international journals (in reverse chronological order).

1. **Ardham, V. R.**; Leroy, F., Atomistic and Coarse-Grained Modeling of the Adsorption of Graphene Nanoflakes at the Oil-Water Interface, *J. Phys. Chem. B*, **2018** (*accepted*).

2. **Ardham, V. R**.; Leroy, F., Communication: Is a Coarse-grained Model for Water Sufficient to Compute Kapitza Conductance on Nonpolar Surfaces? *J. Chem. Phys*, **2017**, *147*(15), 151102.

3. **Ardham, V. R.**; Leroy, F., Thermodynamics of Atomistic and Coarse-grained Models of Water on Nonpolar Surfaces, *J. Chem. Phys,* **2017**, *147*(8), 074702.

4. **Ardham, V. R.**; Deichmann, G.; van der Vegt, N. F. A.; Leroy, F., Solid-liquid Work of Adhesion of Coarse-grained Models of *n*-hexane on Graphene Layers Derived from the Conditional Reversible Work Method, *J. Chem. Phys.* **2015**, *143*(24), 243135.

The above research articles have been reproduced as chapters 4, 5, 3 and 2 respectively, in this thesis.

Zussamenfassung

Grenzflächen haben in einer Reihe von Materialien Ausdehnungen im Nanometerbereich und spielen typischerweise eine Schlüsselrolle für die Eigenschaften von Verbundmaterialien. Das Verständnis der Thermodynamik und der Wärmeübertragung durch die Grenzflächen ist eine entscheidende Herausforderung für das Design und die Konstruktion von Verbundwerkstoffen. Zum Beispiel wurden graphenhaltige Polymerverbundwerkstoffe häufig verwendet, um die thermischen Eigenschaften um Größenordnungen zu verbessern. Sie haben aber die hohen Erwartungen, hauptsächlich aufgrund des thermischen Widerstands an der Grenzfläche, noch nicht erfüllt. Die Simulation dieser Systeme bietet sicherlich die Möglichkeit, wertvolle Einblicke in die Physik an der Schnittstelle zu gewinnen und einige offene Fragen zu beantworten.

Die Simulation dieser Systeme ist jedoch nicht trivial und erfordert die Überwindung von zwei großen Hürden. Das erste Problem besteht darin, dass die Schnittstelle mit geeigneten Modellen korrekt beschrieben werden muss, um einen realistischen Vergleich mit den Experimenten durchzuführen. Zweitens gibt es ein Skalenproblem; wenn man versucht, diese komplexen Systeme mit der höchsten Auflösung in allen chemischen Details zu modellieren, erstrecken sich die relevanten physikalischen Probleme oft über Längen- und Zeitskalen, die außerhalb der gegenwärtigen Rechenleistungen liegen. In dieser Doktorarbeit befasse ich mich mit den beiden oben genannten Problemen, mit der genauen Beschreibung der Wechselwirkung zwischen den Komponenten und damit, wie man vergröberte Modelle dafür ableitet. Dadurch erhalten wir ein detailliertes Verständnis darüber, welche Veränderungen die vergröberte Darstellung an den Fest-Flüssig-Grenzflächen bewirkt.

Die vorliegende Dissertation zielt darauf ab, ein grundlegendes Verständnis der Fest-Flüssig-Grenzflächen zu erlangen und ein Verfahren vorzuschlagen, das die Simulation großer Systeme von Teilchennetzen ermöglicht, die von einer fluiden Komponente umgeben sind. Zu diesem Zweck befassen wir uns zunächst mit Details der Grenzflächenthermodynamik, indem wir Fest-Flüssig-Grenzflächen von graphenhaltigen Systemen untersuchen. Dann erweitern wir diese Studie auf vergröberte Flüssigkeitsmodelle, um im Detail zu untersuchen, wie sich das Grenzflächenverhalten dadurch verändert. Wir beobachten vor allem, dass der entropische Anteil der freien Energie durch diese Art der Auflösung nicht genau reproduziert wird. Wir haben gelernt, dass zur präzisen Darstellung der Schnittstellen sowohl die Wechselwirkungsenergie als auch ihre Fluktuationen reproduziert werden müssen.

Mit diesen Erkenntnissen schlagen wir einen Ansatz vor, um Graphenpartikel an der Wasser-Öl-Grenzfläche zu simulieren. Unter Verwendung des makroskopischen Benetzungskoeffizienten als relevanten Parameter wurde ein einfacher Ansatz zur Ableitung von Fest-Flüssig-

Wechselwirkungselementen vorgeschlagen und getestet. Durch Simulationen mit verscheidenen Werten des Benetzungskoeffizienten konnten wir bestätigen, dass die Bedingungen für die Adsorption von Teilchen mit makroskopischen Vorhersagen übereinstimmen. Es wird weiter gezeigt, dass der vorgestellte Ansatz für atomare und grobe Auflösungen von Flüssigkeiten gleich gut funktioniert.

Im nächsten Schritt wurde eine detaillierte Studie zum Einfluss der Wasser-Grobkörnung auf den Wärmeübergang über Wasser-Graphit-Grenzflächen durchgeführt. Durch die Berechnung der Grenzflächenwärmeleitfähigkeit (G) haben wir die Unterschiede in der Wärmeübertragung für atomare und grobe Auflösung von Wasser bei unterschiedlichen Benetzungsstärken untersucht, die von hydrophob bis schwach hydrophil reichen. Ziemlich überrascht beobachten wir, dass ein vergröbertes Modell von Wasser ausreichend ist, um G zu berechnen. Diese wichtige Erkenntnis bedeutet, dass die Wärmeübertragung über die Fest-Flüssig-Grenzfläche hauptsächlich im Niederfrequenzbereich stattfindet und Hochfrequenzmoden (oder Freiheitsgrade), die durch eine Vergröberung entfernt werden, nur einen geringen Einfluss haben.

Die obigen Erkenntnisse werden uns in die Lage versetzen, komplexe Systeme (bis zu 100 nm) von Graphen an Wasser-Öl-Grenzflächen zu modellieren und uns weiterhin ermöglichen, den Wärmetransfer über Teilchennetzwerke zu charakterisieren. Die hier durchgeführten Computerstudien könnten die Bemühungen zur Entwicklung von Ansätzen in der Multiskalenmodellierung vorantreiben und dazu beitragen, offene Fragen im Bereich des Wärmetransfers und der Selbstorganisation in Polymernanokompositen zu beantworten.

Summary

Interfaces are ubiquitous at the nanoscale in a range of materials and typically play a key role in determining the composite material properties. Understanding the thermodynamics and heat transfer across interfaces is a crucial challenge in composite material design and engineering. For instance, graphene-based polymer composites have been hyped to render orders of magnitude enhancement in thermal properties but have not yet lived up to the promise, primarily due to the thermal resistance arising at the interface. Simulating these systems certainly provides a way to gain valuable insights into physics at the interface and can answer some outstanding questions.

However, simulating these systems is non-trivial and offers two major hurdles. The first issue is that the interface must be properly represented using suitable models to perform a realistic comparison with the experiments. The second problem is that of the scale, i.e., if one aims to model these complex systems at the highest resolution with all the chemical details inserted, the relevant physical problems often span length and time scales that are out of reach of the state of the art computational power. We address the above two problems in this thesis, i.e., how to represent interactions between various species faithfully and two, how to derive coarse-grain models accordingly. Furthermore, we also obtain a detailed understanding of what changes coarse-graining brings to the solid-liquid interfaces.

The current thesis aims to obtain a fundamental understanding of the solid-liquid interfaces and to propose a framework that allows simulation of large systems of particle networks surrounded by a fluid component. To this end, we first address the nature of interfacial thermodynamics by studying solid-liquid interfaces of graphene-based systems. Then we extend this study to coarse-grained models of liquids to study in detail how the interfacial behavior is modified on coarse-graining. We primarily observe that the entropic part of the free energy is not accurately reproduced up on coarse-graining. We have learnt that, to accurately represent the interfaces, one needs to reproduce both the interaction energy and its fluctuations.

Using these insights, we propose an approach to simulate graphene particles at the water-oil interface. By relying on the macroscopic wetting coefficient as the relevant wetting parameter, a simple approach to derive solid-liquid interaction parameters was proposed and tested. By simulating at various values of the wetting coefficient, we were able to confirm that the regime, for which the particles adsorb, is consistent with the macroscopic predictions. It is further shown that this approach works equally well for atomistic and coarse-grained models of liquids.

In the next step, a detailed study on the influence of water coarse-graining on the interfacial heat transfer across water-graphitic interfaces has been conducted. By computing the interfacial thermal conductance (G), we evaluated the differences in heat transfer for atomistic and coarse-grained water at different strengths of wetting ranging from hydrophobic to mildly hydrophilic. Quite surprisingly, we observe that a coarse-grained model of water is sufficient to compute G. This important insight means that, heat transfer across solid-liquid interface is mainly in the low frequency regime and removing high frequency modes (or degrees of freedom) by coarse-graining has only a nominal influence.

The above insights will enable us to model large scale systems (up to 100nm) of graphene at water-oil interfaces and further will allow us to characterize heat transfer across networks of particles. The computational studies performed here will further the efforts to develop approaches in multiscale modeling and will assist in addressing outstanding questions in the areas of heat transfer and self-assembly in polymer nanocomposites.

Table of Contents

CHAPTER # 1

1.1 Motivation

Polymer nanocomposites (PNCs) are an interesting class of materials that opened new avenues like flexible electronics, advanced prosthetics, transparent conductive films, and self-healing materials. Even in modern electronics, PNCs with their tunable conductivities (both thermal and electrical) gained significant importance. For instance, Moore's law,[1,2] advent of the novel computing architectures (like three-dimensional[3] and neuro-morphic[4–6] architectures) have resulted in a great surge in transistor density (several 100 billion/mm^2) in computer microprocessors. For shrinking components as well high-density architectures, efficient dissipation has remained a severe bottle neck[7,8,9] for any serious practical implementation or industrial scaleup. Polymer nanocomposites appeared to be tailor-made choices as thermal interface materials (TIMs) to channel efficient heat dissipation,[10,11] so as to avoid over-heating or even melting of the computer chips. Particularly, graphite[12] and carbon nanotube (CNT)[13,14] based materials appear to be a natural choice, as they seemingly combine the positive features of both nanoparticles (high thermal/electric conductivity >10^5 times that of polymers)[15] and polymers (low density, cost and high mechanical flexibility)[16] while discarding undesirable features of each.

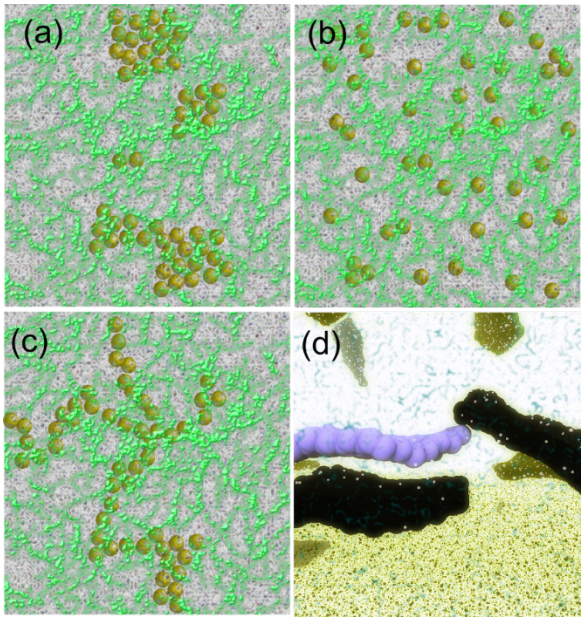

Figure 1. Artistic rendering of a polymer nanocomposite, where particles (a) form aggregates (b) are well dispersed (c) form inter-connected networks. (d) shows a close-up rendering of particle connectivity obtained from molecular dynamics simulations.

However, studies revealed that, the composite thermal properties are rather meek (up to tens of percent points) and far from the predictions made by the effective medium theories.[17,18] This lead to the belief

that the cumulative properties obtained by fusing polymers and nanoparticles together, are not a trivial mean of the properties but arise from a complex interplay of structural and mutual interaction strengths. For instance, the presence of contrasting phonon density of states at the interface between polymer and nanoparticle result in poor vibrational coupling,[19] added channels of scattering and consequently to poor heat transfer across the interface. The interfacial resistance depends on the nature and strength of the interaction between the polymer and nanoparticle, the interfacial structure, and roughness among other things.[20,21] In general, the properties of nanocomposites are a direct function of the spatial distribution of nanoparticles embedded in the polymeric system, and the interaction strengths among each of the species involved. As depicted in Figure 1, depending on the mutual interaction strengths the particles might from conglomerates (Figure 1a), disperse well within the polymer matrix (Figure 2a) or the particles might form a network like arrangement (Figure 3a). A typical interface formed between nanoparticles and the surrounding fluid is shown in Figure 1d. The image illustrates the complex structures and interactions that are at play. In the next section, we dig a little deeper into the heat transfer mechanisms through the interface and challenges that need to be overcome.

1.2 Physics at the interface

Heat transfer in crystal materials and polymers takes place through very different mechanisms.[22] Crystals have well defined periodicities and heat propagation takes place via the pseudo particles known as phonons.[23] Phonons correspond to allowed discrete vibrational modes in a periodic system. Phonons behave very much like a wave, they propagate, superpose with one another and scatter, transferring energy in the process. In low dimensional materials[24] like CNTs[25,26] and graphene,[27] the phonons possess unique features, like large mean free paths (100s of nm due to the absence of any scattering channels), ultra-high group velocities (>10^4 m/s, owing to the strong sp^2 C-C bonds) making them highly conductive (up to 2000-5000 W/mK). Most of the unusual properties in these carbon allotropes arise from the flexural acoustic modes known as ZA modes.[28] These vibrational modes characterizing conductivity are given by the dispersion curves and are dependent on the atomic interactions and coordinates. Typically this information is obtained by modeling Phonon interactions and propagations through Boltzmann transport equation (BTE)[29] or non-equilibrium Green's function.[30,31]

In contrast, theory of thermal properties in liquids (either heat capacity or thermal conductivity) or amorphous polymers is not well established so far. Heat transfer in liquids is dominated by weak intermolecular interactions leading to low group velocities and thermal mean free paths resulting in a diffusive means of transport (as opposed to ballistic). Resolving heat transfer in liquids into various

vibrational modes reveals localized bonded vibrations, vibrations arising from van der Waals (vdW) interactions and hydrogen bonds to be the major carriers of heat.[32,33,34,35] An important feature of these vibrations is that, they are all localized modes having short mean free paths and therefore result in low values of thermal conductivities in liquids. These several different vibrational modes are separable into two regimes based on their frequencies relative to the Frenkel frequency (ω_F). The modes having frequencies greater than ω_F are strictly localized vibrations and the remaining low frequency vibrations could be treated as diffusion like modes. In the recent years, a phonon theory of liquid thermodynamics[36,37] has been proposed relying on the above distinctions and paved a way for a complete and satisfactory theory of heat transfers in liquids too.

Considering the contrasting features of heat transfer mechanisms in solid and liquids, it is indeed not straightforward to predict or explain the observed enhancement in thermal properties in nanocomposites that feature solid-liquid interfaces (the term solid-liquid interface will be used interchangeably with nanoparticle-polymer interface). In fact, various mechanisms have been proposed to address the conductivity enhancement in nanofluids, explanations ranging from Brownian motion based mechanisms, formation of nanolayers, heat transfer aided by thermal diffusion, enhancement produced by particle-particle collision to mechanisms proposing heat channeling through percolation network of particles.[38–41] However, in polymer based composites, there is little to no fluid motion and the entire conductivity enhancement can be attributed to the formation of percolation networks.[22,42–45,46,47] These percolation networks of particles theorized to channel heat or electrons effectively and enhance conductivity are now arguably the most dominant pathways to heat transfer. The conductivity in these composites was found to follow a scaling law with concentration of the nanoparticles as predicted by the percolation theories,[45,48,49] buttressing the idea of percolation further. Therefore, these network formations raised curiosity and renewed interest in synthesizing conductive polymer nanocomposites. Boosted by the idea of percolation phenomenon, several papers[47,49–57] appeared in the literature in the past few years reporting significant enhancement of up to an order of magnitude in the composite conductivity.

However, it was observed that there was a striking change in the magnitude of electric conductivity at percolation threshold but the same was not seen in case of thermal conductivity.[42] In fact, thermal conductivity showed only a slight jump whereas electric conductivity has shown an increment of a few orders of magnitude. The difference can be qualitatively explained by comparing the transmission probabilities[58] that determine the conductance across an interface. Heat transfer requires perfect matching of vibrational modes across the interface between polymer and nanoparticle (which have contrasting vibrational modes) and large contact areas between nanoparticles, which means very low probability of transmission. Whereas, electron transmission probabilities across an

interface are close to unity. An alternative explanation was provided by Shenogina and coworkers,[18] who pointed out that the ratio of electric conductivities of nanoparticle and polymer is very high (>10^{12}) when compared to the ratio of thermal conductivities (~10^{4}). Based on continuum heat transfer models, this difference in ratio was shown as a possible mechanism for the lack of thermal percolation. Although the above explanations provide qualitatively satisfactory explanation, a quantitative one is lacking as the detailed mechanisms of heat transfer through networks of particles embedded in polymers is still missing.

Therefore, the key mechanisms to explain the above discrepancy and to attain deeper understanding of the heat transfer lie at the interface. Several studies have revealed the importance of the interface, its role in determining the thermal conductance and how it could be tuned.[20,21,59–70] Hence, to obtain detailed understanding of heat transfer across a network of particles using simulations, one needs to model the interfaces accurately, which forms the central topic of this thesis.

Another issue that arises often while synthesizing networks of graphene, carbon nanotubes or other low dimensional materials is that the materials must be appropriately functionalized to achieve proper dispersion. As already well known, functionalization leads to defects in these pristine 2D materials with unique properties, ultimately leading to scattering and unwanted dissipations. To overcome the issue of functionalization, plenty of research groups resorted to self-assembly at liquid-liquid interfaces. Immiscible liquid-liquid interfaces are highly energetic (water-oil interface has a surface tension of about 50 mJ/m^2 at room temperature) and are ready to be replaced by particles that tend to lower the overall free energy. Therefore, when nanoparticles are introduced at such interfaces, they act as surfactants and readily migrate to the interface. Self-assembly of few layer graphene and graphene oxide at water-oil interfaces have been particularly exploited a lot experimentally to synthesize very thin conducting films of nanoparticles that could later be used as a template to be further down processing in polymer nanocomposites. Interfacial self-assembly arises from the subtle balance of interactions arising from different interfaces and requires that these balances be reproduced faithfully.

Both the above requirements, i.e., understanding heat transfer across the interfaces and attaining self-assembly at liquid-liquid interfaces, demonstrate the need for faithful representation of the solid-liquid interfaces. It is evident that further investigations are necessary to understand the nature of connectivity among the particles, to achieve greater control over the formation of these networks and ultimately to assist proper selection of the materials to manufacture composites with desirable properties. Molecular simulations can be of considerable avail to address problems at this scale. They have been proven to provide fundamental insights into the microscopic structures, formations of dispersed particles by allowing us to take a deeper look. However, the above problems discussed

cannot simply be modelled at a single scale owing to the many time and length scales that need to be addressed. To this end, we discuss multi-scale modeling in the next section.

1.3 Multi-scale modeling

1.3.1 Continuum models

Continuum models typically address problems at the macroscopic scale (μm-m) although at a very low resolution. Continuum approaches have proven to be useful to solve well-established partial differential equations (PDEs) with complex boundary conditions. At the nanoscale continuum approximations break down and therefore, continuum-based models usually introduce tunable effective parameters (like thermal resistance) to represent interfaces. A few continuum-based methods have so far been applied to study heat transfer problems and compute effective thermal conductivity of nanocomposites. In Finite element[71,72] based or Monte-Carlo[73] based techniques, the interfacial resistance between the solid and liquid is taken as an input quantity and while assuming a distribution of nanoparticles of certain shapes and sizes, the effective conductivity of the composite was evaluated based on a simple heat transfer model. Continuum methods were also coupled with the atomistic simulations by representing certain regions at atomistic resolution and remaining regions at low continuum resolution.[74] In addition, analytical effective-medium theories with fitting parameters have been used to interpret composite conductivity.[75,76,77] In either of the above-mentioned methods, information obtained at the atomistic scale is crucial and continuum methods alone cannot be applied to study heat transfer at the nanoscale.

1.3.2 Particle-based models

Molecular simulations have not only enhanced our understanding of the equilibrium properties, but they are able to provide profound insight into systems driven by non-equilibrium processes as well. Furthermore, these simulation tools (Molecular Dynamics (MD) to Dissipative Particle Dynamics (DPD)) allow us to study the dynamic transport properties of complex systems and to gain a deeper understanding of various driving forces in action at the nm-μm regime.

Particle based simulations is an umbrella term that includes a wide variety of simulation methods spanning different length scales and resolutions, ranging from ab-initio MD (sub nm) to all the way up to DPD and Smooth Particle Hydrodynamics (SPH) which deal with problems at the macroscale (from μm to all the way up to intergalactic scale). Below we discuss few examples from the literature where particle-based simulations provided valuable insights into self-assembly and thermal transport at the nanoscale.

	Nature of interactions	Typical models/methods	Resolution
0	Solution of Schrödinger's wave equation – particles are waves	Electron density based functionals/ Plane waves	The smallest resolution
1	Intramolecular–very strong SR	harmonic potentials, many-body	AT, CG
2	Electrostatic – strong, LR	Inverse square law	AT, CG
3	Dispersion interactions – weak, SR	Lennard-Jones potential	AT, CG
4	Colloidal – weak, SR	Yukawa potential, Hamaker based	Mesoscale
5	Fluctuating Hydrodynamic	DPD, SPH, LLNS	Mesoscale
6	Hydrodynamic	CFD (FE, FV, FD)	Macroscale

Table 1. Summary of various interactions, typical models used and applied resolutions. The numbering on the column loosely indicates the increasing length scale at models are relevant. AT refers to fully atomistic level, CG is coarse-grained, SR is short-ranged, LR is long-ranged, SPH is Smoothed Particle Hydrodynamics, CFD is computational fluid dynamics, FE, FV and FD refer to Finite-element, volume and difference methods respectively. LLNS refers to the Landau-Lifshitz-Navier-Stokes equation.

Self-assembly phenomenon

Studies on self-assembly of spherical nanoparticles[78,79,80] embedded in a polymer matrix revealed that, by tuning various interaction strengths one can easily control the amount to which the particles disperse or aggregate. Studies have been extended to morphologies other than spheres[81,82] and by functionalizing nanoparticle surfaces or polymers with chains of atoms.[83,84] In an interesting study self-assembly of ionic nanoparticles was studied at the oil-water interface.[85] These studies revealed to us that various configurations of particles that control the properties of the composite can be easily tuned by changing the interactions, morphologies and functionalizations. The above studies were limited to model systems and studies on more realistic systems were performed to understand how solvent influences particle dispersion by computing the exfoliation properties.[86–91] Exfoliation energy and potential of mean force profiles for particles in a solvent provide excellent guides to choosing a suitable solvent to obtain a chosen spatial distribution of particles. The above systems had to be limited to small simulation domains and limited number of nanoparticles due to serious computational constraints. Large networks of CNTs (up to 1.5 million particles) were simulated to perform electrical conductivity studies recently,[92] however by using generic models for polymers and CNTs based on a self-consistent field approach. There also have been attempts to simulate composite systems of

multiple graphene sheets in polymers to understand the dynamics, structural properties and dispersion of graphene sheets[93–97], but only with limited success.

Thermal transport phenomenon

When heat transfers across an interface, a temperature drop occurs at the interface due to the presence of the interfacial thermal resistance (ITC). Several studies have tried to address the problem of solid-liquid interfacial heat transfer using non-equilibrium molecular dynamics simulations (NEMD) and evaluating the Kapitza resistance[98] (or conductance) of an interface. Kapitza resistance is a quantity that characterizes how effectively an interface conducts heat and is given by the ratio of temperature drop across the interface to the heat flux. Studies indicated that grafting self-assembled monolayers (SAMs)[33,99] can facilitate effective heat transfer from a rigid solid phase to the soft polymer phase. Also, addition of covalent functionalisations[62,69,100,101] to the surface was found to add new pathways for thermal transport although degrading the intrinsic conductivity of the nanoparticle. It was also found that the Kapitza conductance increases with work of adhesion.[21,101,102,75–77] Although, certain works propose the trend to be linear, it was found to be only so in a rather narrow regime.[103] More recent studies on nanoparticle-polymer interfaces revealed in detail the mechanisms of heat transfer and addressed the influence of parameters like wetting strength, relative orientation of the polymers, roughness of the contact, direction of heat transfer, bonding at the interface etc.[104,105,106–108,109] The above studies enhanced our understanding of the interfacial heat transfer to a great deal and hinted at possible pathways to tune the conductance. However, all the above-mentioned studies were limited to rather simple model interfaces where an interface was studied alone under strict isolation from the bulk composite. A study on complex and realistic network of particles, with several particles that accounts for the resistance at the solid-solid contacts and considering how these contacts evolve over time is missing.

As the above examples clearly illustrate, simulations have either been performed at large scale but with model systems or at a small scale with complex systems. It is now clear that, although a lot has been achieved and a great deal has been understood with respect to the assembly and heat transfer in polymer nanocomposites a lot more remains unexplored. Especially, questions related to the formation of nanoparticle networks, the parameters controlling these formations, their detailed structure, and the corresponding heat transfer through these particles remain unanswered. Addressing these questions requires both chemical specificity and large simulation sizes. One such way is to perform systematic coarse-graining, which will be the topic of the next section.

1.4 Coarse-graining

Coarse-graining is procedure followed to represent the atomistic system at a lower resolution by removing irrelevant degrees of freedom and to derive the corresponding effective interactions or potentials. As we discussed in section 1.3.2, there are various kinds of interactions that must be dealt with, if one aims to capture the thermodynamics and dynamics of the system accurately. The absolute number of interactions scales with the square of the particle number, the computation time typically scales linearly with the particle number (for a given cutoff distance) and as a result the computation time scales with the cube of the volume of the simulation cell. This puts serious limitations on the systems sizes and time lengths we can access in a particle-based simulation. Moreover, due to the presence of such a large number of interactions the potential energy landscape is quite rugged, and the system is very likely to be kinetically trapped for the computationally feasible time scales. To mitigate the above two problems, a strategy that is being increasingly applied is the process of systematic coarse-graining. The idea of coarse-graining is to lump a group of atoms and represent it as one single bead (an interaction site), effectively reducing the number of interactions. For example, the C-H vibrations in alkyl groups and the O-H vibrations in water have a minimal impact on the overall conformational properties of a protein and thus can be easily ignored and the respective groups may be combined into one heavy bead. In cases, where intra monomer interactions are not important, each monomer in a polymer could just be represented by a single bead. There is an essential loss in information when a certain number of degrees of freedom are removed, and the models derived using coarse-graining cannot in principle reproduce all the characteristic features of an underlying atomistic model.

Coarse-graining procedure essentially consists of two steps, one is to choose a mapping or representation on which atoms to be combined and represented as a single unit. Followed by a second step, where the interactions between the newly defined beads must be parametrized to reproduce certain physical properties of the reference system. Various choices exist at each of these steps depending on what information one is interested in retaining. The so obtained coarse-grained model not only reduces the degrees of freedom of the model but also smoothens the potential energy surface allowing faster sampling of the configurational space. However, it is not always clear when a coarse-grain model is derived by reproducing a certain property (say structure) up to a certain level of accuracy, which properties of the model stay close to their reference values and which properties don't. So, coarse-graining is a highly non-trivial process and must be applied by paying a lot of attention to in what ways the new model differs from the parent atomistic model. Another issue with the coarse-grained models is that a model developed at a certain state point (temperature, pressure,

concentrations) cannot be directly applied to a different state point, this is called transferability and the coarse-grained models are often poorly transferable.

Nevertheless, coarse-graining is an active field, a lot of effort is being laid on addressing each of the above problems and new and efficient methods are being developed at regular intervals. Interested readers might find detailed examples in the most recent reviews on coarse-graining and its applicaations.[110–115] Some of the popular coarse-graining strategies along with the target property that is optimized are summarized in Table 2.

	Method	Target quantity
1	Iterative Boltzmann Inversion (IBI)[116]	Pair-correlation function
2	Inverse Monte Carlo (IMC)[117]	Structure
3	Force-matching[118]	Forces on each atom
4	Relative-Entropy[119]	Overlap of probability distribution
5	Conditional Reversible Work[120]	Free energy
6	MARTINI force-field[121]	Free Energy
7	Other ad-hoc procedures	Top-down approaches

Table 2. A summary of some of the most popular coarse-graining methods available in the literature, what each model tries to reproduce in addition to some examples where certain biophysical/material problems were addressed successfully.

In addition to the methods listed in the above table, it is worth mentioning two other strategies might be relevant to the current problem. Adaptive resolution[122,123] method allows switching of the resolution of the particles on the fly as they move between pre-defined high resolution and low resolution regions. Typically, the more interesting regions (closer to an interface for example) are simulated at the atomistic resolution, regions far away are dealt at a coarse-grained resolution while connecting both these regions with a mixed resolution region. Finally, a rigorous approach that can be applied is by implementing a genuine multi-scale approach, by first deriving parameters at the quantum scale, then using them to simulate atomistic systems and then transferring data from these simulations to the coarse-grained level as followed Suter and co-workers.[124]

All the above-mentioned coarse-graining methods could be classified as bottom-up methods as the information flow is from the highest resolution to the lowest resolution. An alternative heuristic approach termed as top-down method provides information flow in the opposite direction. Typically,

information from the experimental results is chosen as a target function (say collapse of a polymer or assembly of a bilayer) and the model parameters are tuned to reproduce this function. This is the hand wavy procedure typically followed by DPD models. The middle ground between top-down and bottom-up approaches is to tune the parameters of an existing model by quantitatively reproducing an experimental quantity (like free energy or contact angle), which is the strategy adopted in this work. This approach is similar to the approach taken by Suter and co-workers except that the expensive quantum computations are replaced by inexpensive and already available experimental results. In this thesis, we make use of this approach for deriving the complex solid-liquid interactions.

The primary reason for choosing this approach is that, none of the above-mentioned coarse-graining methods guarantee apriori reproducibility of the interfacial free energy, the thermodynamic quantity that characterizes interfaces which are of primary importance for the problem being addressed here. Further, the approach we follow relies on reliable experimental quantities and is computationally simple.

1.5 The Wetting phenomenon

In this section, we shed light on the solid-liquid interactions from a macroscopic view and ways to relate these macroscopic properties to the simulation parameters and the challenges that arise in the process. Wetting is the macroscopic phenomenon that parallels solid-liquid interactions at the atomic scale. A liquid drop in contact with a smooth solid surface, adopts various shapes depending on the interaction strength between the phases.

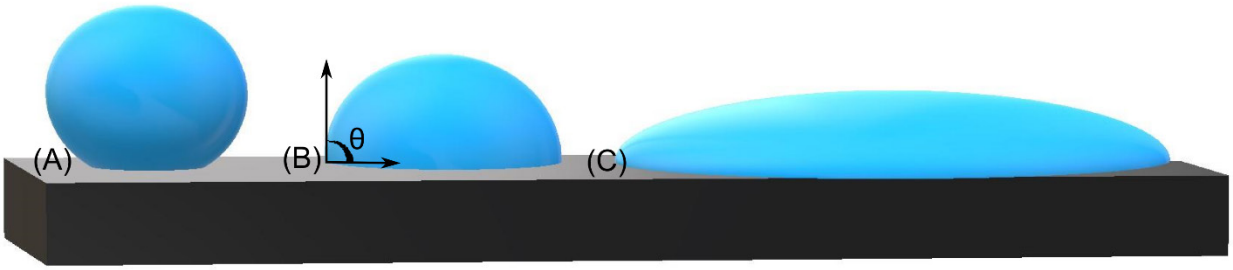

Figure 2. Illustration of liquid droplets in different regimes of wetting from partial wetting (A and B) to fully wetting (C). In the partial wetting regime, the wetting strength, when $\theta < 90°$(A) is often referred to as hydrophobic and $\theta \geq 90°$ (B) as hydrophilic.

As shown in Figure 2, when the solid-liquid interaction is relatively weak (partial wetting), liquid adopts a droplet shape with an angle θ (Figures A, B), otherwise when the solid-liquid phases are highly compatible, and the interaction strengths are strong, the liquid fully wets the surface and forms

a film (fully wetting). In the partial wetting regime, the droplet shape, or the angle θ is determined by the balance of various interfacial tensions acting at the solid-liquid-vapor interface which is given by the Young-Dupré relation:

$$\cos\theta = \frac{\gamma_{SV} - \gamma_{SL}}{\gamma_{LV}}$$

Where, γ is the interfacial tension and S, V and L refer to the solid, vapor and liquid phases respectively. The above equation is a general form of the equation and takes into account that there might be vapor adsorbed on the solid as well. The presence of vapor modifies the solid surface tension, which is termed as spreading pressure (π) and is given by, $\pi=\gamma_S-\gamma_{SV}$, where γ_S is the interfacial tension of the bare solid surface. The spreading pressure could be obtained from the adsorption isotherm and is usually quite small and often neglected. The above equation, neglecting vapor adsorption becomes,

$$\gamma_L \cos\theta = \gamma_S - \gamma_{SL}$$

The above equations are for systems at equilibrium and are applicable only for macroscopic droplets. At the nanoscale, the curvature of the droplet, the three-phase contact line tension may play a role in determining the contact angle. Therefore, a correction is often applied by introducing, line tension τ and the modified equation is,

$$\cos\theta_R = \cos\theta - \frac{\tau}{\gamma_L R}$$

Where θ_R is the contact angle for a given droplet radius R and γ_L is the liquid surface tension.

Droplets in simulations present several difficulties in measurement arising from the size and force-field dependence. Therefore, a quantity often used in relation to wetting is the work of adhesion. It is defined as the free energy required per unit area to separate a solid and a liquid phase that are initially in contact at equilibrium. Following the definition,

$$W_{adh} = \gamma_{LV} + \gamma_{SV} - \gamma_{SL}$$

If we ignore the adsorption of the vapor phase, the work of adhesion becomes the solid-liquid work of adhesion and is given by,

$$W_{SL} = \gamma_L + \gamma_S - \gamma_{SL}$$

Work of adhesion is a free energy unlike the contact angle and has been found to indicate the wettability of a liquid on a given solid surface unambiguously.[125,126] The relationship between W_{SL} and contact angle can be obtained by combining the above equation with the Young-Dupré equation, to give: $W_{SL}=\gamma_{LV}(1+\cos\theta)$.

If one has a knowledge of the wetting at the macroscopic scale characterized by the above quantities, one can parameterize the model parameters to reproduce them (at least for smooth surfaces with no

impurities). Often, the solid-liquid interaction parameters are tuned to reproduce the contact angle or the work of adhesion. The contact angle shows size dependence and the value of line tension is usually not known. Further, when a droplet is simulated, the surface tension of the curved droplet is dependent on the size, which is again non-trivial.[127] Further, usage of work of adhesion has a more profound advantage, as it is a free energy, it is rather fundamental in determining the interaction between a given solid and liquid.[126] Therefore it can be split into its constituent energetic (ΔU_{SL}) and entropic ($T\Delta S_{SL}$) components as:

$$W_{SL} = \frac{\Delta U_{SL}}{A} - \frac{T\Delta S_{SL}}{A}$$

It was recently shown that work of adhesion is directly correlated with the adsorption energy (ΔU_{SL}) which in turn was determined to be a very reliable metric for wettability.[128] Considering all the above facts and issues that arise while simulating droplets, we rely on the work of adhesion as the adopted reference observable in our simulations to obtain the solid-liquid interaction parameters as will be detailed in the following chapters.

1.6 Problems addressed in this thesis

In the current thesis, the problem of characterizing heat transfer through a network of particles is not actually done but the ground framework that is needed for such an analysis has been laid out. Essentially, we focused on simple fluid systems like *n*-hexane as model representations of polymeric systems. Firstly, a deep understanding was obtained about the interfacial thermodynamics of water-graphite and *n*-hexane graphite interfaces. Simultaneously, the influence of coarse-graining on the representation has been studied.

We chose work of adhesion as the characteristic quantity representing solid-liquid interactions and a way to obtain this quantity for coarse-grained potentials is shown in chapter two. The dry surface method which was developed for water was first applied to *n*-hexane, a simple representation of the polymeric systems. Then the dry surface method was extended to coarse-grained potentials obtained using the conditional reversible work method. Although, the method allows us to reproduce work of adhesion, the individual energetic and entropic contributions are modified. Chapter two details the method, how thermodynamics of the interface is changed on coarse-graining and finally concludes by providing general guidelines into coarse-graining of the solid-liquid interactions.

To dig deeper into the thermodynamics of interfaces and the influence that coarse-graining has on these interfaces, we study in detail the water/graphite and water/MoS_2 interfaces as presented in the third chapter. Investigations were carried out on the nature of influence both the liquid coarse-graining

and solid coarse-graining has on the interfacial thermodynamics. In this chapter, we used SPC/E[129] model to represent atomistic water and at the coarse-grained level we used ELBA[129] and mW[130] models. The chapter further includes how the structure differs for each of the models and how these differences have an impact on the overall thermodynamics.

In chapter 5, the insights and knowledge gained in chapters three and four are combined to construct a methodology to simulate graphene sheets adsorbing at the water-oil interface. Simulation of many phases require that a balance is maintained between various interaction strengths. This is achieved by tuning the macroscopic wetting coefficient. Chapter 5, discusses this implementation and illustrates the method at coarse-grained and atomistic resolutions. An example of a simulation where many graphene adsorb at the water-oil interface is illustrated as well.

So far in the thesis, studies have been limited to the equilibrium properties of the interface. The issues caused by coarse-graining to the thermal transport have not yet been discussed. Chapter 6 provides a first step in this direction. A study on interfacial thermal transport across water-graphite interfaces using non-equilibrium molecular dynamics simulations is discussed in detail. The study compares two water models, an atomistic one and a coarse-grained one. Quite surprisingly, both models predict interfacial thermal conductance values very close to each other. A detailed understanding of this observation in addition to the important consequences of this observation are provided.

In the final and 6th chapter, the entire work is summarized, its implications are discussed and a possible roadmap for future studies has been laid out.

References

(1) Moore, G. E. Cramming More Components onto Integrated Circuits. *Electronics* **1965**, 114–117.

(2) Tuomi, I. The Lives and Death of Moore's Law. *First Monday* **2002**, *7* (11).

(3) Knechtel, J.; Sinanoglu, O.; Elfadel, I. M.; Lienig, J.; N Sze, C. C. Large-Scale 3D Chips: Challenges and Solutions for Design Automation, Testing, and Trustworthy Integration. *IPSJ Trans. Syst. LSI Des. Methodol.* **2017**, *10*, 45–62.

(4) Laughlin, S. B.; Sejnowski, T. J.; Choo, X.; Bekolay, T.; DeWolf, T.; Tang, Y.; Rasmussen, D.; Imam, N.; Guo, C.; Nakamura, Y.; et al. Communication in Neuronal Networks. *Science.* **2003**, *301* (5641), 1870–1874.

(5) Caravelli, F.; Traversa, F. L.; Di Ventra, M. The Complex Dynamics of Memristive Circuits: Analytical Results and Universal Slow Relaxation. *Phys. Rev. E,* **2017,** *95,* 0233140.

(6) Alex Pappachen James, Dinesh S. Kumar, and A. A. *IEEE Trans. Very Large Scale Integr.*

Syst. **2015**, *23* (11), 2690–2694.

(7) Waldrop, M. M. The Chips Are down for Moore's Law. *Nature* **2016**, *530* (7589), 144–147.

(8) Balandin, A. Chill Out. *IEEE Spectr.* **2009**, *46* (10), 34–39.

(9) Ball, P. Computer Engineering: Feeling the Heat. *Nature* **2012**, *492* (7428), 174–176.

(10) Razeeb, K. M.; Dalton, E.; Cross, G. L. W.; Robinson, A. J. Present and Future Thermal Interface Materials for Electronic Devices. *Int. Mater. Rev.* **2018**, *63* (1), 1–21.

(11) Bar-Cohen, A.; Matin, K.; Narumanchi, S. Nanothermal Interface Materials: Technology Review and Recent Results. *J. Electron. Packag.* **2015**, *137* (4).

(12) Shahil, K. M. F.; Balandin, A. A. Graphene–Multilayer Graphene Nanocomposites as Highly Efficient Thermal Interface Materials. *Nano Lett.* **2012**, *12* (2), 861–867.

(13) Marconnet, A. M.; Yamamoto, N.; Panzer, M. A.; Wardle, B. L.; Goodson, K. E. Thermal Conduction in Aligned Carbon Nanotube–Polymer Nanocomposites with High Packing Density. *ACS Nano* **2011**, *5* (6), 4818–4825.

(14) Hung Thang, B.; Trinh, P. Van; Chuc, N. Van; Khoi, P. H.; Minh, P. N. Heat Dissipation for Microprocessor Using Multiwalled Carbon Nanotubes Based Liquid. *ScientificWorldJournal.* **2013**, *2013*, 305957.

(15) Balandin, A. a. Thermal Properties of Graphene and Nanostructured Carbon Materials. *Nat. Mater.* **2011**, *10* (8), 569–581.

(16) *Physical Properties of Polymers Handbook*; Mark, J. E., Ed.; Springer New York: New York, NY, 2007.

(17) Buongiorno, J.; Venerus, D. C.; Prabhat, N.; McKrell, T.; Townsend, J.; Christianson, R.; Tolmachev, Y. V.; Keblinski, P.; Hu, L.; Alvarado, J. L.; et al. A Benchmark Study on the Thermal Conductivity of Nanofluids. *J. Appl. Phys.* **2009**, *106* (9), 94312.

(18) Shenogina, N.; Shenogin, S.; Xue, L.; Keblinski, P. On the Lack of Thermal Percolation in Carbon Nanotube Composites. *Appl. Phys. Lett.* **2005**, *87* (13), 133106.

(19) Ge, S.; Chen, M. Vibrational Coupling and Kapitza Resistance at a Solid–Liquid Interface. *Int. J. Thermophysics.* **2012**, *34* (1), 64–77.

(20) Acharya, H.; Mozdzierz, N. J.; Keblinski, P.; Garde, S. How Chemistry, Nanoscale Roughness, and the Direction of Heat Flow Affect Thermal Conductance of Solid–Water Interfaces. *Ind. Eng. Chem. Res.* **2012**, *51* (4), 1767–1773.

(21) Shenogina, N.; Godawat, R.; Keblinski, P.; Garde, S. How Wetting and Adhesion Affect Thermal Conductance of a Range of Hydrophobic to Hydrophilic Aqueous Interfaces. *Phys. Rev. Lett.* **2009**, *102* (15), 156101.

(22) Li, A.; Zhang, C.; Zhang, Y.-F. Thermal Conductivity of Graphene-Polymer Composites:

Mechanisms, Properties, and Applications. *Chem. Mater.,* **2015,** *27*(6), 2100-2106

(23) Nika, D. L.; Balandin, A. A. Phonon Transport in Graphene. *Phonon Transp. Graphene, J. Phys.: Condens. Matt.* **2012**, *24*(23), 233203.

(24) Liu, S.; Xu, X. F.; Xie, R. G.; Zhang, G.; Li, B. W. Anomalous Heat Conduction and Anomalous Diffusion in Low Dimensional Nanoscale Systems. *Eur. Phys. J. B* **2012**, *85* (10), 337.

(25) Shiomi, J.; Maruyama, S. Molecular Dynamics of Diffusive-Ballistic Heat Conduction in Single-Walled Carbon Nanotubes. *Jpn. J. Appl. Phys.* **2008**, *47* (4), 2005–2009.

(26) Wang, J.; Wang, J.-S. Carbon Nanotube Thermal Transport: Ballistic to Diffusive. *Appl. Phys. Lett.* **2006**, *88* (11), 111909.

(27) Tan, Z. W.; Wang, J.-S.; Gan, C. K. First-Principles Study of Heat Transport Properties of Graphene Nanoribbons. *Nano Lett.* **2011**, *11* (1), 214–219.

(28) Pop, E.; Varshney, V.; Roy, A. K. Thermal Properties of Graphene: Fundamentals and Applications. *MRS Bull.* **2012**, *37* (12), 1273–1281.

(29) Balandin, A. A.; Nika, D. L. Thermal Transport in Graphene and Graphene Multilayers. *arXiv:1503.02124,* **2015**.

(30) Amelia Carolina Sparavigna. Politecnico Di Torino Porto Institutional Repository. *Int. J. Sci.* **2014**, *3* (12), 24–27.

(31) Cai, Y.; Lan, J.; Zhang, G.; Zhang, Y.-W. Lattice Vibrational Modes and Phonon Thermal Conductivity of Monolayer MoS2. *Phys. Rev. B* **2014**, *89* (3), 35438.

(32) Matsubara, H.; Kikugawa, G.; Bessho, T.; Yamashita, S.; Ohara, T. Molecular Dynamics Study on the Role of Hydroxyl Groups in Heat Conduction in Liquid Alcohols. *Int. J. Heat Mass Transf.* **2017**, *108*, 749–759.

(33) Kikugawa, G.; Ohara, T.; Kawaguchi, T.; Kinefuchi, I.; Matsumoto, Y. A Molecular Dynamics Study on Heat Transfer Characteristics Over the Interface of Self-Assembled Monolayer and Water Solvent. *J. Heat Transfer* **2014**, *136* (10), 102401.

(34) Ohara, T.; Yuan, T. C.; Torii, D.; Kikugawa, G.; Kosugi, N. Heat Conduction in Chain Polymer Liquids: Molecular Dynamics Study on the Contributions of Inter- and Intramolecular Energy Transfer. *J. Chem. Phys.* **2011**, *135* (3), 34507.

(35) Zhang, L.; Chen, T.; Ban, H.; Liu, L. Hydrogen Bonding-Assisted Thermal Conduction in β-Sheet Crystals of Spider Silk Protein. *Nanoscale* **2014**, *6* (14), 7786–7791.

(36) Bolmatov, D.; Brazhkin, V. V; Trachenko, K. The Phonon Theory of Liquid Thermodynamics. *Sci. Rep.* **2012**, *2* (421), 1–6.

(37) Bolmatov, D.; Zav'yalov, D.; Zhernenkov, M.; Musaev, E. T.; Cai, Y. Q. Unified Phonon-Based Approach to the Thermodynamics of Solid, Liquid and Gas States. *Ann. Phys. (N. Y).* **2015**, *363*,

221–242.

(38) M. Chandrasekar, S. S. A Review on the Mechanisms of Heat Transport in Nanofluids. *Heat Transf. Eng.* **2009**, *30* (14), 1136–1150.

(39) Gupta, A.; Kumar, R. Role of Brownian Motion on the Thermal Conductivity Enhancement of Nanofluids. *Appl. Phys. Lett.* **2007**, *91*, 223102–234701.

(40) Jang, S. P.; Choi, S. U. S. Role of Brownian Motion in the Enhanced Thermal Conductivity of Nanofluids. *Appl. Phys. Lett.* **2004**, *84* (106), 153107–2252.

(41) Azizian, M. R. .; Aybar, H. Ş. .; Okutucu, T. . Effect of Nanoconvection due to Brownian Motion on the Enhancement of Thermal Conductivity of Nanofluids. *Ind. Eng. Chem. Res.* **2009**, *51* (4), 1782–1789.

(42) Zheng, R.; Gao, J.; Wang, J.; Feng, S.-P.; Ohtani, H.; Wang, J.; Chen, G. Thermal Percolation in Stable Graphite Suspensions. *Nano Lett.* **2012**, *12* (1), 188–192.

(43) Sorel, S.; Bellet, D.; Coleman, J. N. Relationship between Material Properties and Transparent Heater Performance for Both Bulk-like and Percolative Nanostructured Networks. *ACS Nano* **2014**, *8* (5), 4805–4814.

(44) Zhu, H.; Li, Y.; Fang, Z.; Xu, J.; Cao, F.; Wan, J.; Preston, C. Highly Thermally Conductive Papers With Percolative Layered Boron Nitride Nanosheets. *ACS Nano.* **2014**, *8*(4), 3606–3613.

(45) Kwon, S. Y.; Kwon, I. M.; Kim, Y.-G.; Lee, S.; Seo, Y.-S. A Large Increase in the Thermal Conductivity of Carbon Nanotube/polymer Composites Produced by Percolation Phenomena. *Carbon N. Y.* **2013**, *55*, 285–290.

(46) Wang, J. J.; Zheng, R. T.; Gao, J. W.; Chen, G. Heat Conduction Mechanisms in Nanofluids and Suspensions. *Nano Today* **2012**, *7* (2), 124–136.

(47) Huang, J.; Zhu, Y.; Xu, L.; Chen, J.; Jiang, W.; Nie, X. Massive Enhancement in the Thermal Conductivity of Polymer Composites by Trapping Graphene at the Interface of a Polymer Blend. *Compos. Sci. Technol.* **2016**, *129*, 160–165.

(48) Song, W.-L.; Veca, L. M.; Kong, C. Y.; Ghose, S.; Connell, J. W.; Wang, P.; Cao, L.; Lin, Y.; Meziani, M. J.; Qian, H.; et al. Polymeric Nanocomposites with Graphene Sheets – Materials and Device for Superior Thermal Transport Properties. *Polymer.* **2012**, *53* (18), 3910–3916.

(49) Wang, P.; Chong, H.; Zhang, J.; Lu, H. Constructing 3D Graphene Networks in Polymer Composites for Significantly Improved Electrical and Mechanical Properties. *ACS Appl. Mater. Interfaces* **2017**, *9* (26), 22006–22017.

(50) Lv, W.; Xia, Z.; Wu, S.; Tao, Y.; Jin, F.-M.; Li, B.; Du, H.; Zhu, Z.-P.; Yang, Q.-H.; Kang, F. Conductive Graphene-Based Macroscopic Membrane Self-Assembled at a Liquid-Air

Interface. *J. Mater. Chem.* **2011**, *21* (10), 3359–3364.

(51) Xiang, J.; Drzal, L. T. Thermal Conductivity of a Monolayer of Exfoliated Graphite Nanoplatelets Prepared by Liquid-Liquid Interfacial Self-Assembly. *J. Nanomater.* **2010,** *2010*, 481753.

(52) Bento, J. L.; Brown, E.; Woltornist, S. J.; Adamson, D. H. Thermal and Electrical Properties of Nanocomposites Based on Self-Assembled Pristine Graphene. *Adv. Funct. Mater.* **2017**, *27* (1), 1604277.

(53) Woltornist, S. J.; Varghese, D.; Massucci, D.; Cao, Z.; Dobrynin, A. V.; Adamson, D. H. Controlled 3D Assembly of Graphene Sheets to Build Conductive, Chemically Selective and Shape-Responsive Materials. *Adv. Mater.* **2017**, *29* (18), 1604947.

(54) Woltornist, S. J.; Carrillo, J. M. Y.; Xu, T. O.; Dobrynin, A. V; Adamson, D. H. Polymer/pristine Graphene Based Composites: From Emulsions to Strong, Electrically Conducting Foams. *Macromolecules* **2015**, *48* (3), 687–693.

(55) Zhang, Y.; Shen, Y.; Kuehner, D.; Wu, S.; Su, Z.; Ye, S.; Niu, L. Directing Single-Walled Carbon Nanotubes to Self-Assemble at Water/oil Interfaces and Facilitate Electron Transfer. *Chem. Commun.* **2008**, 0 , 4273.

(56) Arapov, K.; Goryachev, A.; de With, G.; Friedrich, H. A Simple and Flexible Route to Large-Area Conductive Transparent Graphene Thin-Films. *Synth. Met.* **2015**, *201*, 67.

(57) Wang, Y.; Shan, J. W.; Weng, G. J. Percolation Threshold and Electrical Conductivity of Graphene-Based Nanocomposites with Filler Agglomeration and Interfacial Tunneling. *J. Appl. Phys.* **2015**, *118* (6).

(58) Landauer, R. Spatial Variation of Currents and Fields Due to Localized Scatterers in Metallic Conduction. *IBM J. Res. Dev.* **1957**, *1* (3), 223–231.

(59) Zhou, Y.; Strachan, A. Thermal Conduction in Molecular Materials Using Coarse Grain Dynamics: Role of Mass Diffusion and Quantum Corrections for Molecular Dynamics Simulations. *J. Chem. Phys.* **2009**, *131* (23), 234113.

(60) Clancy, T. C.; Gates, T. S. Modeling of Interfacial Modification Effects on Thermal Conductivity of Carbon Nanotube Composites. *Polymer*, **2006**, *47* (16), 5990–5996.

(61) Konatham, D.; Striolo, A. Thermal Boundary Resistance at the Graphene-Oil Interface. *J. Chem. Phys.* **2009**, *95* (16), 163105.

(62) Wang, M.; Galpaya, D.; Lai, Z. B.; Xu, Y.; Yan, C. Surface Functionalization on the Thermal Conductivity of Graphene–polymer Nanocomposites. *Int. J. Smart Nano Mater.* **2014**, *5* (2), 123–132.

(63) Wang, Y.; Liu, J.; Zhou, J.; Yang, R. Thermoelectric Transport Across Nanoscale Polymer–

Semiconductor–Polymer Junctions. *J. Phys. Chem. C* **2013**, *117* (47), 24716–24725.

(64) Gardea, F.; Naraghi, M.; Lagoudas, D. Effect of Thermal Interface on Heat Flow in Carbon Nano Fi Ber Composites. *ACS Appl. Mater. Interfaces.* **2014**, *6(*2), 1061-1072.

(65) Chen, I.-J.; Mante, P.-A.; Chang, C.-K.; Yang, S.-C.; Chen, H.-Y.; Huang, Y.-R.; Chen, L.-C.; Chen, K.-H.; Gusev, V.; Sun, C.-K. Graphene-to-Substrate Energy Transfer through out-of-Plane Longitudinal Acoustic Phonons. *Nano Lett.* **2014**, *14* (3), 1317–1323.

(66) Warzoha, R. J.; Fleischer, A. S. Heat Flow at Nanoparticle Interfaces. *Nano Energy* **2014**, *6*, 137–158.

(67) Pernot, G.; Stoffel, M.; Savic, I.; Pezzoli, F.; Chen, P.; Savelli, G.; Jacquot, a; Schumann, J.; Denker, U.; Mönch, I.; et al. Precise Control of Thermal Conductivity at the Nanoscale through Individual Phonon-Scattering Barriers. *Nat. Mater.* **2010**, *9* (6), 491–495.

(68) Roy, A. K.; Farmer, B. L.; Varshney, V.; Sihn, S.; Lee, J.; Ganguli, S. Importance of Interfaces in Governing Thermal Transport in Composite Materials: Modeling and Experimental Perspectives. *ACS Appl. Mater. Interfaces* **2012**, *4* (2), 545–563.

(69) Luo, T.; Lloyd, J. R. Enhancement of Thermal Energy Transport Across Graphene/Graphite and Polymer Interfaces: A Molecular Dynamics Study. *Adv. Funct. Mater.* **2012**, *22* (12), 2495–2502.

(70) Hu, M.; Keblinski, P.; Schelling, P. Kapitza Conductance of Silicon–amorphous Polyethylene Interfaces by Molecular Dynamics Simulations. *Phys. Rev. B* **2009**, *79* (10), 104305.

(71) Rajeshwari, P.; Dey, T. K. Finite Element Modelling and Experimental Investigation on Effective Thermal Conductivity of AlN (Nano) Particles Reinforced HDPE Polymer Nanocomposites. *Thermochim. Acta* **2016**, *638*, 103–112.

(72) Mortazavi, B.; Rabczuk, T. Multiscale Modeling of Heat Conduction in Graphene Laminates, *Carbon,* **2015,** *85,* 1-7.

(73) Konatham, D.; Bui, K. N. D.; Papavassiliou, D. V.; Striolo, A. Simulation Insights into Thermally Conductive Graphene-Based Nanocomposites. *Mol. Phys.* **2011**, *109* (1), 97–111.

(74) Liu, J.; Chen, S.; Nie, X.; Robbins, M. O. A Continuum–atomistic Simulation of Heat Transfer in Micro-and Nano-Flows. *J. Comp. Phys,* **2007,** *227(*1),279-291.

(75) Gao, Y.; Müller-Plathe, F. Increasing the Thermal Conductivity of Graphene-Polyamide-6,6 Nanocomposites by Surface-Grafted Polymer Chains: Calculation with Molecular Dynamics and Effective-Medium Approximation, *J. Phys. Chem. B*. **2016,** *120*(7), 1336-1346.

(76) Gao, Y.; Müller-Plathe, F. Effect of Grafted Chains on the Heat Transfer between Carbon Nanotubes in a Polyamide-6.6 Matrix: A Molecular Dynamics Study. *Polym. (United Kingdom)* **2017**, *129*, 228–234.

(77) Gao, Y.; Müller-Plathe, F. Molecular Dynamics Study on the Thermal Conductivity of the End-Grafted Carbon Nanotubes Filled Polyamide-6.6 Nanocomposites. *J. Phys. Chem. C* **2018**, *122* (2), 1412–1421.

(78) Liu, J.; Gao, Y.; Cao, D.; Zhang, L.; Guo, Z. Nanoparticle Dispersion and Aggregation in Polymer Nanocomposites: Insights from Molecular Dynamics Simulation. *Langmuir* **2011**, *27* (12), 7926–7933.

(79) Feng, Y.; Zou, H.; Tian, M.; Zhang, L.; Mi, J. Relationship between Dispersion and Conductivity of Polymer Nanocomposites: A Molecular Dynamics Study*, J. Phys. Chem. B,* **2012**, *116(43),*13081-13088 .

(80) Meng, D.; Kumar, S. K.; Cheng, S.; Grest, G. S. Simulating the Miscibility of Nanoparticles and Polymer Melts. *Soft Matter* **2013**, *9* (22), 5417–5427.

(81) Park, J.; Kalra, V.; Joo, Y. Controlling the Dispersion and Orientation of Nanorods in Polymer Melt under Shear: Coarse-Grained Molecular Dynamics Simulation Study. *J. Chem. Phys.* **2014**, *140* (12), 124903.

(82) Patra, T. K.; Singh, J. K. Polymer Directed Aggregation and Dispersion of Anisotropic Nanoparticles. *Soft Matter.* **2013**, *10* (11), 1823–1830.

(83) Xie, B.; Buehler, M. J.; Xu, Z. Directed Self-Assembly of End-Functionalized Nanofibers: From Percolated Networks to Liquid Crystal-like Phases. *Nanotechnology* **2015**, *26* (20), 205602.

(84) Sinsawat, A.; Anderson, K. L.; Vaia, R. A.; Farmer, B. L. Influence of Polymer Matrix Composition and Architecture on Polymer Nanocomposite Formation: Coarse-grained Molecular Dynamics Simulation. **2003**, *41* (24), 3272–3284.

(85) Frost, D. S.; Dai, L. L. Molecular Dynamics Simulations of Charged Nanoparticle Self-Assembly at Ionic Liquid-Water and Ionic Liquid-Oil Interfaces. *J. Chem. Phys.* **2012**, *136*, 084706/1.

(86) Yang, P.; Liu, F. Understanding Graphene Production by Ionic Surfactant Exfoliation: A Molecular Dynamics Simulation Study. *J. Appl. Phys.* **2014**, *116* (1), 014304.

(87) Suter, J. L.; Groen, D.; Coveney, P. V. Mechanism of Exfoliation and Prediction of Materials Properties of Clay–Polymer Nanocomposites from Multiscale Modeling. *Nano Lett.* **2015**, *15* (12), 8108–8113.

(88) Shih, C.-J.; Lin, S.; Strano, M. S.; Blankschtein, D. Understanding the Stabilization of Liquid-Phase-Exfoliated Graphene in Polar Solvents: Molecular Dynamics Simulations and Kinetic Theory of Colloid Aggregation. *J. Am. Chem. Soc.* **2010**, *132* (41), 14638–14648.

(89) Shih, C.-J.; Lin, S.; Sharma, R.; Strano, M. S.; Blankschtein, D. Understanding the {pH-Dependent} Behavior of Graphene Oxide Aqueous Solutions: A Comparative Experimental and

Molecular Dynamics Simulation Study. *Langmuir* **2012**, *28* (1), 235–241.

(90) Pupysheva, O. V; Farajian, A. A.; Knick, C. R.; Zhamu, A.; Jang, B. Z. Modeling Direct Exfoliation of Nanoscale Graphene Platelets. **2010**, *114* (49), 21083–21087.

(91) Oyer, A. J.; Carrillo, J.-M. Y.; Hire, C. C.; Schniepp, H. C.; Asandei, A. D.; Dobrynin, A. V; Adamson, D. H. Stabilization of Graphene Sheets by a Structured Benzene/Hexafluorobenzene Mixed Solvent. **2012**, *134* (11), 5018–5021.

(92) Zhao, Y.; Byshkin, M.; Cong, Y.; Kawakatsu, T.; Guadagno, L.; De Nicola, A.; Yu, N.; Milano, G.; Dong, B. Nanoscale Self-Assembly of Carbon Nanotubes in Polymer Melts: Simulation of Structural and Electrical Behaviour by Hybrid Particle-Field Molecular Dynamics. *Nanoscale* **2016**, *8* (34), 15361–15824.

(93) Karatasos, K. Graphene/Hyperbranched Polymer Nanocomposites: Insight from Molecular Dynamics Simulations. *Macromolecules* **2014**, *47* (24), 8833–8845.

(94) Ju, S.-P.; Wang, Y.-C.; Huang, G.-J.; Chang, J.-W. Miscibility of Graphene and Poly(methyl Methacrylate) (PMMA):Molecular Dynamics and Dissipative Particle Dynamics Simulations. *RSC Adv.* **2013**, *3* (22), 8298.

(95) Skountzos, E. N.; Anastassiou, A.; Mavrantzas, V. G.; Theodorou, D. N. Determination of the Mechanical Properties of a Poly(methyl Methacrylate) Nanocomposite with Functionalized Graphene Sheets through Detailed Atomistic Simulations. *Macromolecules.* **2014**, *47* (22), 8072–8088.

(96) Rissanou, A. N.; Power, A.; Harmandaris, V. Structural and Dynamical Properties of Polyethylene/Graphene Nanocomposites through Molecular Dynamics Simulations. *Polymers,* **2015**, *7* (3), 390-417.

(97) Zhang, J.; Jiang, D. Molecular Dynamics Simulation of Mechanical Performance of Graphene/graphene Oxide Paper Based Polymer Composites. *Carbon,* **2014**, *67*, 784–791.

(98) Pollack, G. L. Kapitza Resistance. *Rev. Mod. Phys.* **1969**, *41* (1), 48–81.

(99) Sun, F.; Zhang, T.; Jobbins, M. M.; Guo, Z.; Zhang, X.; Zheng, Z.; Tang, D.; Ptasinska, S.; Luo, T. Molecular Bridge Enables Anomalous Enhancement in Thermal Transport across Hard-Soft Material Interfaces. *Adv. Mater.* **2014**, 6093–6099.

(100) Losego, M. D.; Grady, M. E.; Sottos, N. R.; Cahill, D. G.; Braun, P. V. Effects of Chemical Bonding on Heat Transport across Interfaces. *Nat. Mater.* **2012**, *11* (6), 502–506.

(101) Harikrishna, H.; Ducker, W. A.; Huxtable, S. T. The Influence of Interface Bonding on Thermal Transport through Solid–liquid Interfaces. *Appl. Phys. Lett.* **2013**, *102* (25), 251606.

(102) Ramos-Alvarado, B.; Kumar, S.; Peterson, G. P. Solid−Liquid Thermal Transport and Its Relationship with Wettability and the Interfacial Liquid Structure. *J. Phys. Chem. Lett.* **2016**, *7*

(17), 3497–3501.

(103) Merabia, S.; Lombard, J.; Alkurdi, A. Importance of Viscoelastic and Interface Bonding Effects in the Thermal Boundary Conductance of Solid–water Interfaces. *Int. J. Heat Mass Transf.* **2016**, *100*, 287–294.

(104) Nan, C.-W.; Birringer, R.; Clarke, D. R.; Gleiter, H. Effective Thermal Conductivity of Particulate Composites with Interfacial Thermal Resistance. *J. Appl. Phys.* **1997**, *81* (10), 6692.

(105) Neogi, S.; Reparaz, J. S.; Pereira, L. F. C.; Graczykowski, B.; Wagner, M. R.; Sledzinska, M.; Shchepetov, A.; Prunnila, M.; Ahopelto, J.; Sotomayor-Torres, C. M.; et al. Tuning Thermal Transport in Ultrathin Silicon Membranes by Surface Nanoscale Engineering. *ACS Nano* **2015**, *9* (4), 3820–3828.

(106) Han, H.; Merabia, S.; Müller-Plathe, F. Thermal Transport at a Solid–nanofluid Interface: From Increase of Thermal Resistance towards a Shift of Rapid Boiling. *Nanoscale* **2017**, *9* (24), 8314–8320.

(107) Han, H.; Mérabia, S.; Müller-Plathe, F. Thermal Transport at Solid-Liquid Interfaces: High Pressure Facilitates Heat Flow through Nonlocal Liquid Structuring. *J. Phys. Chem. Lett.* **2017**, *8* (9), 1946–1951.

(108) Han, H.; Schlawitschek, C.; Katyal, N.; Stephan, P.; Gambaryan-Roisman, T.; Leroy, F.; Müller-Plathe, F. Solid-Liquid Interface Thermal Resistance Affects the Evaporation Rate of Droplets from a Surface: A Study of Perfluorohexane on Chromium Using Molecular Dynamics and Continuum Theory. *Langmuir* **2017**, *33* (21), 5336–5343.

(109) Alaghemandi, Mohammad; Müller-Plathe, Florian; C. Böhm, M. Thermal Conductivity of Carbon Nanotube- Polyamide-6,6 Nanocomposites: Reverse Non-Equilibrium Molecular Dynamics Simulations. *J. Chem. Phys.* **2011**, *135*, 184905.

(110) Ingólfsson, H. I.; Lopez, C. A.; Uusitalo, J. J.; de Jong, D. H.; Gopal, S. M.; Periole, X.; Marrink, S. J. The Power of Coarse Graining in Biomolecular Simulations. *Wiley Interdiscip. Rev. Comput. Mol. Sci.* **2014**, *4* (3), 225–248.

(111) Riniker, S.; Allison, J. R.; van Gunsteren, W. F. On Developing Coarse-Grained Models for Biomolecular Simulation: A Review. *Phys. Chem. Chem. Phys.* **2012**, *14* (36), 12423.

(112) Barnoud, J.; Monticelli, L. Coarse-Grained Force Fields for Molecular Simulations. In *Methods in molecular biology (Clifton, N.J.)*; 2015; Vol. 1215, pp 125–149.

(113) Merchant, B. A.; Madura, J. D. A Review of Coarse-Grained Molecular Dynamics Techniques to Access Extended Spatial and Temporal Scales in Biomolecular Simulations. *Annu. Rep. Comput. Chem.* **2011**, *7*, 67–87.

(114) Kmiecik, S.; Gront, D.; Kolinski, M.; Wieteska, L.; Dawid, A. E.; Kolinski, A. Coarse-Grained

Protein Models and Their Applications. *Chem. Rev.* **2016**, *116* (14), 7898–7936.

(115) Saunders, M. G.; Voth, G. A. Coarse-Graining Methods for Computational Biology. *Annu. Rev. Biophys.* **2013**, *42* (1), 73–93.

(116) Reith, D.; Pütz, M.; Müller-Plathe, F. Deriving Effective Mesoscale Potentials from Atomistic Simulations. *J. Comput. Chem.* **2003**, *24* (13), 1624–1636.

(117) Lyubartsev, A. P. Multiscale Modeling of Lipids and Lipid Bilayers. *Eur. Biophys. J.* **2005**, *35* (1), 53–61.

(118) Izvekov, S.; Voth, G. A. A Multiscale Coarse-Graining Method for Biomolecular Systems. *J. Phys. Chem. B,* **2005**, *109*(7), 2469-2473.

(119) Scott, M.S. The Relative Entropy Is Fundamental to Multiscale and Inverse Thermodynamic Problems. *J. Chem. Phys.* **2008,** *129*(14), 144108.

(120) Brini, E.; Marcon, V.; van der Vegt, N. F. A. Conditional Reversible Work Method for Molecular Coarse Graining Applications. *Phys. Chem. Chem. Phys.* **2011**, *13* (22), 10468.

(121) Siewert J. Marrink; H. Jelger Risselada; Serge Yefimov; D. Peter Tieleman, and; Vries, A. H. de. The MARTINI Force Field: Coarse Grained Model for Biomolecular Simulations. *J. Phys. Chem. B* **2007**, *111*(27)*, 7812-7824*.

(122) Praprotnik, M.; Site, L. D.; Kremer, K. Adaptive Resolution Molecular Dynamics Simulation: Changing the Degrees of Freedom on the Fly, *J. Chem. Phys*. **2005**, 123, 224106.

(123) Potestio, R.; Fritsch, S.; Español, P.; Delgado-Buscalioni, R.; Kremer, K.; Everaers, R.; Donadio, D. Hamiltonian Adaptive Resolution Simulation for Molecular Liquids. *Phys. Rev. Lett.* **2013**, *110* (10), 108301.

(124) Suter, J. L.; Groen, D.; Coveney, P. V. Clay-Polymer Nanocomposites: Chemically Specific Multiscale Modeling of Clay-Polymer Nanocomposites Reveals Intercalation Dynamics, Tactoid Self-Assembly and Emergent Materials Properties. *Adv. Mater.* **2015**, *27* (6), 957–957.

(125) Kumar, V.; Errington, J. R. Wetting Behavior of Water near Nonpolar Surfaces. *J. Phys. Chem. C* **2013**, *117* (44), 23017–23026.

(126) Leroy, F.; Liu, S.; Zhang, J. Parametrizing Nonbonded Interactions from Wetting Experiments via the Work of Adhesion: Example of Water on Graphene Surfaces. *J. Phys. Chem. C* **2015**, *119* (51), 28470–28481.

(127) Kanduč, M. Going beyond the Standard Line Tension: Size-Dependent Contact Angles of Water Nanodroplets. *J. Chem. Phys.* **2017**, *147* (17), 174701.

(128) Giro, R.; Bryant, P. W.; Engel, M.; Neumann, R. F.; Steiner, M. B. Adsorption Energy as a Metric for Wettability at the Nanoscale. *Sci. Rep.* **2017**, *7*, 46317.

(129) Jorgensen, W. L.; Maxwell, D. S.; Tirado-Rives, J. Development and Testing of the OPLS All-

Atom Force Field on Conformational Energetics and Properties of Organic Liquids. *J. Am. Chem. Soc.* **1996**, *118* (45), 11225–11236.

(130) Molinero, V.; Moore, E. B. Water Modeled As an Intermediate Element between Carbon and Silicon. *J. Phys. Chem. B* **2009**, *113* (13), 4008–4016.

(131) Woltornist, S. J.; Oyer, A. J.; Carrillo, J. M. Y.; Dobrynin, A. V.; Adamson, D. H. Conductive Thin Films of Pristine Graphene by Solvent Interface Trapping. *ACS Nano* **2013**, *7* (8), 7062–7066.

(132) Biswas, S.; Drzal, L. T. A Novel Approach to Create a Highly Ordered Monolayer Film of Graphene Nanosheets at the Liquid-Liquid Interface. *Nano Lett.* **2009**, *9* (1), 167–172.

(133) Wan, W.; Zhao, Z.; Hughes, T. C.; Qian, B.; Peng, S.; Hao, X.; Qiu, J. Graphene Oxide Liquid Crystal Pickering Emulsions and Their Assemblies. *Carbon N. Y.* **2015**, *85*, 16–23.

(134) Kuilla, T.; Bhadra, S.; Yao, D.; Kim, N. H.; Bose, S.; Lee, J. H. Recent Advances in Graphene Based Polymer Composites. *Prog. Polym. Sci.* **2010**, *35*, 1350–1375.

(135) Depa, P.; Chen, C.; Maranas, J. K. Why Are Coarse-Grained Force Fields Too Fast A Look at Dynamics of Four Coarse-Grained Polymers. *J. Chem. Phys.* **2011**, *134* (1), 14903.

(136) Carbone, P.; Varzaneh, H. A. K.; Chen, X.; Müller-Plathe, F. Transferability of Coarse-Grained Force Fields: The Polymer Case. *J. Chem. Phys.* **2008**, *128* (6), 64904.

(137) Depa, P. K.; Maranas, J. K. Speed up of Dynamic Observables in Coarse-Grained Molecular-Dynamics Simulations of Unentangled Polymers. *J. Chem. Phys.* **2005**, *123* (9), 94901.

(138) Fischer, J.; Paschek, D.; Geiger, A.; Sadowski, G. Modeling of Aqueous Poly(oxyethylene) Solutions. 2. Mesoscale Simulations. *J. Phys. Chem. B* **2008**, *112* (43), 13561–13571.

(139) Nielsen, S. O.; Lopez, C. F.; Srinivas, G.; Klein, M. L. Coarse Grain Models and the Computer Simulation of Soft Materials. *J. Phys. Condens. Matter* **2004**, *16* (4), 481–512.

(140) Hong, B.; Chremos, A.; Panagiotopoulos, A. Z. Dynamics in Coarse-Grained Models for Oligomer-Grafted Silica Nanoparticles. *J. Chem. Phys.* **2012**, *136* (20).

(141) Leroy, F. Revisiting the Droplet Simulation Approach to Derive Force-Field Parameters for Water on Molybdenum Disulfide from Wetting Angle Measurements. *J. Chem. Phys.* **2016**, *145* (16), 164705.

(142) Riniker, S.; Allison, J. R.; van Gunsteren, W. F. On Developing Coarse-Grained Models for Biomolecular Simulation: A Review. *Phys. Chem. Chem. Phys.* **2012**, *14* (36), 12423.

(143) Müller-Plathe, F. Coarse-Graining in Polymer Simulation: From the Atomistic to the Mesoscopic Scale and Back. *ChemPhysChem* **2002**, *3* (9), 754–769.

(144) Louis, A. A. Beware of Density Dependent Pair Potentials. *J. Physics-Condensed Matter* **2002**, *14* (40), 9187–9206.

(145) Brini, E.; Algaer, E. A.; Ganguly, P.; Li, C.; Rodríguez-Ropero, F.; Vegt, N. F. a. Van Der. Systematic Coarse-Graining Methods for Soft Matter Simulations – a Review. *Soft Matter* **2013**, *9* (7), 2108–2119.

(146) Driskill, J.; Vanzo, D.; Bratko, D.; Luzar, A. Wetting Transparency of Graphene in Water. *J. Chem. Phys.* **2014**, *141* (18), 18C517.

(147) Fowkes, F. M. Attractive Forces at Interfaces. *Ind. Eng. Chem.* **1964**, *56* (12), 40–52.

CHAPTER # 2

THE JOURNAL OF CHEMICAL PHYSICS **143**, 243135 (2015)

Solid-liquid work of adhesion of coarse-grained models of n-hexane on graphene layers derived from the conditional reversible work method

Vikram Reddy Ardham,[1,a)] Gregor Deichmann,[2,a)] Nico F. A. van der Vegt,[2,b)] and Frédéric Leroy[1,b)]

[1]*Eduard-Zintl-Institut für Anorganische und Physikalische Chemie, Technische Universität Darmstadt, Alarich-Weiss-Strasse 4, 64287 Darmstadt, Germany*

[2]*Center of Smart Interfaces, Technische Universität Darmstadt, Alarich-Weiss-Strasse 10, 64287 Darmstadt, Germany*

(Received 4 September 2015; accepted 9 November 2015; published online 24 November 2015)

We address the question of how reducing the number of degrees of freedom modifies the interfacial thermodynamic properties of heterogeneous solid-liquid systems. We consider the example of *n*-hexane interacting with multi-layer graphene which we model both with fully atomistic and coarse-grained (CG) models. The CG models are obtained by means of the conditional reversible work (CRW) method. The interfacial thermodynamics of these models is characterized by the solid-liquid work of adhesion W_{SL} calculated by means of the dry-surface methodology through molecular dynamics simulations. We find that the CRW potentials lead to values of W_{SL} that are larger than the atomistic ones. Clear understanding of the relationship between the structure of *n*-hexane in the vicinity of the surface and W_{SL} is elucidated through a detailed study of the energy and entropy components of W_{SL}. We highlight the crucial role played by the solid-liquid energy fluctuations. Our approach suggests that CG potentials should be designed in such a way that they preserve the range of solid-liquid interaction energies, but also their fluctuations in order to preserve the reference atomistic value of W_{SL}. Our study thus opens perspectives into deriving CG interaction potentials that preserve the thermodynamics of solid-liquid contacts and will find application in studies that intend to address materials driven by interfaces. © *2015 AIP Publishing LLC.* [http://dx.doi.org/10.1063/1.4936253]

I. INTRODUCTION

Materials of technological interest such as colloids, colloidal particles at the interface between immiscible fluids, nanocomposites, nano- and microfluidic systems, polymer thin, or thick films on surfaces to name a few are characterized by large surface to volume ratio. Therefore, their overall stability and phase behavior are dominated by their interfacial thermodynamic properties. This behavior in turn influences many other properties of practical interest. For example, nanocomposites show remarkable thermal, electric, and mechanical properties.[1–4] Moreover, nanocomposites allow a great degree of tuning to obtain desirable properties. The behavior of interfacial materials is intimately related to the intermolecular interactions in the vicinity of the interfaces. This feature calls for the use of methods such as the molecular simulation approach to understand better these interactions. However, the length and time scales which characterize such soft matter systems are hardly accessible to quantum mechanical methods and simulations with atomistic force-fields. One possible approach is found in coarse-graining (CG) according to which the resolution of all atom systems is lowered (coarsened) by mapping several atoms into an effective interaction site and, therefore, greatly reducing the number of degrees of freedom. Of course, this comes at a cost and one might potentially lose some information with coarse-graining, so it is quintessential that one obtains the CG potentials by removing only the degrees of freedom that are not relevant to the property under study. The bead-spring model of Grest and Kremer,[5] which has recently been employed to study the structure and dynamics of polymer melts at surfaces,[6] has proven to be particularly useful in computational studies of generic polymer behavior. However, the trend that has emerged in the last two decades is to develop CG models that go beyond generic behavior and which are able to retain a close link to the chemistry of the system at hand.[7–14] Although, there are a vast number of methodologies to obtain CG potentials for liquid-liquid systems in the bulk and solid-liquid systems of the same species, the same is not true for heterogeneous solid-liquid systems. A few of the existing techniques are briefly summarized below.

In Refs. 15 and 16, methodologies have been described to obtain solid-liquid interaction potentials between CG liquid particles and surfaces. However, the solid in both the cases has been replaced by a smooth surface acting like an external field with which liquid interacts depending on the distance of the liquid particles from the surface. Müller *et al.*[17] examined polymers in contact with a solid surface using bead-spring polymer models with different number of beads but identical end-to-end distance and discussed the effect of polymer coarse-graining on the interfacial tension. CG interaction potentials between the solid surface and polymer have also been obtained by mapping the polymer into different

[a)]V. R. Ardham and G. Deichmann contributed equally to this work.

[b)]Author to whom correspondence should be addressed. Electronic addresses: vandervegt@csi.tu-darmstadt.de and f.leroy@theo.chemie.tu-darmstadt.de

beads and then using density functional theory to calculate the adsorption energies of the beads which are then used to parameterize the interaction potentials.[18–20]

Coarse-grained studies often focus on and succeed in reproducing the interfacial structure of polymers near surfaces.[21–23] However, little is known on the relationship between structure and interfacial thermodynamics. Especially it is unknown whether the fact that interfacial polymer or liquid structure is preserved upon coarse-graining induces that the interfacial thermodynamic properties are also comparable in the atomistic and coarse-grained representations. Because coarse-graining strongly modifies the potential energy surface of a given system,[24] one may ask to what extent coarse-graining degrades the thermodynamic properties of an interfacial system. Our approach is to calculate the solid-liquid work of adhesion of *n*-hexane on graphene layers. Work of adhesion is defined as the reversible work per unit area required to separate solid-liquid surfaces. Herein, we report CG models of this system by means of the conditional reversible work (CRW) method[25] and calculate the work of adhesion of both the atomistic and CG models with the recently developed dry-surface approach.[26] We quantify how coarsening modifies the solid-liquid work of adhesion both in its energy and entropy components. We develop clear understanding of the relationship between structure and thermodynamics and highlight the crucial effect of energy fluctuations. Our approach does not only serve as a diagnostic tool to quantify the interfacial thermodynamics of atomistic and CG solid-liquid systems. It also provides with an approach to derive CG potentials that are able to reproduce the corresponding reference thermodynamic properties and paves the way to address systems whose wetting behavior is of crucial importance.

The manuscript is organized as follows. The computational details of our study are given in Section II. The models and especially the conditional reversible work method are discussed in Section III. We discuss in Section IV the theoretical background of the solid-liquid work of adhesion and the technicalities of the dry-surface method. We present results in Section V, before we conclude our work in Section VI.

II. COMPUTATIONAL DETAILS

Both atomistic and coarse-grained simulations were performed using different setups. Liquid bulk and liquid-vapor equilibrium simulations were conducted. The work of adhesion calculations were performed with a liquid film in contact with a solid surface as shown in Fig. 1. The system had then two interfaces, i.e., a solid-liquid and liquid-vapor interface. All the calculations were performed in a simulation cell having a rectangular shape whose dimension in the xy plane was $\mathcal{A} = 4.428 \times 4.261$ nm^2. In the calculations on systems with interfaces, $\mathcal{A}$ denotes their cross-sectional area. The systems contained 1000 *n*-hexane molecules such that the thickness of the liquid phase was approximately 11-12 nm. The dimension of the simulation cell for the liquid-vapor equilibrium system was fixed to 30 nm. This dimension was set to 45 nm for the work of adhesion calculations. This length was chosen to minimize the electrostatic interaction between the periodic images in the direction perpendicular to the surface in the atomistic simulations. In the development of the CG potentials and in the work of adhesion calculations, the solid surface was made up of a stack of four graphene monolayers. The AA-type stacking was adopted, i.e., all the carbon atoms in adjacent layers were immediately above each other. Note that we intend to perform a comparison between the all-atom and CG models rather than a comparison to possible experiments. Although graphene layers may be found with the AA-type stacking,[27,28] the AB-stacking is a more common form. The interlayer spacing was set to 0.335 nm and the carbon-carbon bond distance to 0.142 nm. The distance between the surface particles in one of the coarse-grained representation will be discussed in Section III. The surface particles were frozen and remained at their crystallographic position for the entire simulations. We focus on the study of the solid-liquid interactions without the influence of the internal dynamics of the graphene layers. Although the corresponding degrees of freedom may be included in the atomistic resolution through existing models like the Tersoff potential,[29] they would have to be developed in the CG resolution if the flexibility of the surface has to be included. To prevent that too many molecules evaporate from the liquid film during the work of adhesion calculations, an additional graphene layer with repulsive interaction with *n*-hexane was placed at 15 nm above the bottom graphene layer of the solid (Fig. 1). When a molecule evaporated from the film, it collided with this wall and was sent back toward the liquid film. The bulk, liquid-vapor, and work of adhesion calculations were conducted with LAMMPS.[30] The bulk simulations were performed with a Nosé-Hoover type barostat as implemented in LAMMPS at 300 K and

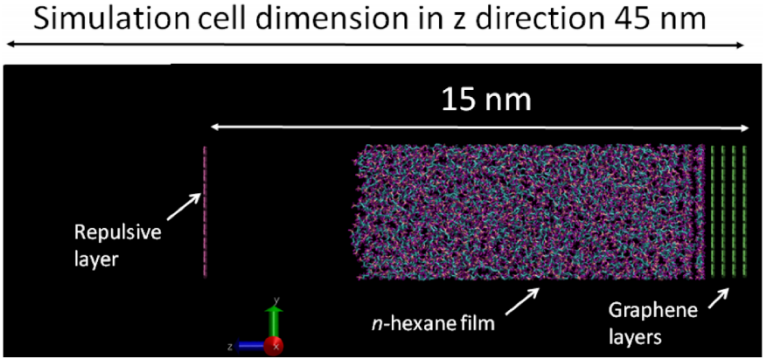

FIG. 1. Typical snapshot of the simulation cell with the liquid film arrangement.

1 atm, with coupling constants of 200 and 2000 time steps for temperature and pressure, respectively. The liquid-vapor equilibrium and work of adhesion simulations were carried out at constant volume, constant temperature, and constant number of particles with the Berendsen thermostat[31] (coupling constant 0.2 ps) at 300 K. All calculations were performed with a cutoff distance of 1.4 nm. A time step of 0.5 fs was used for the atomistic simulations because a fully flexible model including the flexibility of the CH bonds was employed. A value of 1 fs was employed in the CG simulations. This value was chosen through preliminary calculations in the microcanonical ensemble in which it was found to lead to proper conservation of the total energy. In the atomistic simulations, no-long range correction to the Lennard-Jones interactions was used. The particle-particle particle-mesh scheme as implemented in LAMMPS was employed to account for the long-range electrostatic interactions in the atomistic simulations.

III. MODELS

A. Atomistic model

We now discuss reference properties of the all-atom model of *n*-hexane that we later compare with the properties of the CG model. The all-atom Optimized Potential for Liquid Simulations (OPLS) model[32] of *n*-hexane was employed to carry out the atomistic simulations. Simulations were performed to obtain the liquid density of the model at 300 K. To this end, a simulation cell containing 1000 molecules was prepared with PACKMOL[33] near liquid density. The box was elongated in the z direction as discussed in Section II and only the z component of the pressure tensor was coupled to the barostat. The system was first relaxed to its target density. Subsequent runs of 500 ps were performed to obtain the average liquid bulk density reported in Table I. It can be seen that the OPLS model leads to a fair agreement with experiment. The simulation cell used for the bulk simulation was elongated in the z direction to generate a system where liquid and vapor are in equilibrium as explained in Section II. The simulations with the liquid-vapor equilibrium were performed at constant volume. The system was relaxed during 5 ns. A subsequent simulation of 35 ns was used to obtain the average liquid and vapor mass densities, as well as the liquid surface tension γ_{LV}. γ_{LV} was obtained from the spatial integration of the stress-tensor anisotropy through $\gamma_{LV} = L_z/2\,(\langle P_N\rangle - \langle P_T\rangle)$ where L_z is the size of the system in the z direction and P_N and P_T are the stress tensor components normal and parallel to the interface, respectively.[34] The factor of two arises from the fact that the system has two liquid-vapor interfaces. The results of these calculations are reported in Table I. It can be seen that the surface tension of the atomistic model (AA) underestimates the experimental value by approximately 20%.

TABLE I. Properties of *n*-hexane both in its atomistic and 3-site coarse-grained representation. The symbol ρ denotes mass density. The errors are calculated as error on the mean obtained through block averaging.

Model	ρ_{Bulk} (kg/m^3)	ρ_{Liquid} (kg/m^3)	ρ_{Vapor} (kg/m^3)	γ_{LV} (mJ/m^2)
AA	636.0 ± 0.2	631.7	1.92	14.1 ± 1.9
CG	650.3 ± 0.3	650.4	3.18	13.3 ± 0.7
Expt.	653.1	653.0	0.77	17.8

The structure and thermodynamic properties of the interface between *n*-hexane and the graphene layers will be discussed in detail in Section V. The corresponding calculations were also performed at constant temperature, constant volume, and constant number of particles. The Lennard-Jones parameters for the carbon atoms of the graphene surface were taken from the OPLS force-field, too. The parameters of carbon for benzene were chosen, with no electrostatic charge. The energy parameter for the carbon atom of the graphene layers is denoted ε_{Cg}. Since all parameters are taken from that force-field, the geometric mixing rule applies for both the energy and distance parameters.

B. Coarse-grained potentials

The CG potentials for liquid *n*-hexane and for the interaction between *n*-hexane and graphite were obtained from the CRW approach. The CRW method has so far been used to calculate interaction potentials for coarse-grained models of liquids[25,35,36] and polymer systems[35] but calculating surface interactions is also possible without a large change of the method itself. The CRW procedure follows a strict bottom-up approach, meaning that the CG potential emerges naturally from the interactions in the underlying fine-grained (i.e., atomistic) model. The CRW pair potential $U_{CRW}(r)$ is a measure for the free energy change resulting from "turning-on" the direct pair interactions between two coarse-grained interaction sites given a distance r between the two sites. A straightforward way to calculate this interaction potential is using the thermodynamic cycle shown in Fig. 2. Configurations of a hexane molecule are sampled while the distance between a given CG mapping point of this hexane molecule and a CG mapping point of the surface is constrained. This operation is repeated for distances up to the cutoff. For the development of the interactions between two CG hexane molecules, we refer to the approach corresponding to the thermodynamic cycle shown in Fig. 1 of Ref. 35. During the molecular dynamics simulation, the force F_C acting on the distance constraint can be calculated by

$$F_C = \sum_a \sum_{b\neq a} \vec{F}_{ab} \cdot \vec{e}_{ij} \tag{1}$$

as the sum of all atomistic pair forces projected onto the distance vector between CG mapping points i and j.

The average of F_C is calculated for multiple distances and can be integrated to yield the reversible work required to move the CG sites from infinite distance to a distance r,

$$W(r) = -\int_{r_{max}}^{r} \langle F_C(R)\rangle\, dR, \tag{2}$$

where $\langle\ldots\rangle$ denotes a canonical ensemble average. The calculation of W is performed twice, with the direct interactions between the atoms contained in the CG-bead turned on and off, respectively. The CRW pair potential

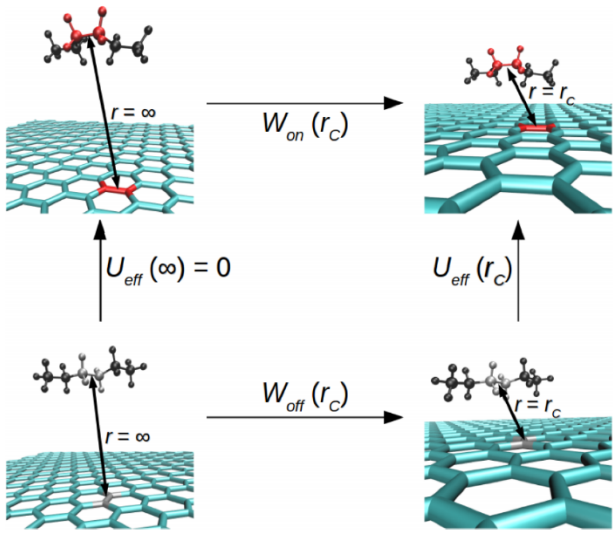

FIG. 2. Schematic illustration of the thermodynamic cycle used to calculate the CRW interaction potentials. Here, the interaction between a coarse-grained surface and a hexane bead containing the central carbon atoms and their adjacent hydrogen atoms is calculated (atoms merged into CG sites shown in red in the upper part). The distances between the centers of mass of those groups are varied and integration over the force on the constraint yields the PMF W_{on}. The same procedure is repeated with direct interactions between the atoms in the CG sites turned off (white color; lower half) to obtain W_{off}. The effective potential results as the difference between the two potentials of mean force. Pictures were generated using Visual Molecular Dynamics (VMD).[56]

results as the difference of the two contributions,

$$U_{CRW}(r) = W_{on}(r) - W_{off}(r). \quad (3)$$

We call the resulting potential conditional because it represents the interaction of the two CG beads *under the condition* that they are embedded within a larger molecule. The atomistic simulations required for the CRW calculations can be performed in the gas phase (with only the two molecules present) or in the liquid phase (with a surrounding bath of solvent molecules). The calculation in the liquid phase yields slightly better representability but is much more computationally demanding. However, it has been shown that gas phase calculations yield potentials that perform well in terms of representability and transferability for *n*-alkanes.[11,35,36]

We want to stress again that the calculations to obtain the CRW interaction potentials do not rely on converging properties of the CG model to a target value (as in, e.g., the Iterative Boltzmann Inversion (IBI),[37,38] Inverse Monte Carlo (IMC),[39] or MultiScale Coarse-Graining (MS-CG)[40] coarse-graining methods). The potentials emerge directly from interactions in the fine-grained representation of our system and therefore do not contain information on properties of the atomistic bulk. This fact will render our potentials physically meaningful and suitable for the use in the study of interface problems, as the use of pair potentials designed to reproduce bulk properties will probably be inadequate to model the behavior of a liquid in the vicinity of an interface.

All CRW potentials were calculated from gas phase molecular dynamics simulations with a sampling time of 20 ns and 25 ns for the hexane-hexane and surface-hexane interactions, respectively, using a time step of 0.5 fs. The calculations were performed with GROMACS 4.6.7[41] using the stochastic dynamics integrator with a reference temperature of 300 K and a thermostat coupling time of 2 ps. The distance between two CG interaction sites is constrained by the SHAKE-algorithm[42] and is varied from a value of 0.26 nm up to 1.4 nm in steps of 0.02 nm. For the atomistic interactions, the OPLS-AA force-field is used as mentioned above with a cut-off distance of 1.4 nm. No long-range correction is applied.

Hexane is coarse-grained using a three-site model with two beads (T-bead) representing the two terminal carbon atoms and one bead (M-bead) representing the two central carbon atoms, each including the respective adjacent hydrogen atoms (see, for example, Fig. 2 of Ref. 25). The intra-molecular interaction potentials (1 angle type and 1 bond type) are calculated by Boltzmann-inversion from the bond length and angle distributions sampled from a 100 ns molecular dynamics simulation of one hexane molecule in vacuum without any non-bonded interactions. The overall parameters for the simulations are only slightly different from those used in Ref. 25 where the OPLS united atom model for *n*-alkanes is used as fine-grained reference and the potentials are very similar to those obtained therein. The potentials exhibit the typical shape of CRW-calculated interaction potentials, i.e., they present a clearly distinct attractive and repulsive regime without fluctuations of interaction energy in the attractive tail, that are often observed when using structure-based CG methods. We have repeatedly argued that this "physical shape" of the interaction potentials is a key advantage of the CRW method because it allows for realistic simulation of energy fluctuations within the CG model, which in turn will lead to a good chemical and physical transferability of the model.[25,35,43] Calculations were conducted with LAMMPS using the same conditions as for the atomistic simulations above to characterize the bulk and liquid-vapor equilibrium properties. The results can be found in Table I. It can be seen that the CRW potentials tend to overestimate liquid and vapor densities at 300 K. However, fair agreement is observed between the atomistic and CG values as well as between the simulation and experimental data. It is interesting to note that the CG and all-atom models lead to similar values of γ_{LV} within statistical uncertainty.

We now discuss the mapping scheme of the graphene layers and their interaction with CG *n*-hexane. The surface interactions are calculated using the following mapping schemes in the CG model:

(1) An atomistic surface with a) $\varepsilon_{Cg} = 0.292\,88$ kJ/mol, which is the standard OPLS-AA value for aromatic carbon (model CG1) and b) $\varepsilon_{Cg} = 0.026\,778$ kJ/mol (model CG1-ob). The extension -ob stands for lyophobic.
(2) A coarse-grained surface using a 2:1 mapping of the surface (two bonded atoms are merged into one CG-site) shown in Fig. 3 using the same two ε_{Cg} values for the surface atoms in the CRW calculation (CG2 and CG2-ob, respectively).

Owing to the fact that the hexane-graphene system is mostly dominated by carbon-carbon interactions, it is

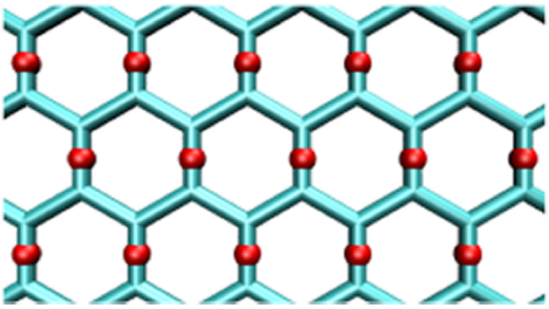

FIG. 3. Mapping used for the CG2 model of "graphite." A 1:2 mapping is used for the graphene sheets: the red spheres represent the positions of CG mapping points in the CG2 model. Picture generated using VMD.[56]

obviously expected that the system is lyophilic. We chose to optimize potentials with reduced interaction between hexane and the surface in order to study in a model way the behavior of lyophobic systems. The term lyophobic should be understood in the sense that the microscopic energy parameters lead to weakly attractive effective interaction between solid and liquid. Conversely, we denote as lyophilic the systems described by microscopic interactions that lead to a strongly attractive effective interaction between solid and liquid. These denominations are often used in the field of colloids and wetting.[44]

The potentials calculated at 300 K for the surface-liquid interaction are shown in Fig. 4. All potentials present a shape similar to the liquid interaction potentials with steep increase in the repulsive regime and a monotonically decaying attractive tail. As we may have expected, the potential minima are deeper when using the CG2 mapping scheme in which two surface carbon atoms are merged into an interaction site thereby increasing the number of atoms incorporated into the surface-liquid interaction. The characterization of these CG models in terms of solid-liquid interfacial structure and thermodynamics will be discussed and compared with the results obtained with the atomistic model in Section V.

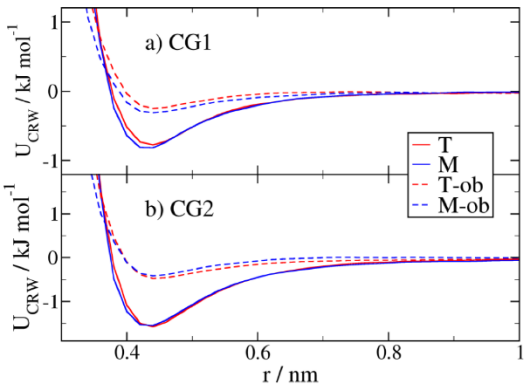

FIG. 4. Interaction potentials for the CG hexane model with the "graphite" surface interaction sites using surface mappings CG1 and CG2. Solid lines represent the interactions with surfaces represented by OPLS-AA carbon atoms while dashed lines represent the interaction with the lyophilic surfaces with modified Lennard-Jones parameters.

IV. SOLID-LIQUID WORK OF ADHESION

A. Theoretical background of the work of adhesion

The central thermodynamic quantity in our approach is the solid-liquid work of adhesion W_{SL}. The work of adhesion is generally defined as the reversible work per unit area to separate liquid and solid and to bring them at a distance where they no longer interact. Depending on the thermodynamic condition under which the separation is carried out, vapor adsorption may have to be taken into account in the definition of the work of adhesion.[45] If solid and liquid are separated in vacuum or under a condition such that vapor pressure is sufficiently low, vapor adsorption plays a negligible role and the work of adhesion is the solid-liquid work of adhesion W_{SL}. This quantity depends on the solid-liquid interfacial tension γ_{SL}, the solid surface tension γ_S, and the liquid-vapor interfacial tension γ_{LV} through the relationship

$$W_{SL} = \gamma_S + \gamma_{LV} - \gamma_{SL}. \tag{4}$$

In contrast, if vapor adsorption on the surface is significant, the separation of liquid and solid is performed in vapor and the work of adhesion is denoted by W_{SLV}.[45] It then depends on the solid-vapor interfacial tension γ_{SV} in addition to γ_{LV} and γ_{SL} through the relationship

$$W_{SLV} = \gamma_{SV} + \gamma_{LV} - \gamma_{SL}. \tag{5}$$

γ_{SV} and γ_S are related through $\gamma_{SV} = \gamma_S - \pi_{SV}(\Gamma)$ where $\pi_{SV}(\Gamma)$ is the surface pressure exerted by the excess amount of adsorbed vapor Γ.[46] For fluids with low vapor pressure, Γ is negligible and $\gamma_{SV} \approx \gamma_S$, such that $W_{SLV} \approx W_{SL}$. It should be noted that the work of adhesion is directly related to the wetting contact angle θ at the three-phase contact line that a drop of the given liquid forms on the given surface. In fact, the contact angle equation also depends on the interfacial tensions mentioned above,[45,46]

$$\gamma_{LV} \cos\theta = \gamma_{SV} - \gamma_{SL}. \tag{6}$$

Both contact angle and work of adhesion express the balance of interactions that drives the equilibrium behavior of a given solid-fluid system. However, contact angles cannot be used to characterize fully wetting systems, as no contact angle is measureable under this condition. There are other limitations associated with the use of droplets in studies of interfacial thermodynamics at the nanometer scale. The interested reader will find a discussion on this topic in the introduction of Ref. 26.

B. Dry-surface approach

The quantity that is calculated and discussed in the present work is the solid-liquid work of adhesion W_{SL}. On rigid substrates, as is the case here, interfacial tensions (force per unit length) can be identified to excess interfacial free energies (energy per unit area) because there is no plastic deformation of the solid upon separation of solid and liquid.[47] W_{SL} is then defined as the free energy change per unit area upon separating liquid and solid in vacuum or under negligible influence of vapor with respect to adsorption. Defining W_{SL} as a free energy change makes it possible to calculate this quantity using well

established free energy calculations methods. This approach was followed by one of us to establish the phantom-wall[48] and the dry-surface methodologies.[26] Following the latter approach, W_{SL} is calculated by thermodynamic integration as the free energy change per unit area to turn the actual solid-liquid interaction potential into a potential whose well is of negligible magnitude, such that the corresponding solid-liquid interaction is driven by the repulsive component of the potential. The algorithm was built on the observation that when water interacts with such a surface, it avoids it and forms a liquid-vapor like interface in its vicinity.[49] The interfacial tension of this effectively repulsive solid-liquid interface $\gamma_{SL,rep}$ was found to be approximately equal to the sum $\gamma_S + \gamma_{LV}$.[26,50] In other words, the free energy change per unit area of the transformation described above is $\gamma_S + \gamma_{LV} - \gamma_{SL}$, i.e., it is equal to the solid-liquid work of adhesion W_{SL}. Herein, we show that this result can be generalized to liquids other than water and exploit it in the framework of studies with CG models.

Following the dry-surface approach, we define state A as the state of the *n*-hexane-graphene layers surface such that the average total solid-liquid potential interaction energy $\langle \mathcal{U}_{\mathrm{SL,A}} \rangle$ is of the order of -10^{-2} mJ/m^2.[26] In practical terms, we consider that this condition is fulfilled when $\langle \mathcal{U}_{\mathrm{SL,A}} \rangle > -0.03$ mJ/m^2. We define state B as the state of the actual system whose solid-liquid work of adhesion is to be determined. It will be shown later that the magnitude of $\langle \mathcal{U}_{\mathrm{SL,B}} \rangle$ is orders of magnitude larger than $\langle \mathcal{U}_{\mathrm{SL,A}} \rangle$.The solid-liquid work of adhesion of the system in state B can be identified with the free energy change per unit area $\Delta F_{B\to A}/\mathcal{A}$ to achieve the reversible change from state B to state A under the condition that the interfacial tension of the system in state A fulfills the constraint $\gamma_{SL,A} = \gamma_S + \gamma_{LV}$. We will show later that this condition was met both in the atomistic and CG simulations of the *n*-hexane-graphene interfaces. To summarize, the solid-liquid work of adhesion W_{SL} is calculated as the free energy change per unit area $\Delta F_{B\to A}/\mathcal{A}$ to turn the system of interest from state B into state A: $W_{SL} = \Delta F_{B\to A}/\mathcal{A}$. We will discuss in Sections IV C and IV D how this transformation is implemented. In both cases, only the solid-liquid pair interaction potentials are explicitly affected by the transformation such that $\Delta F_{B\to A}$ is obtained through thermodynamic integration whose generic formula reads

$$\Delta F_{B\to A} = \int_{\lambda_B}^{\lambda_A} \left\langle \frac{\partial \mathcal{U}_{SL}}{\partial \lambda} \right\rangle d\lambda. \tag{7}$$

In Eq. (7), the bracket denotes an ensemble average (here the canonical ensemble), and λ is a parameter that describes the reversible path along which the transformation is performed.

C. Calculation through atomistic simulations

We now discuss in practical terms how thermodynamic integration is performed on the atomistic system in order to obtain $\Delta F_{B\to A}$. The parameter chosen to turn the actual surface (state B) into the effectively repulsive surface (state A) is the energy parameter of the surface carbon atoms $\varepsilon_{\mathrm{Cg}}$. This parameter couples to the liquid energy parameters through the geometric mixing rule. The transformation from B to A is performed by reducing $\varepsilon_{\mathrm{Cg}}$ from its value for the actual surface to a value small enough such that $\langle \mathcal{U}_{\mathrm{SL,A}} \rangle > -0.03$ mJ/m^2. We found that $\varepsilon_{\mathrm{Cg}} = 4.2 \times 10^{-6}$ kJ/mol led to this result. Note that even for such a small value, the repulsive branch of the potential remains, making the solid-liquid interaction effectively repulsive. The *n*-hexane liquid bulk systems described in Section II was brought into contact with the graphene surface. A simulation of 500 ps was performed with full interaction between solid and liquid, i.e., with $\varepsilon_{\mathrm{Cg}} = 0.292\ 88$ kJ/mol so as to equilibrate the system. The final configuration of this equilibration run was used as the initial configuration of different systems having each a different value for $\varepsilon_{\mathrm{Cg}}$ between 4.2×10^{-6} kJ/mol and 0.292 88 kJ/mol. An additional run of 4.5 ns was performed. The last 2 ns was used for analysis as explained below. As mentioned above, the parameter that is modified to achieve the transformation from state B to state A is $\varepsilon_{\mathrm{Cg}}$. Owing to the fact that solid and liquid atoms interact through the Lennard-Jones pair potential, Eq. (7) leads to

$$\Delta F_{B\to A} = -\int_{\sqrt{\varepsilon_A}}^{\sqrt{\varepsilon_B}} \left\langle \sum_{i=1}^{N_L} \sum_{j=1}^{N_S} 4\sqrt{\varepsilon_i} \left[\left(\frac{\sigma_{ij}}{r_{ij}}\right)^{12} - \left(\frac{\sigma_{ij}}{r_{ij}}\right)^{6} \right] \right\rangle d\sqrt{\varepsilon_{C_g}}. \tag{8}$$

N_S is the total number of solid particles and N_L is the total number of liquid particles. We denote the quantity between brackets as I_{AA}. We show in Fig. 5 the variation of the integrand $\langle I_{AA} \rangle$ with respect to $\sqrt{\varepsilon_{C_g}}$. The variation is smooth enough such that the integration can be performed using the trapezoidal rule. The two values of $\varepsilon_{\mathrm{Cg}}$ which define system AA and system AA-ob are 0.292 88 kJ/mol and 0.026 778 kJ/mol, respectively. We report in Table II the values of $\Delta F_{B\to A}/\mathcal{A}$ and of its energy component $\Delta U_{SL}/\mathcal{A}$. Because the total number of particles and temperature are held constant, ΔU_{SL} is obtained from the difference in average solid-liquid interaction energy $\langle \mathcal{U}_{\mathrm{SL,A}} \rangle - \langle \mathcal{U}_{\mathrm{SL,B}} \rangle$. The physical meaning of this quantity will be discussed later in detail.

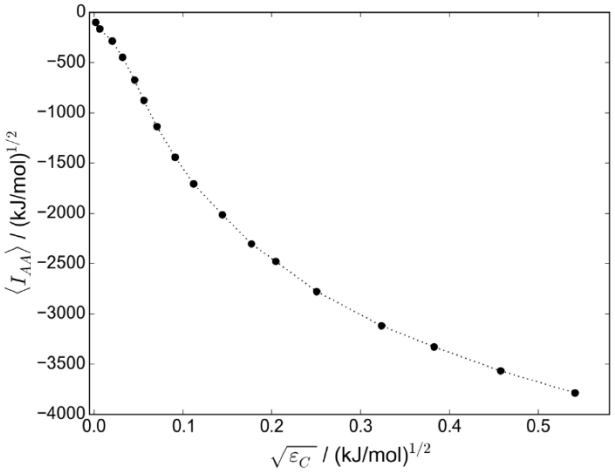

FIG. 5. Variation of the integrand for the calculation of the solid-liquid work of adhesion in the atomistic simulations. The dashed line is a guide to the eye.

TABLE II. Solid-liquid work of adhesion and its energy component for the atomistic and coarse-grained systems. The quantities are given in mJ/m^2. Fitting parameters for the dependence of $\langle I_{CG}\rangle$ with respect to α. a is given in nm kJ/mol and b in nm.

System	$\Delta F_{B\to A}/\mathcal{A}$	$\Delta U_{SL}/\mathcal{A}$	a	b
AA	122 ± 2	181	...	...
AA-ob	17.4 ± 0.2	31.3	...	...
CG1	192 ± 2	249	2116.4 ± 2.8	0.9708 ± 0.0037
CG1-ob	88.8 ± 0.9	115	1231.4 ± 3.6	1.2209 ± 0.0079
CG2	212 ± 2	274	2300.8 ± 4.0	0.9543 ± 0.0037
CG2-ob	37.6 ± 0.4	53.3	488.61 ± 2.9	1.1450 ± 0.0148

As mentioned above, $\Delta F_{B\to A}/\mathcal{A}$ can be identified with W_{SL} under the condition that the solid-liquid interfacial tension of the system in state A $\gamma_{SL,A}$ is such that $\gamma_{SL,A} = \gamma_S + \gamma_{LV}$. Note that it is irrelevant to define γ_S in the present study because the solid atoms are kept fixed and do not interact with each other. We thus take $\gamma_S = 0$.[51] Consequently, the condition above to identify $\Delta F_{B\to A}/\mathcal{A}$ with W_{SL} now writes $\gamma_{SL,A} = \gamma_{LV}$. The spatial integral of the average total stress anisotropy in state A with rigid substrates is equal to $\gamma_{SL,A} + \gamma_{LV}$. Indeed, the system contains a liquid-vapor interface in addition to the solid-liquid interface. We performed two independent simulations of 48 ns from which the stress tensor anisotropy analysis led to $\gamma_{SL,A} = 13.7 \pm 1.4$ mJ/m^2, which is in good agreement with $\gamma_{LV} = 14.1 \pm 1.9$ mJ/m^2 (Table I). We conclude that $\Delta F_{B\to A}/\mathcal{A} = W_{SL}$ within statistical uncertainty. Finally, it is observed that the hexane-graphene surface (system AA) is lyophilic, as expected, with W_{SL} having a value one order of magnitude larger than γ_{LV}. In contrast, the system AA-ob is lyophobic with W_{SL} of the order of γ_{LV}.

D. Calculation through coarse-grained simulations

The CG potentials arising from the CRW optimization are not analytical. Thus, thermodynamic integration has to be formulated in a way different than with the Lennard-Jones potential. However, the principle of the dry surface approach remains the same. The actual solid-liquid interaction potential must be turned into an effectively repulsive potential. This is implemented by reducing the depth of the potential well while preserving the repulsive part. This transformation is performed by multiplying the actual CG solid-liquid pair potential $v^0_{SL}(r)$ with a filtering function that maintains the repulsive component, but screens the attractive tail. For simplicity, this function is chosen here to be a decaying exponential of the inter-particle distance r such that

$$v_{SL}(\alpha, r_{ij}) = v^0_{SL}(r_{ij}) \exp(-\alpha r_{ij}), \tag{9}$$

where v^0_{SL} is the unperturbed potential as mentioned above and r_{ij} is the distance between the interacting particles i and j. For $\alpha = 0$, the actual potential is recovered: $v_{SL}(\alpha = 0, r_{ij}) = v^0_{SL}(r_{ij})$. When increasing values of α are used, the magnitude of v_{SL} at large distances is decreased, whereas the short distance values are less affected. Depending on the system, we found that values of α between 7 and 10 nm^{-1} were sufficient to lead to solid-liquid total interaction energies that were of the order of −0.01 mJ/m^2, as prescribed above for the definition of state A. State B of the thermodynamic integration for the CG systems is such that $\alpha = \alpha_B = 0$. The value of α_A was 9.5 nm^{-1} for both systems CG1 and CG2, and 7 nm^{-1} for both systems CG1-ob and CG2-ob. Finally, $\Delta F_{B\to A}$ for the CG systems is obtained from taking the derivative of the total solid-liquid interaction potential energy $\mathcal{U}_{SL}$ with respect to α. The following integral arises from this mathematical operation:

$$\Delta F_{A\to B} = -\int_{\alpha_A}^{\alpha_B} \left\langle \sum_{i=1}^{N_L} \sum_{j=1}^{N_S} -r_{ij} v^{CG}_{SL}(r_{ij}) \exp(-\alpha r_{ij}) \right\rangle d\alpha, \tag{10}$$

The brackets also denote an ensemble average in the canonical ensemble. We denote the quantity between brackets as I_{CG}. The simulations to obtain the variation of $\langle I_{CG}\rangle$ with respect to α were conducted as follows: The atomistic system was used to produce the CG liquid layer which was brought into contact with the atomistic and CG graphene surfaces with $\alpha = 0$. A simulation of 2.5 ns was performed to equilibrate the systems. The final configuration of the corresponding trajectory was then used as initial configuration for the simulations with different values of α in the range between 0 and 9.5 nm^{-1}. These simulations lasted 7.5 ns. The last 2.5 ns was used for analysis. We show in Fig. 6 the variation of the integrand $\langle I_{CG}\rangle$ with respect to α for the system CG1. As can be seen, an exponential function with the analytical form $a \exp(-b\alpha)$ fits the data very well. We report in Table II the results of the fitting parameters a and b for all CG systems. Similarly to the atomistic simulations, we calculated $\gamma_{SL,A}$ through the spatial integral of the average stress tensor anisotropy in order to understand whether $\Delta F_{B\to A}/\mathcal{A}$ as it is defined in Eq. (10) can be identified with W_{SL}. We found through simulations of 20 ns whose last 15 ns was used for analysis that $\gamma_{SL,A}$ was equal to 12.6 ± 0.6 mJ/m^2 for CG1 at $\alpha = 0.95$, 13.2 ± 0.6 mJ/m^2 for CG2 at $\alpha = 0.95$, 12.6 ± 0.6 mJ/m^2 for CG1-ob at $\alpha = 0.7$, and 13.2 ± 0.6 mJ/m^2 for CG2-ob at $\alpha = 0.7$. These results are in agreement with the value of γ_{LV} for n-hexane reported

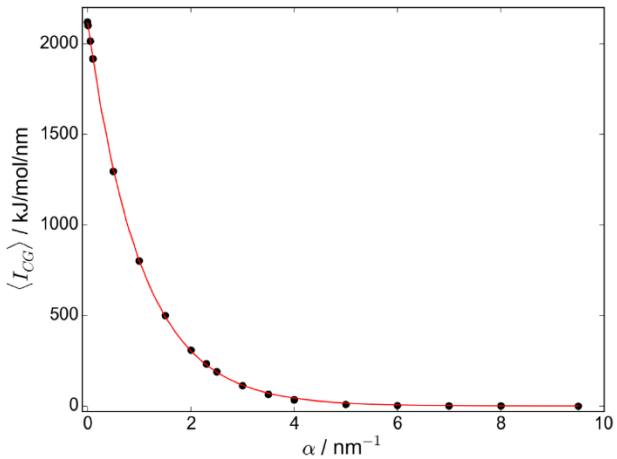

FIG. 6. Variation of the integrand for the calculation of the solid-liquid work of adhesion in the coarse-grained simulations. Result for the system CG1. The black circles represent the simulations data. The red line shows the mono-exponential fitting function.

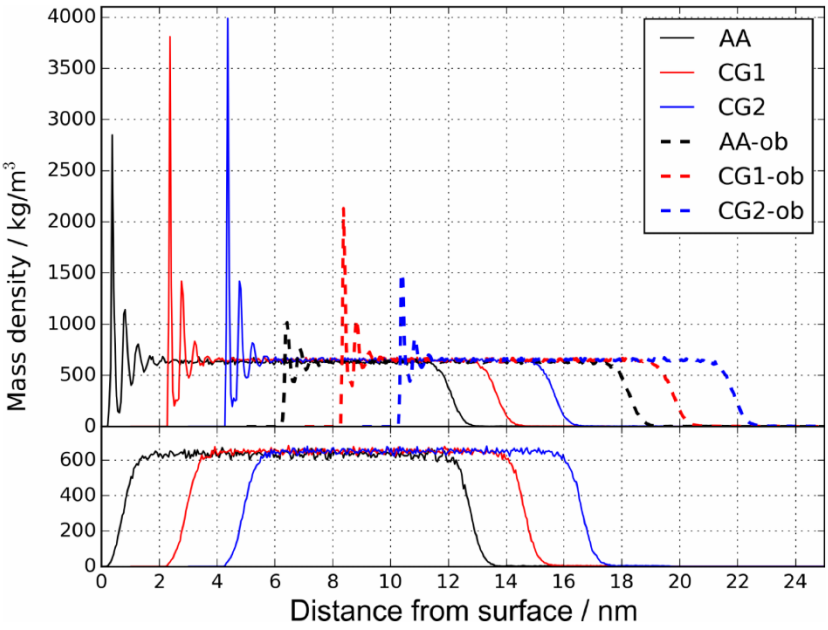

FIG. 7. Upper panel: Mass-density distribution of *n*-hexane perpendicular to the graphene surface. The black line describes the AA simulations results, the red line describes the CG1 simulations, and the blue line describes the CG2 simulation results. The dotted lines describe the systems AA-ob, CG1-ob, and CG2-ob with the same code colors as above. CG1, CG2, AA-ob, CG1-ob, and CG2-ob were shifted by 2, 4, 6, 8, and 10 nm along the x axis, respectively, for better readability. Lower panel: Spatial mass-density distribution of the AA (black), CG1 (red), and CG2 (blue) systems in their respective reference state (state A). The CG1 and CG2 curves were shifted by 2 and 4 nm, respectively, for better readability.

in Table I. Similarly to the atomistic systems above, we conclude that $\Delta F_{B\to A}/\mathcal{A} = W_{SL}$ within statistical uncertainty. For all systems in state A, it was found that the mass-density distribution in the vicinity of the surface was identical to the distribution close to the liquid-vapor interface, as is illustrated in the bottom panel of Fig. 7 for the systems AA, CG1, and CG2. Note that this behavior is reminiscent of the behavior of water.[26,49] This observation supports the result according to which the interfacial tension of the effectively repulsive interface is γ_{LV}, both in the atomistic and CG resolutions. We present in Table II the value of W_{SL} and $\Delta U_{SL}/\mathcal{A}$ for all CG systems. Further discussion on the magnitude of these quantities and a comparison with the atomistic values is carried out in Section V.

V. RESULTS AND DISCUSSION

We will start the discussion of our results by comparing the data for W_{SL} and $\Delta U_{SL}/\mathcal{A}$ obtained with the AA, CG1, and CG2 models (Subsection V A). Based on our findings, we continue with a more general discussion on the relation of the work of adhesion and its energy and entropy contributions in Subsection V B. Finally, we will propose a method to parameterize the solid-liquid interactions in a way that will enable us to reproduce W_{SL} correctly using a CG-CRW model.

A. Structure and energy of the solid-liquid interfaces

We compare the values of $\Delta U_{SL}/\mathcal{A}$ for the atomistic system AA and for the CG models CG1 and CG2 reported in Table II. $\Delta U_{SL}/\mathcal{A}$ represents the solid-liquid energy that is lost by a given system upon turning off the attractive tail of the solid-liquid interaction potential. Conversely, one may interpret $-\Delta U_{SL}/\mathcal{A}$ as the part of the energy that is gained by the system upon building solid-liquid contacts. Because $\langle \mathcal{U}_{\mathrm{SL,A}} \rangle$ is three to four orders of magnitude smaller than $\langle \mathcal{U}_{\mathrm{SL,B}} \rangle$, $\Delta U_{SL}/\mathcal{A}$ is numerically equal to $-\langle \mathcal{U}_{\mathrm{SL,B}} \rangle/\mathcal{A}$, i.e., the magnitude of the interfacial solid-liquid interaction potential energy. The stronger the solid-liquid interaction is, the larger $\Delta U_{SL}/\mathcal{A}$. It can be observed that both CG1 and CG2 lead to values of $\Delta U_{SL}/\mathcal{A}$ which are larger than for the corresponding atomistic system AA. Owing to their lyophilic character, the systems adopt a layer structure with intense maxima in the mass-density distribution next to the surface, as can be observed in the top panel of Fig. 7. Note that the positions of the maxima in the mass-density distribution are located at the same exact position in both the atomistic and CG resolutions. A similar behavior was observed in the case of polystyrene on gold for some of the polystyrene CG beads.[21] Moreover, the average mass-density values in the plateau region (for distances between approximately 2 and 11 nm from the surface) are identical to the mass-density values observed in the liquid-vapor equilibrium simulations. It can be seen that the intensity of the first maximum at 0.37 nm follows the same order as the value of $\Delta U_{SL}/\mathcal{A}$ for AA, CG1, and CG2, namely, CG2 > CG1 > AA. The numerical results regarding $\Delta U_{SL}/\mathcal{A}$ for the CG potentials can thus be interpreted qualitatively. The more attractive the potential generated by the surface is, the larger the number of molecules in the corresponding well, and the larger the magnitude of $\langle \mathcal{U}_{\mathrm{SL,B}} \rangle/\mathcal{A}$ of the corresponding system. We can conclude that the potential generated by the surface in the AA system is weaker than in the CG cases. To validate this assumption, we show in the left panel of Fig. 8 the variation of the total interaction energy $E_{pot,SL}$ between a given *n*-hexane molecule at a given distance from the surface for AA, CG1, and CG2. This distance is defined by the z position of the bead M in the CG representation and the z position of the center of the bond between the third and fourth carbon atoms in the atomistic representation. It is interesting to observe that the curves for these three systems have very similar shapes. Similarly to the mass-density distribution, the ordering of the depth of the

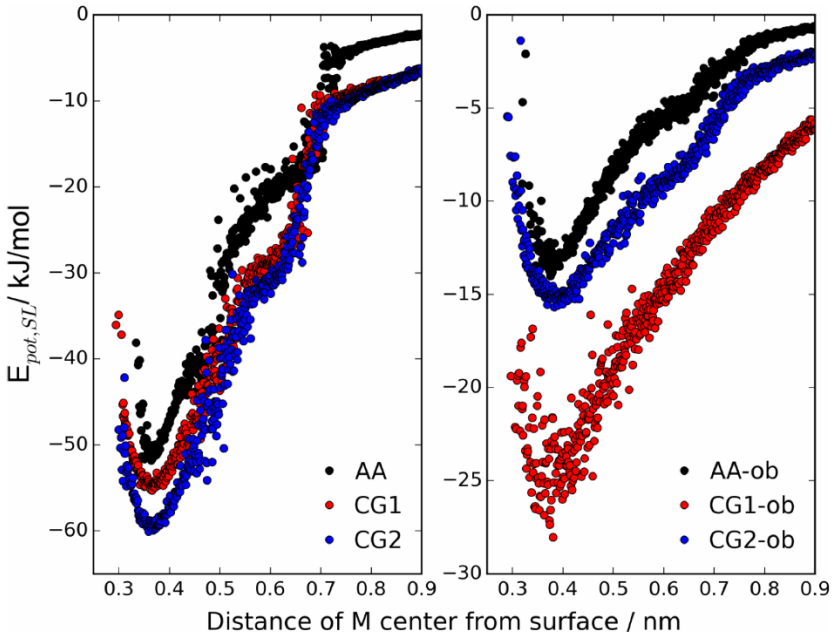

FIG. 8. Total interaction energy between of a given n-hexane molecule and the whole graphene surface $E_{pot,SL}$ depending on the distance of the M center of the molecules from the surface. In the CG representation, the M center is the M bead. In the atomistic representation, the M center is the center of the bond between the third and fourth carbon atoms. Each circle represents an instantaneous value of $E_{pot,SL}$ extracted from a 1.5 ns trajectory. Left: AA, CG1, and CG2 systems. Right: AA-ob, CG1-ob, and CG2-ob systems.

well of these energy curves follows what was observed for the magnitude of the first maximum that characterizes the layer structure, i.e., CG2 > CG1 > AA.

We now discuss the lyophobic system AA-ob, and the corresponding CG systems CG1-ob and CG2-ob. AA-ob is the atomistic system for which the boundary ε_B in the integral in Eq. (8) is 0.026778 kJ/mol. It can be seen in Table II that both CG1-ob and CG2-ob have values of W_{SL} larger than AA-ob. Considering the fact that W_{SL} for both CG1-ob and CG2-ob largely exceeds γ_{LV}, these systems cannot be qualified as lyophobic, in contrast to AA-ob. Contrary to CG1 and CG2, CG2-ob leads to a value of $\Delta U_{SL}/\mathcal{A}$ which is smaller than for CG1-ob. This behavior can be understood following the reasoning we have summarized above. Indeed, we found that $E_{pot,SL}$ for CG2-ob has a minimum of smaller intensity than CG1-ob but larger than AA-ob (right panel of Fig. 8). The ordering of the maxima in the mass-density distribution follows in a consistent way, as can be observed in Fig. 7 (top panel). We show in Section V B that $\Delta U_{SL}/\mathcal{A}$ is the largest component of W_{SL}; thus, the behavior of W_{SL} in Table II can be understood following the qualitative arguments we have developed above concerning $\Delta U_{SL}/\mathcal{A}$.

B. Energy gain relative to entropy loss of W_{SL} upon coarse-graining

To better understand the discrepancies between the CRW and AA models discussed above, and to find ways to improve the CRW models, we proceed discussing how the work of adhesion is affected by the properties of the external potential generated by the surface. It will be demonstrated how to devise improved CRW models, which represent $\Delta U_{SL}/\mathcal{A}$ in agreement with the atomistic model, and, by virtue of the form of the CRW potential, further provide a good representation of the solid-liquid energy fluctuations, which relate to the entropy contribution to W_{SL}.

First, we discuss the results for W_{SL} and its entropy component to complete our foregoing discussion on the interfacial energy behavior. In Table II, we have reported the values of W_{SL} for the end states of the thermodynamic integration. These states characterize the lyophilic systems (with full interaction) and the lyophobic atomistic as well as less lyophilic CG ones. However, it should be mentioned that the boundaries ε_A in Eq. (8) and α_A in Eq. (9) in our thermodynamic integration approach define reference states that are common to all the other values of ε_{Cg} or α for a given model. The states other than state A are defined through the other boundary of the integral. For example, ε_B = 0.292 88 kJ/mol defines system AA and α_B = 0 defines CG1 if the 1:1 mapping scheme is employed. Other values of these B-state boundaries define other systems. We conclude that W_{SL} can be made dependent on ε_B and α_B. We present in Fig. 9 the variations of W_{SL} and $\Delta U_{SL}/\mathcal{A}$ with respect to $\sqrt{\varepsilon_{C_g}}$ and α for the atomistic model and for the CG1 model, respectively. As suggested by the variation of the integrands of these curves in Figs. 5 and 6, respectively, the variation of W_{SL} is monotonic. Curves similar to the CG1 curves in Fig. 9 were obtained for the other CG systems (not shown). The results in Fig. 9 show that $\Delta U_{SL}/\mathcal{A}$ represents an upper boundary for W_{SL}. Similar behavior was observed by some of the present authors in the case of water on carbon surfaces[52,53] and of water on gold.[26] The important feature that drives this relationship is the connection between W_{SL} and $\Delta U_{SL}/\mathcal{A}$. In a study about the wetting properties of graphene,[52,53] some of us introduced the idea that the energy-entropy compensation that is known in solvation thermodynamics is also illustrated when studying systems such as solid-liquid interfaces. In fact, the surface may be considered as a solute, though extended. It is thus formally possible to show in the case of rigid substrates, as is the case here, that the change in internal energy arising from liquid-liquid interactions ΔU_{LL} upon disrupting the solid-liquid contacts is exactly compensated by

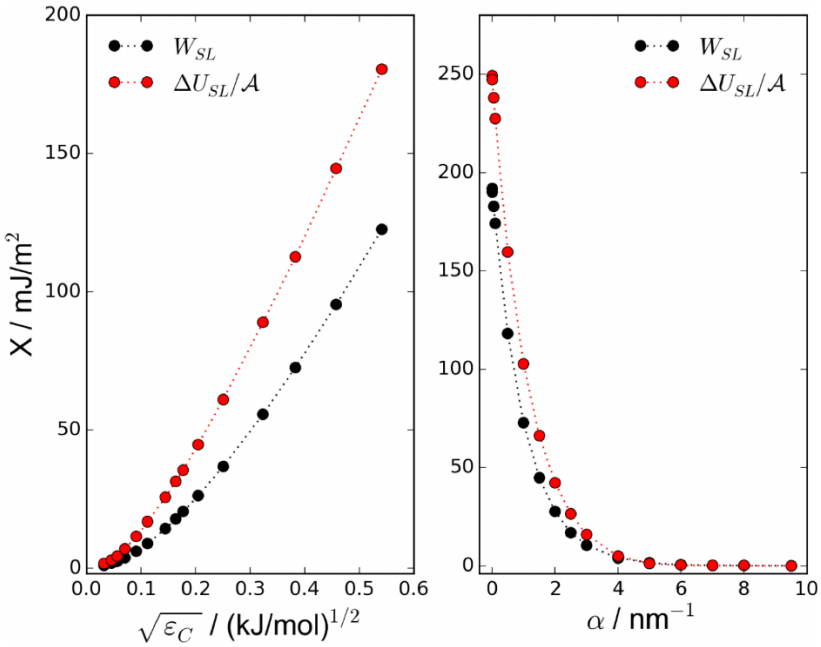

FIG. 9. Variation of W_{SL} (black circles) and of $\Delta U_{SL}/\mathcal{A}$ with respect to the thermodynamic integration parameter for the atomistic model (left) and for the CG1 system (right).

the corresponding entropy contribution $T\Delta S_{LL}$. It follows that W_{SL} only depends on the solid-liquid contributions, both in terms of energy and of entropy,[52,53]

$$W_{SL} = \frac{\Delta U_{SL}}{\mathcal{A}} - \frac{T\Delta S_{SL}}{\mathcal{A}}. \tag{11}$$

Note that for rigid substrates, there is no contribution of the solid-solid interactions to W_{SL} at all. While $\Delta U_{SL}/\mathcal{A}$ represents the energy per unit area lost by the system upon separating liquid and surface, $\Delta S_{SL}/\mathcal{A}$ is the entropy gained by the system during the same process.[52,53] The fact that liquid experiences a drastic change in its interfacial structure with corresponding changes in liquid-liquid interaction energies when it is separated from the surface has no influence on W_{SL} at a given temperature. However, the fact that ΔU_{LL} and $T\Delta S_{LL}$ are different from zero cannot be neglected if one wishes to understand the temperature variation of W_{SL}. The energy-entropy compensation discussed above is independent of the model for the solid-liquid surface. Thus, Eq. (11) holds for both the atomistic and CG systems.

We now address the question about how the process of coarse-graining modifies the balance between the energy loss $\Delta U_{SL}/\mathcal{A}$ and entropy gain $\Delta S_{SL}/\mathcal{A}$. The comparison between atomistic and CG results cannot be performed directly simply because the integration parameters ε_{Cg} and α do not even have the same dimension. Since we are interested in the ratio between ΔU_{SL} and $T\Delta S_{SL}$, we propose simply to plot W_{SL} against ΔU_{SL}. Indeed, Eq. (11) can readily be rewritten as follows:

$$\mathcal{A}W_{SL} = \Delta U_{SL}\left(1 - \frac{T\Delta S_{SL}}{\Delta U_{SL}}\right). \tag{12}$$

We show in Fig. 10 the suggested plot. The remarkable feature of Fig. 10 is that the variation of W_{SL} against $\Delta U_{SL}/\mathcal{A}$ can almost be described by a master curve. It is interesting to see that two different mapping schemes (CG1 and CG2) lead to the exact same dependence of W_{SL} with respect to $\Delta U_{SL}/\mathcal{A}$. Note that this curve only slightly deviates from the atomistic one. We can now quantify the ratio $T\Delta S_{SL}/\Delta U_{SL}$ for AA, CG1, and CG2, as well as for AA-ob, CG1-ob, and CG2-ob. These values are reported in Table III. It can be observed that the CG models tend to decrease the entropy gain compared to the energy loss. It is also interesting to note that the entropy contribution is actually not negligible at all. In fact, it may represent several tens of percent of W_{SL}. Moreover, the ratio $T\Delta S_{SL}/\Delta U_{SL}$ depends on the strength of the solid-liquid interaction. It decreases when the solid-liquid interaction becomes more attractive. This feature was also observed for water on non-polar surfaces.[52]

We now address the question of how the external field generated by a given surface affects $T\Delta S_{SL}$. To this end, we

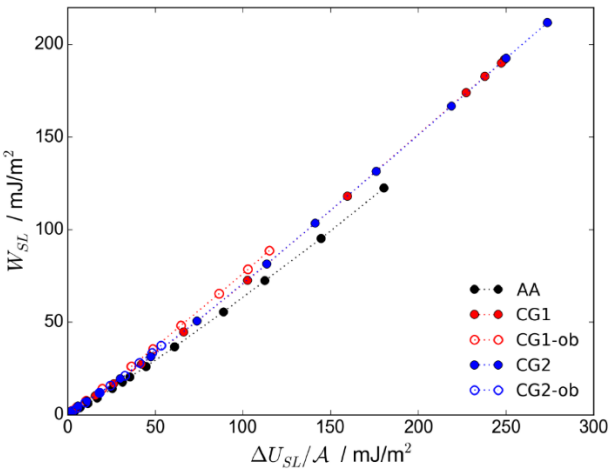

FIG. 10. Variations of the solid-liquid work of adhesion with respect to its energy component for all atomistic and coarse-grained systems. The dashed lines are guide to the eye.

TABLE III. Ratio between the entropy and energy components of the solid-liquid work of adhesion. The statistical uncertainty on each value is about 2%.

Model	$T\Delta S_{SL}/\Delta U_{SL}$
AA	0.325
CG1	0.229
CG2	0.226
AA-ob	0.444
CG1-ob	0.228
CG2-ob	0.295

apply the formalism of Yu and Karplus[54] to Eq. (7) in order to obtain the following relationship for $T\Delta S_{SL}$:

$$T\Delta S_{SL} = \frac{1}{k_B T}\int_{\lambda_B}^{\lambda_A}\left[\left\langle \mathcal{U}_{SL}\frac{\partial \mathcal{U}_{SL}}{\partial \lambda}\right\rangle - \langle \mathcal{U}_{SL}\rangle\left\langle \frac{\partial \mathcal{U}_{SL}}{\partial \lambda}\right\rangle\right] d\lambda. \quad (13)$$

It is interesting to note that $(\partial \mathcal{U}_{SL}/\partial\lambda)\, d\lambda$ has the dimension of energy. This is true independently of whether integration is performed with ε_{Cg} or with α. Therefore, the qualitative reasoning we develop applies to both levels of resolution. Because $(\partial \mathcal{U}_{SL}/\partial\lambda)\, d\lambda$ has the dimension of energy, the integrand in Eq. (13) is closely related to the variance of $\mathcal{U}_{SL}$: $\langle \mathcal{U}_{SL}^2\rangle - \langle \mathcal{U}_{SL}\rangle^2$. We conclude that the behavior of $T\Delta S_{SL}$ may be qualitatively understood from the fluctuations of $\mathcal{U}_{SL}$ for a given surface characterized by a given value of ε_{Cg} or α. We report in Fig. 11 the standard deviation of $\mathcal{U}_{SL}$ for all atomistic and CG systems, i.e., for all tested values of ε_B or α_B. The second order nature of $\langle \mathcal{U}_{SL}^2\rangle - \langle \mathcal{U}_{SL}\rangle^2$ leads to relatively scattered data. It can clearly be seen, however, that the all-atom systems lead to broader distributions of solid-liquid interaction energies than the CG models for the most attractive interfacial interactions. The difference is relatively small, though. It is understandable that the all-atom systems lead to distributions of $\mathcal{U}_{SL}$ values broader than the CG models. The all-atom

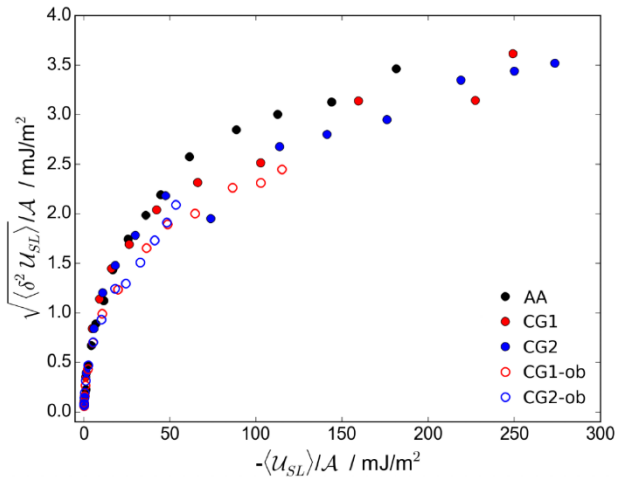

FIG. 11. Standard deviation of the total solid-liquid potential interaction energy per unit area with respect to the magnitude of this quantity for all the atomistic and CG systems. Each data point corresponds to a given B-state of the thermodynamic integration.

representation leads to a landscape of intermolecular energies rougher than the coarse-grained representation due to the additional atomistic degrees of freedom. It is also interesting to note that the results for the CG1 and CG2 mappings seem to fall on the same curve. This observation is consistent with the behavior of W_{SL} shown in Fig. 10. The fact that W_{SL} for the CG models varies similarly with respect to ΔU_{SL} and that the all-atom results deviate only weakly from the CG curve suggests that the energy landscape generated by the graphene layers is relatively smooth. Such a result has recently been observed through *ab initio* calculations on the water-graphene system.[55] The potential energy curves in Fig. 8 also support this interpretation because they all have very similar shapes, with the exception of CG1-ob. According to the behavior of the variance of $\mathcal{U}_{SL}$, we conclude that for a given value of ΔU_{SL}, the CG models should lead to a value of $T\Delta S_{SL}$ smaller than the atomistic one. Under this condition, Eq. (12) shows that W_{SL} for the CG models are larger than for the atomistic one. This is exactly what is seen in Fig. 10, thus supporting our reasoning.

The discussion above shows that the energy component $\Delta U_{SL}/\mathcal{A}$ and the entropy component $T\Delta S_{SL}/\mathcal{A}$ of the solid-liquid work of adhesion W_{SL} have a clear connection to the actual solid-liquid interaction energy $\mathcal{U}_{SL}$. In fact, $\Delta U_{SL}/\mathcal{A}$ is the average of the magnitude of this quantity. Given the width of the well of the potential energy curve $E_{pot,SL}$ shown in Fig. 8 (about 0.2 nm), it is reasonable to assume that $\mathcal{U}_{SL}$ is mostly influenced by the depth of the potential generated by the surface and by the number of molecules in the first adsorbed layer. $T\Delta S_{SL}/\mathcal{A}$ is defined in the exact mathematical terms through Eq. (13). It may, however, be qualitatively understood from the variance or the standard deviation of $\mathcal{U}_{SL}$. This quantity relates to the roughness of the intermolecular solid-liquid energy landscape. These considerations lead to recommendations that one may follow in the development of CG potentials that aim to reproduce the interfacial thermodynamics of a given solid-liquid system in terms of solid-liquid work of adhesion. Starting from the reference atomistic potential energy curve $E_{pot,SL}$, one must ensure that the corresponding CG curve has a well depth of similar magnitude, but also a similar shape in order to ensure appropriate energy fluctuations. Note that the liquid density fluctuations in the adsorbed layers play an important role as they are at the origin of the energy fluctuations. This observation provides with another indication on how to choose the CG model for the liquid. Our study, especially Fig. 10, suggests that the nature of the mapping scheme is irrelevant as far as W_{SL} is concerned for a given value of $\Delta U_{SL}/\mathcal{A}$. In fact, we conclude that different mapping schemes used with the same liquid CG model should lead to similar values of W_{SL} under the condition that the dependence of $E_{pot,SL}$ with respect to the distance from the surface is used as a constraint in the CG solid-liquid pair interaction potentials development. Fig. 12 (left) clearly demonstrates the validity of this assumption for the comparison between CG1 and CG2. We show $E_{pot,SL}$ for the two CG mappings (CG1, CG2) at values of α (0.4622 nm^{-1} and 0.5757 nm^{-1}, respectively) obtained from the fitting parameters a and b in Table II. The values of α were chosen such that the CG models reproduce W_{SL} for the atomistic

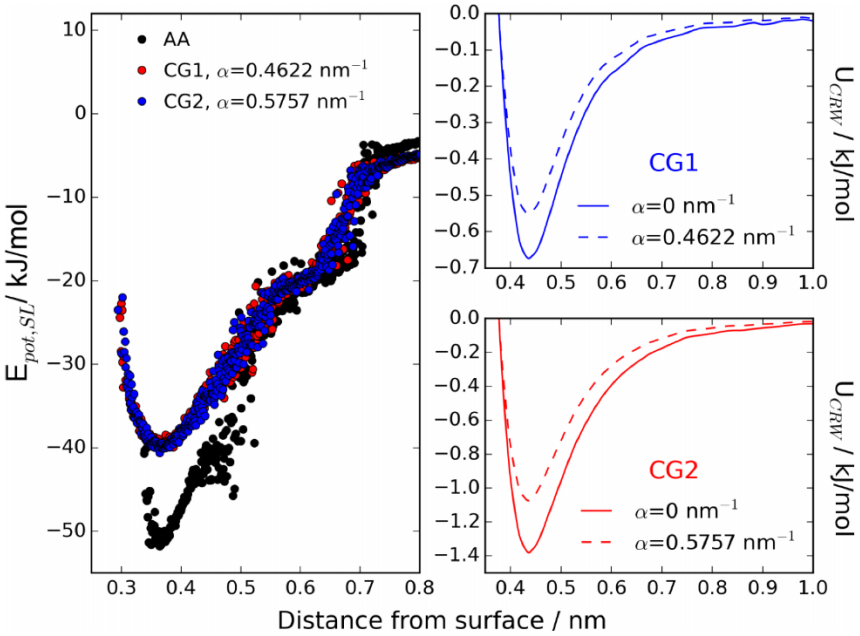

FIG. 12. Left: Comparison of the interfacial total interaction energy $E_{pot,SL}$ between a given n-hexane molecule whose M center is at a given distance from the surface for the atomistic (AA) and the models CG1 and CG2 at values of W_{SL} equal to the atomistic reference (122 mJ/m^2). The corresponding values of α are 0.4622 nm^{-1} and 0.5757 nm^{-1}, respectively. Right: CRW pair potentials for the surface-T bead for CG1 (upper panel) and for the CG2 (lower panel). The solid lines represent the actual potentials ($\alpha = 0$) and the dashed lines represent the screened potentials with values of α as mentioned above.

reference (122 mJ/m^2). The overlap between the two curves is indisputable. The corresponding values of $\Delta U_{SL}/\mathcal{A}$ are 164.7 mJ/m^2 and 164.3 mJ/m^2, respectively. The $E_{pot,SL}$ data of the AA model are included for comparison. The adjoining sub-figures in Fig. 12 (right) show the corresponding CRW potentials for the T bead. Note the difference in the width and depth of these potentials.

We finally remark that $\Delta U_{SL}/\mathcal{A}$ and the corresponding fluctuations allow us to qualitatively understand the performance of a coarse-grained model. The entropic contributions to the free energy are significant and only a coarse-grained model that not only has a similar potential well but also similar shape is essential in order to reproduce the free energy. Moreover, the CRW method combined with the dry-surface approach establishes a precise way to tune the coarse-grained model so one can retain the thermodynamic consistency with the all-atom system (Fig. 12), whereas, in a strict bottom-up approach one does not have a straightforward way to restore entropy due to the lost degrees of freedom.

VI. CONCLUSIONS AND OUTLOOK

We have proposed an approach to characterize the solid-liquid interfacial thermodynamics of atomistic and coarse-grained systems through their solid-liquid work of adhesion. The dry-surface method was employed to this end. This approach was applied to the interface between n-hexane interacting with graphene layers. Two mapping schemes were chosen to generate coarse-grained potentials using the conditional reversible work methodology. In the first CG model, n-hexane modeled through a three-bead model interacted with the surface in its atomistic representation. In the second CG model n-hexane represented with the same three-bead model interacted with the graphene surface represented through a model in which two carbon atoms were mapped into a CG interaction site.

The CG models were characterized by solid-liquid interactions that are more intense than the atomistic reference one. Consequently, CG n-hexane responds by forming a layer structure whose intensity is in line with the intensity of the solid-liquid interaction. More attractive interaction induces the presence of a larger number of molecules at positions where they in turn contribute favorable interacting energies with the surface.

The analysis of the energy and entropy components of the solid-liquid work of adhesion highlighted the role of the solid-liquid interaction energy fluctuations. We arrived at the conclusion that CG potentials which aim to reproduce atomistic reference values of the solid-liquid work of adhesion should be developed under the constraint that they reproduce not only the scale of solid-liquid intermolecular energies but also their fluctuations. These fluctuations determine the entropy of the work of adhesion which may represent several tens of percent of the solid-liquid interaction energy. The role of the solid-liquid energy fluctuations seems to be particularly important for the construction of coarse-models to describe systems with heterogeneous solid-liquid energy landscapes.

Owing to the fact that the wetting behavior of droplets is driven by the same thermodynamic quantities as the work of adhesion, our approach should find a natural extension in the field of wetting phenomena. It should also be useful in the development of chemically realistic coarse-grained potentials of systems whose behavior is dominated by solid-liquid interactions. This includes colloids, nanofluids, nanocomposites, and polymer-surface contacts.

ACKNOWLEDGMENTS

We are grateful for financial support from the Collaborative Research Center Transregio TRR 146 Multiscale Simulation Methods for Soft Matter Systems funded by the Deutsche Forschungsgemeinschaft. We also would

like to thank the HPC Center of Technische Universität Darmstadt for allocating computer time on the Lichtenberg-Hochleistungsrechner and to the John von Neumann Institute for Computing at the Jülich Supercomputing Center for allocating computer time on JURECA. FL thanks Aoife Fogarty for fruitful discussions and for her help in the preparation of the manuscript.

[1]A. C. Balazs, T. Emrick, and T. P. Russell, Science **314**, 1107–1110 (2006).
[2]M. Moniruzzaman and K. I. Winey, Macromolecules **39**(16), 5194–5205 (2006).
[3]P. M. Ajayan and J. M. Tour, Nature **447**(7148), 1066–1068 (2007).
[4]M. Okamoto, Mater. Sci. Technol. **22**(7), 756–779 (2006).
[5]G. S. Grest and K. Kremer, Phys. Rev. A **33**(5), 3628–3631 (1986).
[6]J. Sarabadani, A. Milchev, and T. A. Vilgis, J. Chem. Phys. **141**(4), 044907 (2014).
[7]J. Baschnagel, K. Binder, P. Doruker, A. A. Gusev, O. Hahn, K. Kremer, W. L. Mattice, F. Müller-Plathe, M. Murat, W. Paul, S. Santos, U. W. Suter, and V. Tries, Adv. Polym. Sci. **152**, 41–156 (2000).
[8]T. Murtola, A. Bunker, I. Vattulainen, M. Deserno, and M. Karttunen, Phys. Chem. Chem. Phys. **11**(12), 1869–1892 (2009).
[9]C. Peter and K. Kremer, Faraday Discuss. **144**, 9 (2010).
[10]L. Y. Lu and G. A. Voth, Adv. Chem. Phys. **149**, 47–81 (2012).
[11]E. Brini, E. A. Algaer, P. Ganguly, C. Li, F. Rodriguez-Ropero, and N. F. A. van der Vegt, Soft Matter **9**, 2108 (2013).
[12]S. Riniker, J. R. Allison, and W. F. van Gunsteren, Phys. Chem. Chem. Phys. **14**(36), 12423–12430 (2012).
[13]W. G. Noid, J. Chem. Phys. **139**(9), 090901 (2013).
[14]S. J. Marrink, H. J. Risselada, S. Yefimov, D. P. Tieleman, and A.H. de Vries, J. Phys. Chem. B **111**, 7812–7824 (2007).
[15]S. O. Nielsen, G. Srinivas, and M. L. Klein, J. Chem. Phys. **123**, 124907 (2005).
[16]E. Forte, A. J. Haslam, G. Jackson, and E. A. Müller, Phys. Chem. Chem. Phys. **16**, 19165–19180 (2014).
[17]M. Müller, B. Steinmüller, K. C. Daoulas, A. Ramírez-Hernández, and J.J. de Pablo, Phys. Chem. Chem. Phys. **13**, 10491–10502 (2011).
[18]K. Johnston, R. M. Nieminen, and K. Kremer, Soft Matter **7**, 6457 (2011).
[19]L. Delle Site, C. F. Abrams, A. Alavi, and K. Kremer, Phys. Rev. Lett. **89**, 156103 (2002).
[20]L. Delle Site, S. Leon, and K. Kremer, J. Am. Chem. Soc. **126**(9), 2944–2955 (2004).
[21]K. Johnston and V. Harmandaris, Macromolecules **46**, 5741–5750 (2013).
[22]A. Ghanbari, T. V. M. Ndoro, F. Leroy, M. Rahimi, M. C. Böhm, and F. Müller-Plathe, Macromolecules **45**(1), 572–584 (2012).
[23]M. Fukuda, H. Zhang, T. Ishiguro, K. Fukuzawa, and S. Itoh, J. Chem. Phys. **139**, 054901 (2013).
[24]T. T. Foley, M. S. Shell, and W. G. Noid, J. Chem. Phys. **143**, 243104 (2015).
[25]E. Brini, V. Marcon, and N. F. A. van der Vegt, Phys. Chem. Chem. Phys. **13**, 10468–10474 (2011).
[26]F. Leroy and F. Müller-Plathe, Langmuir **31**, 8335–8345 (2015).
[27]Z. Liu, K. Suenaga, P. J. F. Harris, and S. Iijima, Phys. Rev. Lett. **102**(1), 015501 (2009).
[28]J. K. Lee, S. C. Lee, J. P. Ahn, S. C. Kim, J. I. B. Wilson, and P. John, J. Chem. Phys. **129**(23), 234709 (2008).
[29]J. Tersoff, Phys. Rev. Lett. **61**(25), 2879–2882 (1988).
[30]S. Plimpton, J. Comput. Phys. **117**(1), 1–19 (1995).
[31]H. J. C. Berendsen, J. P. M. Postma, W. F. van Gunsteren, A. Dinola, and J. R. Haak, J. Chem. Phys. **81**(8), 3684–3690 (1984).
[32]W. L. Jorgensen, D. S. Maxwell, and J. Tirado-Rives, J. Am. Chem. Soc. **118**, 11225–11236 (1996).
[33]L. Martinez, R. Andrade, E. G. Birgin, and J. M. Martínez, J. Comput. Chem. **30**, 2157–2164 (2009).
[34]G. J. Gloor, G. Jackson, F. J. Blas, and E. de Miguel, J. Chem. Phys. **123**(13), 134703 (2005).
[35]E. Brini and N. F. A. van der Vegt, J. Chem. Phys. **137**, 154113 (2012).
[36]G. Deichmann, V. Marcon, and N. F. A. van der Vegt, J. Chem. Phys. **141**, 224109 (2014).
[37]P. Ganguly, D. Mukherji, C. Junghans, and N. F. A. van der Vegt, J. Chem. Theory Comput. **8**, 1802–1807 (2012).
[38]D. Reith, M. Pütz, and F. Müller-Plathe, J. Comput. Chem. **24**, 1624–1636 (2003).
[39]A. Lyubartsev and A. Laaksonen, Phys. Rev. E **52**, 3730–3737 (1995).
[40]W. G. Noid, J.-W. Chu, G. S. Ayton, V. Krishna, S. Izvekov, G. A. Voth, A. Das, and H. C. Andersen, J. Chem. Phys. **128**, 244114 (2008).
[41]B. Hess, C. Kutzner, D. van der Spoel, and E. Lindahl, J. Chem. Theory Comput. **4**, 435–447 (2008).
[42]J.-P. Ryckaert, G. Ciccotti, and H. J. C. Berendsen, J. Comput. Phys. **23**, 327–341 (1977).
[43]E. Brini, C. R. Herbers, G. Deichmann, and N. F. A. van der Vegt, Phys. Chem. Chem. Phys. **14**, 11896 (2012).
[44]Y. Yoon, D. Kim, and J.-B. Lee, Micro Nano Syst. Lett. **2**, 3 (2014).
[45]J. N. Israelachvili, *Intermolecular and Surface Forces*, 2nd ed. (Academic Press, 1991).
[46]L. J. M. Schlangen, L. K. Koopal, M. A. C. Stuart, and J. Lyklema, Colloids Surf., A **89**(2-3), 157–167 (1994).
[47]R. Shuttleworth, Proc. Phys. Soc., London, Sect. A **63**(365), 444–457 (1950).
[48]F. Leroy and F. Müller-Plathe, J. Chem. Phys. **133**(4), 044110 (2010).
[49]A. P. Willard and D. Chandler, J. Chem. Phys. **141**(18), 18C519 (2014).
[50]D. M. Huang, P. L. Geissler, and D. Chandler, J. Phys. Chem. B **105**(28), 6704–6709 (2001).
[51]E. S. Machlin, Langmuir **28**(49), 16729–16732 (2012).
[52]F. Taherian, F. Leroy, and N. F. A. van der Vegt, Langmuir **29**(31), 9807–9813 (2013).
[53]F. Taherian, V. Marcon, N. F. A. van der Vegt, and F. Leroy, Langmuir **29**(5), 1457–1465 (2013).
[54]H. A. Yu and M. Karplus, J. Chem. Phys. **89**(4), 2366–2379 (1988).
[55]G. Tocci, L. Joly, and A. Michaelides, Nano Lett. **14**, 6872–6877 (2014).
[56]W. Humphrey, A. Dalke, and K. Schulten, J. Mol. Graphics Modell. **14**(1), 33–38 (1996).

CHAPTER # 3

THE JOURNAL OF CHEMICAL PHYSICS **147**, 074702 (2017)

Thermodynamics of atomistic and coarse-grained models of water on nonpolar surfaces

Vikram Reddy Ardham[a] and Frédéric Leroy[b]
Eduard-Zintl-Institut für Anorganische und Physikalische Chemie, Technische Universität Darmstadt, Alarich-Weiss-Strasse 8, 64287 Darmstadt, Germany

(Received 28 April 2017; accepted 5 August 2017; published online 18 August 2017)

In order to study the phenomena where interfaces play a dominant role through molecular simulations, the proper representation of the interfacial thermodynamic properties of a given model is of crucial importance. The use of coarse-grained rather than atomistic models makes it possible to simulate interfacial systems with larger time and length scales. In the present work, we compare the structure and thermodynamic behavior of one atomistic and two single-site coarse-grained models of water on nonpolar surfaces, namely, graphite and the basal plane of molybdenum disulfide. The three models interact with the surfaces through Lennard-Jones potentials parametrized to reproduce recent experimental contact angle measurements. The models form a layered structure close to the surface, which is usually observed on sufficiently attractive nonpolar substrates. However, differences in the structure and thermodynamic behavior are observed between the models. These differences are explained by certain features of the water models, such as short range tetrahedral order and liquid density fluctuations. Besides these results, the approach employed in the present study may be used to assess the ability of coarse-grained models for solid-liquid systems to represent consistent interfacial thermodynamics. *Published by AIP Publishing.* [http://dx.doi.org/10.1063/1.4999337]

I. INTRODUCTION

The interaction of liquids or polymers with extended surfaces or solid nanoparticles plays a central role in soft-matter systems like emulsions and nanofluids. The interfaces formed at these heterogeneous systems play a major role in a wide variety of interesting phenomena like selective adsorption, assembly, or dispersion of particles, energy transport, apart from determining mechanical and rheological properties. Typically, these phenomena occur at length and time scales that are often out of reach of particle-based simulations with atomistic (AT) resolution. A possible approach to model these phenomena to access the relevant scales is by reducing the number of degrees of freedom of the models through coarse-graining. The resulting coarse-grained (CG) models are characterized by potential energy surfaces which, in general, greatly differ from the corresponding AT models. Consequently, not only the structure but also the thermodynamic and dynamic properties of CG models generally differ from those of the AT models. The process of coarse-graining is highly non-trivial, and during the last few decades, several methodologies have been developed to tackle the problem of deriving CG models or interactions for systems corresponding to specific interactions.[1–10] These developments have enhanced the understanding of complex systems like polymers and biological membranes. Relatively less has been done in the direction of developing coarse-graining methodologies for solid-liquid interactions or to understand how coarse-graining affects the representation of these interfaces.[11]

In the present work, the question of which important ingredients are necessary to construct AT or CG potentials that are thermodynamically consistent with experiments or reference models for solid-liquid systems is addressed. We focus on interfaces dominated by van der Waals interactions to discuss general principles. More precisely, liquid films of water on graphite and on the basal plane of a MoS_2 monolayer are studied. Structure and thermodynamic properties of water represented by an AT model are compared with the properties of two CG models. As will be explained in Sec. II, the CG water models employed have no explicit hydrogen bonds (HBs). We will show and explain why this lack of explicit HB representation has a minor influence on the interfacial liquid structure and interfacial thermodynamics. Coarse-grained potentials are by construction potentials of mean force[12,13] and are very often obtained by averaging out atomistic degrees of freedom through procedures detailed, for example, in Refs. 1–10. A typical example of such potentials was discussed by Mashayak and Aluru to describe the behavior of water in confinement between carbon and silica layers.[14,15] The CG models used in the present study were not obtained by such procedures. They were constructed and parametrized to reproduce experimental bulk liquid quantities and interfacial thermodynamic quantities. The comparison of their behavior is performed through quantities defined below. Nevertheless, this approach enables us to draw conclusions that are relevant to assess the behavior of CG models for solid-liquid interfaces in a broader sense.

The approach employed is based on the calculation of the solid-liquid work of adhesion W_{SL}. This quantity may be defined as the free energy change per unit area for separating a liquid and a solid in contact and for bringing these

[a] v.ardham@theo.chemie.tu-darmstadt.de
[b] f.leroy@theo.chemie.tu-darmstadt.de

two components at a distance where they no longer interact.[16] Under ambient conditions on surfaces with contact angle values around 60°-70° like on the basal plane of graphite or MoS_2, vapor adsorption is negligible.[17] Thus W_{SL} can be directly related to the wetting contact angle θ and the liquid surface tension γ_L through the Young-Dupré equation, which reads

$$W_{SL} = \gamma_L (1 + \cos\theta). \quad (1)$$

An advantage of addressing models for solid-liquid interactions through W_{SL} rather than through θ is because W_{SL} is a free energy change. This feature makes it simple to apply statistical thermodynamics to relate the collective behavior of molecules measured through W_{SL} to microscopic information like the interfacial liquid structure and interaction energies. In Sec. III, statistical thermodynamics is applied to give an expression that relates W_{SL} to solid-liquid interaction energies. As illustrated by the simulation results presented in Sec. IV, this expression plays an important role in understanding how the liquid structure and the density fluctuations in the vicinity of the interface that have been discussed in several publications[18,19] affect W_{SL} and consequently the wetting behavior of a given system. In Sec. IV, the limitations of the approach based on the determination of θ through droplet simulations to compare the wetting behavior of different models are discussed. To this end, a comparison of W_{SL} obtained from free energy calculations and from the independent determination of γ_L and of θ through simulations on nanometer sized cylindrical droplets is carried out.

To understand the thermodynamics of the models in more detail, the temperature dependence of W_{SL} is studied in the range between 298 and 348 K on monolayer MoS_2 and is presented in Sec. IV. It is found that the temperature transferability of quantities that depend on liquid-liquid interactions like density and surface tension play an important role in the temperature dependence of W_{SL}.

The simulation results are summarized in Sec. V. The underlying principles are discussed in a broader context to show how they may be used to assess the ability of given CG or AT models to describe the thermodynamics of solid-liquid interfaces.

II. METHODOLOGY

A. Calculation of the solid-liquid work of adhesion

Molecular dynamics (MD) simulations are performed to calculate the solid-liquid work of adhesion W_{SL} of water on nonpolar models for the basal plane of a monolayer of MoS_2 and graphite as well as the (111) surface of gold. This quantity is calculated following a thermodynamic integration approach as the reversible work per unit area to turn a given water-solid interface into an interface that is effectively repulsive.[20] In this process, the actual interface with the interfacial tension γ_{SL} is turned into an interface whose interfacial tension is to a good approximation $\gamma_S + \gamma_L$. The difference in free energy per unit area is thus $W_{SL} = \gamma_S + \gamma_L - \gamma_{SL}$.[16] Details about the corresponding methodology called dry-surface approach and examples with which it is used both with AT and CG models may be found elsewhere.[11,20–22] In order to calculate W_{SL}, a liquid film of water of approximate thickness 12 nm is in contact with the surface of interest. The other surface of the liquid film is free such that water is in equilibrium with its vapor. Note that under the conditions studied here, almost no water molecule is present in the vapor phase. The system is contained in a fixed volume V, with a constant number of particles N and its temperature T is maintained constant. The Lennard-Jones pair potential for the surface-water interaction is made dependent on a parameter λ such that the total water-surface interaction energy is

$$\mathcal{U}_{SL}(\lambda) = \lambda \sum_{i=1}^{N_L} \sum_{j=1}^{N_S} 4\varepsilon_{ij} \left[\left(\frac{\sigma_{ij}}{r_{ij}} \right)^{12} - \left(\frac{\sigma_{ij}}{r_{ij}} \right)^{6} \right]. \quad (2)$$

In Eq. (2), N_L is the number of water molecules, N_S is the number of surface particles, σ_{ij} and ε_{ij} are the distance and energy parameters for the Lennard-Jones interaction potential, respectively, and r_{ij} denotes the distance between two interacting particles. The scaling parameter λ quantifies the thermodynamic path along which the change from the actual interface to the effectively repulsive interface mentioned above is carried out. As mentioned in Ref. 22, Eq. (2) may be written in the following form:

$$\mathcal{U}_{SL}(\lambda) = \lambda \mathcal{U}_{SL}(1), \quad (3)$$

where $U_{SL}(1)$ is the expression for $\mathcal{U}_{SL}(1)$ at $\lambda = 1$ in Eq. (2). The quantity W_{SL} is obtained following the formalism of thermodynamic integration from:

$$W_{SL} = W_{SL}(\lambda) = -\frac{1}{\mathcal{A}} \int_{\lambda_0}^{\lambda} \left\langle \mathcal{U}_{SL}(1) \right\rangle_{N,V,T,\lambda'} d\lambda'. \quad (4)$$

The quantity $\mathcal{A}$ in Eq. (4) is the cross-sectional area of the water-substrate interface. The bracket refers to an ensemble average in the canonical ensemble at a given value of λ'. Note that W_{SL} depends on the upper boundary of the integral λ. For $\lambda = 1$, W_{SL} is the work of adhesion on the surface with the interaction parameters in Table I, whereas values with $\lambda < 1$ characterize systems with a weaker interaction between the water and surface. The parameter λ_0 quantifies the coupling between water and surface for the reference interface with interfacial tension $\approx \gamma_S + \gamma_L$. In practice, λ_0 is of the

TABLE I. Lennard-Jones pair interaction parameters between water and the atoms of different surfaces. The letter W in the subscripts refers to water. Water is described by the oxygen atom for SPC/E and by the CG interaction site for ELBA and mW.

Surface	Distance parameter (nm)	Energy parameter (kJ/mol)
MoS_2	σ_{MoW}/σ_{SW}	$\varepsilon_{MoW}/\varepsilon_{SW}$
	0.368 3/0.314 8	0.2540/1.484
Graphite	σ_{CW}	ε_{CW}
	0.335 25	0.4720
CG graphite	σ_{GW}	ε_{GW}
	0.335 25	0.9440
Gold	σ_{AuW}	ε_{AuW}
	0.289 75	3.7935

order of 10^{-3} and is chosen such that $\langle \mathcal{U}_{SL}(\lambda_0) \rangle \approx -0.01$ mJ/m^2.[20] About 15 values of λ' are used to calculate the integral in Eq. (4) through the trapezoidal rule.[21,22] The results of the calculations of the interfacial tension between the CG water models and the different surfaces presented in Sec. II B at $\lambda_0 = 0.001$ are given in the supplementary material. The comparison with the values of γ_L for the CG models shows that the approximation that the interfacial tension of the reference interface is approximately equal to $\gamma_S + \gamma_L$ is valid. Note that this assumption was already validated for SPC/E in other studies.[20,22]

B. Models and simulations

The MD simulations are essentially used to calculate the ensemble average for the integrand in Eq. (4) before the integration is performed to obtain W_{SL} as a function of λ. In addition, the simulation trajectories are employed to obtain structural properties of water at the interface on the different substrates. Water is modeled either with the AT model SPC/E[23] or with the CG models ELBA[24] or mW.[25] The models ELBA and mW are called single water CG models. They have a single interaction site that represents a single water molecule. Other CG water models called multiple water models have several water molecules mapped to a single CG particle.[26] Such models are not considered in the present work. The models ELBA and mW correspond to different ways of approaching intermolecular interactions in water. As mentioned by Orsi and Essex "*The ELBA water model is based on the general Stockmayer potential for polar fluids*,[27] *where a particle is represented by a Lennard-Jones soft sphere* (*providing excluded volume*) *embedded with a point dipole* (*to capture the electrostatics*)."[24] This model was parameterized against liquid water bulk density and diffusion properties at 303 K and 1 atm.[24] It has been extensively tested and was found to yield very good agreement between simulations and experiments for several values of bulk water properties.[28] Molinero and Moore who introduced the mW model mentioned that it "*is essentially an atom with tetrahedrality intermediate between carbon and silicon. mW mimics the hydrogen-bonded structure of water through the introduction of a nonbonded angular dependent term that encourages tetrahedral configurations*." This model was optimized to best describe the melting temperature and melting enthalpy of ice as well as the vaporization enthalpy and bulk liquid density.[25] Song and Molinero found, for example, that mW "*correctly represents the free energy of association of the methane pair, the temperature dependence of free energy, and the positive change in entropy and enthalpy upon association*."[29] It can be noted that with both ELBA and mW, water molecules interact through analytical potentials optimized against experimental data. Alternatively, the interaction between water molecules with single site CG models may be represented through potentials of mean force, like the one obtained by Wang *et al.* through iterative Boltzmann inversion.[30] Such a model is not considered here.

Independent of the model chosen, water interacted with the surfaces through the Lennard-Jones pair potential in Eq. (2). For the calculations involving SPC/E, water interacts with the surfaces through the oxygen atom. No explicit interaction between hydrogen and the surface atoms is considered. The Lennard-Jones parameters for the water-surface interactions are reported in Table I. These parameters are derived to reproduce the most recent experimental characterizations of the wetting behavior of water on the basal plane of MoS_2[22] and on highly ordered pyrolitic graphite[21] through wetting contact angle measurements. Note that it was recently shown that electrostatic charges on molybdenum and sulfur play no role on the wetting behavior of the basal plane of MoS_2 by water.[22,31] Thus a force-field solely based on the Lennard-Jones pair potential can be used to study the interfacial behavior of this particular system. The parameters for gold are taken from the force-field of Heinz *et al.*[32] In addition to the graphite surface where all carbon atoms are represented, the water CG models interacted with a CG surface of graphite will be denoted by CG graphite. The corresponding surface contains half the number of atoms of the graphite surface with full AT resolution. The particles of CG graphite are arranged in each graphene layer following the spatial distribution of the (001) plane of a face-centered cubic lattice with an interatomic distance of 0.245 95 nm. This distance corresponds to a carbon-carbon distance of 0.142 nm in the underlying AT resolution. The interlayer distance is set to 0.335 nm in both the AT and CG resolutions. The form of graphite with AB stacking is employed. The energy parameter between water and the interaction sites of CG graphite is increased by a factor two between the AT and CG resolutions, as can be seen in Table I. This value arises from the fact that there are twice less interaction sites within the CG surface than that in the AT one. In order to understand this particular point, the potential interaction energy $V(x,y)$ of a water molecule in the xy plane parallel to the surface for graphite and CG graphite at the height $z = \sigma_{CW}$ was calculated. The corresponding plots are reported in Figs. S1 and S2 of the supplementary material, respectively. They show that the differences between the greatest and lowest energies are 0.35 kJ/mol and 0.7 kJ/mol for water on graphite and CG graphite, respectively. Thus, the process of removing half of the surface particles in CG graphite without modifying their diameter increases corrugation of the surface in terms of interaction energies with water. However, for both graphite surfaces, the lowest interaction energy is −8.5 kJ/mol. When compared with the magnitude of the energy differences above, this value shows that the roughness of the energy landscape generated by the surface on water is of weak magnitude. The fact that $V(x,y)$ shows weak corrugation arises from the relatively large number density of the surface particles. As can be seen in Figs. S1 and S2 of the supplementary material, a given water molecule at $z = \sigma_{CW}$ interacts with tens of surface atoms in the interaction cutoff. We also calculated the effective interaction potential energy $V_{SL}(z)$ between a given water molecule and the whole surfaces depending on the distance from the surface z. To this end, the lateral contributions (in the xy plane) to V_{SL} are averaged out. The related plot is shown in Fig. S3 of the supplementary material. The curves for AT graphite and CG graphite are indistinguishable. This result shows that the increase by a factor 2 of ε_{CW} in the CG surface compared to the atomistic one exactly compensates the effect on $V_{SL}(z)$ of removing half of the graphite sites in CG graphite.

The simulation setup adopted for the AT simulations with SPC/E to obtain W_{SL} is the same as that in the articles published for water on MoS_2[22] and graphite.[21] For the reader's convenience, we report the values of N_L, N_S, and $\mathcal{A}$ as well as the simulation length for the trajectories corresponding to the calculation of the ensemble averages in Eq. (4) in Tables S1 and S2 of the supplementary material. Simulations are performed at varied temperatures which will be given in the text. Temperature is controlled with the Nosé-Hoover thermostat with a coupling constant of 0.2 ps for the AT simulations. For the CG simulations, the Langevin thermostat with a coupling constant of 1 ps is employed. The particles of the solid surfaces are kept fixed in all simulations.

Additional simulations are performed with water droplets to calculate the contact angle θ of the water models on monolayer MoS_2. The simulation setup employed in Ref. 22 is used with the same dimensions. Cylindrical droplets containing 10 000 water molecules are simulated on a rigid surface at temperatures that will be given in the text. The simulations started with droplets equilibrated at 298 K on a monolayer of MoS_2 with an initial value for θ of about 95°. This starting configuration is taken from a previous work by one of us.[22] The target temperature and water-MoS_2 potential parameters in Table I are applied to that initial configuration. These simulation conditions led θ to decrease, as will be discussed in detail in Sec. IV D. The droplets were considered in equilibrium when the position of their center of mass perpendicular to the surface was oscillating around an average value. Trajectories with a length of 7.5 ns after equilibration are employed to obtain the values of θ.

III. THEORETICAL BACKGROUND

Our goal is to understand how the choice of a given model for a given solid-liquid system, be it modeled with AT or CG resolution, influences the liquid interfacial structure and thermodynamic properties obtained in simulations. To this end, we discuss a microscopic expression which relates W_{SL} to the intermolecular interaction energies. Similar to the simulation setup discussed in Sec. II, the system under study is a liquid film adsorbed on a surface. The system is held at a constant temperature with a constant number of particles and constant volume. The film is in equilibrium with its vapor. The thickness of the film is at least one order of magnitude larger than the characteristic length of the surface-liquid interaction. The formalism of the canonical ensemble is used.

The quantity $\mathcal{U}_{SL}$ is the total surface-liquid interaction energy and is modeled in the present simulations through the Lennard-Jones potential [Eq. (2)]. The quantity $\mathcal{U}_L$ is the total liquid interaction energy. It contains both intra-molecular and liquid-liquid intermolecular contributions and thus depends on the features of the water models briefly described in Sec. II. In the formalism developed here, the surface atoms are assumed to vibrate around their crystallographic positions. These positions are assumed to be sensitive neither to the strength of the liquid-surface interaction nor to the changes in temperature. Thus, the surface acts as an external field on the liquid with a strength that varies only with the solid-liquid interaction energy. Those assumptions are of course only valid over a restricted range of temperature which must in principle be specified. They also correspond to relatively stiff solid surfaces. The main consequence of those assumptions is that the changes in the energy and entropy arising from the changes in the solid-solid interactions upon varying the magnitude of the coupling between the liquid and surface are neglected and do not appear in the formalism presented below.

As already discussed in Secs. I and II, W_{SL} is defined as the reversible work to separate a liquid and a solid initially in contact. It may also be interpreted as the reversible free-energy change per unit area to turn a given solid-liquid interface of interest into a reference where the solid and liquid are virtually uncoupled. This process can be produced by turning $\mathcal{U}_{SL}$ for an interface with the interfacial tension γ_{SL} into another solid-liquid interaction potential function, which yields an interface with the interfacial tension $\gamma_S + \gamma_L$. To this end, $\mathcal{U}_{SL}$ is made dependent on a parameter λ that quantifies the progression on the thermodynamic path between both interfaces. The Helmholtz free-energy change for a given solid-liquid interfacial area $\mathcal{A}$ for the process above is $\Delta F/\mathcal{A} = \gamma_S + \gamma_L - \gamma_{SL}$. The solid-liquid work of adhesion is thus obtained from $W_{SL} = \Delta F/\mathrm{A}$. Let us assume that the value $\lambda = \lambda_0$ defines the reference system whose interfacial tension is $\gamma_S + \gamma_L$. For a system with the interfacial tension γ_{SL} characterized by a given λ, the solid-liquid work of adhesion may be obtained through thermodynamic integration[33] from

$$W_{SL} = \frac{1}{\mathcal{A}}\left[F(\lambda_0) - F(\lambda)\right] = \frac{1}{\mathcal{A}}\int_{\lambda}^{\lambda_0}\left\langle\frac{\partial \mathcal{U}_{SL}(\lambda')}{\partial \lambda'}\right\rangle_{N,V,T,\lambda'} d\lambda'. \tag{5}$$

Following the approach of Yu and Karplus,[34] it can be shown that

$$\mathcal{A}W_{SL} = \langle \mathcal{U}_{SL}\rangle_{\lambda_0} - \langle \mathcal{U}_{SL}\rangle_{\lambda} - \frac{1}{k_B T}\int_{\lambda_0}^{\lambda}\left(\left\langle\frac{\partial \mathcal{U}_{SL}}{\partial \lambda'}\mathcal{U}_{SL}\right\rangle - \left\langle\frac{\partial \mathcal{U}_{SL}}{\partial \lambda'}\right\rangle\langle \mathcal{U}_{SL}\rangle\right) d\lambda'. \tag{6}$$

The meaning of the brackets in Eq. (6) and in the other related equations in the remainder of the text is the same as in Eq. (5). The subscripts are not reported for simplicity. Equation (6) will be employed for developing a microscopic understanding of the wetting behavior of the water models on the solid surfaces. We discuss and interpret it in detail below. Note that Eq. (6) is very general although it was initially employed to analyze the solvation thermodynamics of small solutes.[34] Owing to its generality, it can be extended to surfaces, i.e., larger solutes, as suggested in a work by the group of van der Vegt and one of us.[35]

It can be observed from Eq. (6) that W_{SL} depends on ensemble averages of $\mathcal{U}_{SL}$ and on an integral, which through its dimension closely relates to the variance of $\mathcal{U}_{SL}$. Note that the bracket for the ensemble average refers to the sampling of the configuration space by the liquid molecules and therefore refer to $\mathcal{U}_L$ in addition to $\mathcal{U}_{SL}$. However, Eq. (6) shows that understanding the behavior of W_{SL} with respect to λ for a given

model can be gained through the average and variance of the solid-liquid interaction potential energy. In order to understand that observation, it must be noted that the solid-liquid work of adhesion is a free energy change with an internal energy component $\Delta U/\mathcal{A}$ and an entropy component $T\Delta S/\mathcal{A}$. Following the same formalism that leads to Eq. (6),[34] it can be shown that

$$\Delta U = \langle U_{SL}\rangle_{\lambda_0} - \langle U_{SL}\rangle_{\lambda} - \frac{1}{k_B T}\int_{\lambda_0}^{\lambda}\left(\left\langle\frac{\partial \mathcal{U}_{SL}}{\partial \lambda'}\right\rangle\langle \mathcal{U}_L\rangle - \left\langle\frac{\partial \mathcal{U}_{SL}}{\partial \lambda'}\mathcal{U}_L\right\rangle\right)d\lambda' \quad (7)$$

and that

$$-T\Delta S = \frac{1}{k_B T}\int_{\lambda_0}^{\lambda}\left(\left\langle\frac{\partial \mathcal{U}_{SL}}{\partial \lambda'}\right\rangle\langle \mathcal{U}_L\rangle - \left\langle\frac{\partial \mathcal{U}_{SL}}{\partial \lambda'}\mathcal{U}_L\right\rangle + \left\langle\frac{\partial \mathcal{U}_{SL}}{\partial \lambda'}\right\rangle\langle \mathcal{U}_{SL}\rangle - \left\langle\frac{\partial \mathcal{U}_{SL}}{\partial \lambda'}\mathcal{U}_{SL}\right\rangle\right)d\lambda'. \quad (8)$$

It can readily be seen that the integral that depends on $\mathcal{U}_L$ in Eq. (7) is equal to the opposite of the part of the integral in Eq. (8) that depends on $\mathcal{U}_L$. This equality is a mathematical expression of the energy-entropy compensation associated with the rearrangement of the liquid molecules in the process where the liquid and substrate are uncoupled. In other words, when the interaction between a given liquid and a given substrate is changed, interfacial liquid molecules reorganize and changes in the liquid-liquid interactions follow. However, these changes do not contribute to W_{SL} because the related energy and entropy components are exactly equal.[34] Since only $\mathcal{U}_{SL}$ appears in the bracket in Eq. (6), we write $\mathcal{A}W_{SL} = \Delta U_{SL} - T\Delta S_{SL}$, where $\Delta U_{SL} = \langle \mathcal{U}_{SL}\rangle_{\lambda_0} - \langle \mathcal{U}_{SL}\rangle_{\lambda}$ and $T\Delta S_{SL}$ is equal to the integral in Eq. (6) divided by k_BT. Note that the energy-entropy compensation of solvent reorganization is an essential concept for understanding hydrophobic hydration.[36–39]

We now discuss ΔU_{SL} to highlight the important microscopic properties that influence this component of W_{SL}. Although the result in Eqs. (6)–(8) is in principle general, we will mostly discuss the particular case of water in the present manuscript. Because at $\lambda = \lambda_0$ water and surface weakly interact, $\langle \mathcal{U}_{SL}\rangle_{\lambda_0}$ is orders of magnitude smaller than $\langle \mathcal{U}_{SL}\rangle_{\lambda}$ for $\lambda >> \lambda_0$, thus $\Delta U_{SL} \approx -\langle \mathcal{U}_{SL}\rangle_{\lambda}$.[20] In order to estimate $\langle \mathcal{U}_{SL}\rangle_{\lambda}$, information is needed on the spatial distribution of the water molecules in the vicinity of the surface and on how these molecules contribute to the solid-liquid interaction energy $\mathcal{U}_{SL}$. The former property can be estimated by the average total number of water molecules $n_L(z)$ located at a given height z from the surface, whereas the latter is given by the interaction potential between a water molecule at a given distance z from the surface and the whole surface $V_{SL}(z)$. The approximation that V_{SL} only depends on z holds true for interfaces dominated by short-range interactions and with surfaces having a sufficiently large number density of particles. Indeed, for these interfaces, the surface appears energetically homogenous at the atomic scale, as was discussed in Sec. II B in connection with the Figs. S1 and S2 of the supplementary material. An estimate of ΔU_{SL} for a given water-surface coupling can thus be obtained from

$$\frac{\Delta U_{SL}}{A} \approx -\int_0^{r_{cut}} n_L(z)\, V_{SL}(z)\, dz. \quad (9)$$

In Eq. (9), r_{cut} is the cutoff distance employed in the simulations for the solid-water pair interactions. When the interaction between water and surface is dominated by van der Waals interactions, Lennard-Jones interaction pair potentials are often used like in the present study. If water is represented by a single interaction site as is often the case, the analytical form of $V_{SL}(z)$ can be obtained for crystalline or even amorphous systems,[40,41] as was illustrated for water on graphene.[35] Equation (9) shows that ΔU_{SL} also depends on $n_L(z)$, i.e., the ability of a given water model to pile molecules in the well of the interface potential V_{SL}. Obviously, this quantity is driven by the interactions between the water molecules. In fact, modeling $n_L(z)$ is a more complex task than modeling $V_{SL}(z)$. A discussion on models for $n_L(z)$ on nonpolar surfaces may be found in Sec. 4.3 of Ref. 20. From the discussion above, it can be concluded that two water models placed in the same external field $V_{SL}(z)$ may yield similar values of ΔU_{SL} if they generate similar spatial distributions of the water molecules.

We now discuss the entropy component $T\Delta S_{SL}$, which is defined from the integral in Eq. (6). Straightforward dimension analysis shows that the integrand has the dimension of the variance of $\mathcal{U}_{SL}$, i.e., $\left\langle \mathcal{U}_{SL}^2\right\rangle - \langle \mathcal{U}_{SL}\rangle^2$, as mentioned in Ref. 11. Thus $T\Delta S_{SL}$ depends on the fluctuations of the total solid-liquid interaction energy. On stiff and homogenous surfaces, the solid-liquid interaction potential V_{SL} is independent of time. Therefore, the fluctuations in $\mathcal{U}_{SL}$ mainly depend on the ability of a given liquid model to generate solid-liquid energy fluctuations. The basic mechanism underlying these fluctuations is related to the liquid density fluctuations in the layers adsorbed on the surface. The model for the liquid-liquid interactions is at the origin of these variations. It can be concluded that a given AT model and a given CG model interacting with the same solid-liquid interaction potential (as is the case here) may yield similar values of $T\Delta S_{SL}$ if the liquid-liquid interaction potentials in both cases lead to comparable solid-liquid energy fluctuations.

In Sec. IV, we show how the reasoning above on the energy and entropy of W_{SL} helps us to understand the behavior of the AT and CG models of water introduced in Sec. II on nonpolar surfaces. This study leads us to discuss general principles to analyze the behavior of CG models for solid-liquid systems.

IV. RESULTS

A. Reason for the layered structure of liquid water on non-polar substrates

We now discuss the structure of water on the basal plane of a single layer of MoS_2, on graphite, on CG graphite, and on gold. The behavior of the AT model SPC/E is compared with the CG models ELBA and mW. The average spatial distribution of the water number density $n_L(z)$ perpendicular to the surfaces is shown in Fig. 1 for MoS_2 and graphite

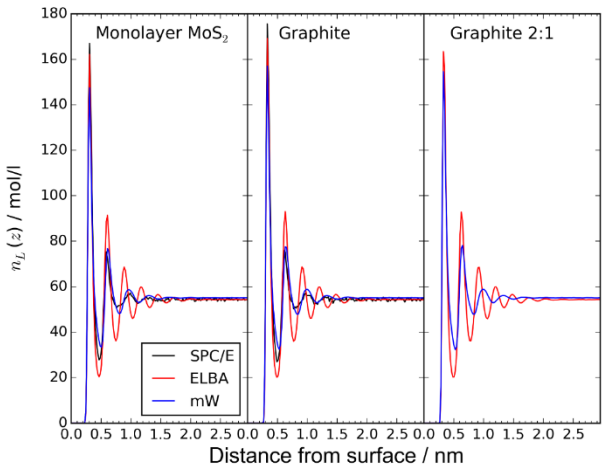

FIG. 1. Number density spatial distribution for different water models on the basal plane of monolayer MoS_2 (left), graphite (middle), and a coarse-grained model of graphite (right). The black, red, and blue colors refer to the water models SPC/E, ELBA, and mW, respectively.

and in Fig. S4 in the supplementary material for gold. These results are obtained at 323 K. It can be seen that the models all yield a typical layer structure of water that has been observed in numerous simulation studies on hydrophilic and mildly hydrophobic surfaces (see, for example, Refs. 18 and 42 among others). The first adsorbed layer is characterized by a maximum in number density at $z = 0.31$ nm from the surface on MoS_2 independent of the water model. This maximum appears at $z = 0.33$ nm on both AT and CG graphite surfaces independent of the water model. A second layer can be observed in all cases, with the position of the corresponding maximum for n_L that only weakly depends on the water model. A third maximum for $n_L(z)$ of weaker magnitude can be observed for all models on all surfaces. Further maxima are observed for the ELBA model. Moreover, the position of the third maximum for ELBA is located at a distance from the surface shorter than for SPC/E and mW. These observations show that the layer structure of ELBA is increased compared to the other models and that mW yields a layer structure strikingly similar to what is obtained for SPC/E. In fact, the intermolecular interaction potential in mW imposes by construction via a three-body Stillinger-Weber potential, a short-range tetrahedral arrangement of water molecules very much like the hydrogen-bonded tetrahedral arrangement observed in experiments, which in turn is constructed through the electrostatic interactions in the SPC/E model. We observed that the spatial distribution perpendicular to the surfaces of the tetrahedral order parameter[43] which measures the tetrahedral arrangement of water is similar for mW and SPC/E (not shown). In contrast, short-range tetrahedral structure is absent for the ELBA model at all distances from the surfaces, including in the region beyond the interfacial layered structure. Thus, due to the relaxation of this geometric constraint, the piling up of ELBA molecules next to the substrates takes another form than with mW and SPC/E, as illustrated in Fig. 1.

It is interesting to observe that for both CG water models, there is hardly any difference in the variation of $n_L(z)$ between graphite and CG graphite. Although both surfaces lead to different interaction energy landscapes for the water molecules taken individually next to the substrates (see Figs. S1 and S2 of the supplementary material), water molecules taken collectively behave as if both graphite and CG graphite were similar substrates. Both surfaces act on water as external fields regardless of the granularity of their structure, as was shown by the fact that $V_{SL}(z)$ are identical for both graphite surfaces (Sec. II B). Note that this result is in line with the work of Liu and Xu[44] later reproduced by Włoch *et al.*[45] who found that the contact angle of water nanodroplets on bilayer graphene is insensitive to the relative orientation of the two carbon monolayers. Independent of the resolution of the surface or of how the layers are oriented with respect to each other, the potential $V_{SL}(z)$ generated by the surface is the same because it is based on the short-range Lennard-Jones potential with surfaces having identical number densities. Indeed, the z-dependent potential is proportional to the number density of the solid,[35] which implies that if the density of the solid remains the same, the relative distribution of the masses should not play a major role in determining the mean field potential over the surface.

We now discuss the general microscopic mechanism that drives the formation of the water layers illustrated in Fig. 1. The free energy per unit area to bring a water film in contact with a given surface is the opposite of the work of adhesion, i.e., $-W_{SL}$. It was shown in previous simulation studies on water on nonpolar surfaces that the energy component of W_{SL} dominates its entropy term.[35,46,47] Thus minimizing the free energy for a given solid-liquid system can be understood through the minimization of the energy term $-\Delta U_{SL}$. Because $\Delta U_{SL} \approx -\langle \mathcal{U}_{SL} \rangle_\lambda$ (see Sec. II), the average solid-liquid energy $\langle \mathcal{U}_{SL} \rangle_\lambda$ controls the free-energy minimization when the solid and liquid are brought into contact. According to Eq. (9), only changes in the number of molecules at a given distance from the solid surface $n_L(z)$ can influence $\langle \mathcal{U}_{SL} \rangle_\lambda$ for a given solid-liquid potential V_{SL}, i.e., at a given λ. Therefore, the system maximizes the magnitude of $\langle \mathcal{U}_{SL} \rangle_\lambda$ by maximizing the number of liquid molecules at positions where V_{SL} is the most attractive, i.e., at the minimum of the well. On MoS_2 and graphite as well as on gold, the simulations show that the position of the minimum of V_{SL} coincides with the first maximum in $n_L(z)$ shown in Fig. 1. Therefore, the first adsorbed water layer is centered around the position of this minimum. Moreover, the width of the well of V_{SL} for the three surfaces mentioned above is of the order of the molecular diameter of water (see Fig. 3 of Ref. 21 for graphite and Fig. 5 of Ref. 22 for MoS_2). It can thus be anticipated that the average number of molecules in the first adsorbed layer n_{1L} plays a central role in determining the free energy of the solid-liquid interface.

The particular role played by n_{1L} suggested above is now discussed through the variation of n_{1L} depending on W_{SL}. For each model, the largest value of W_{SL} is obtained at $\lambda = 1$. The other results at lower values of W_{SL} correspond to water on surfaces with the structure of MoS_2, graphite, or gold but with decreased interfacial interaction strength. Note that when this interaction strength decreases, the intensity of the maxima in the water spatial distribution $n_L(z)$ decreases.[42] A given water molecule is considered to belong to the first adsorbed layer if

the oxygen atom for SPC/E or the interaction center for the CG models is at a distance from the surface lower than the minimum of $n_L(z)$ which for $\lambda = 1$ is found at $z \approx 0.5$ nm in Fig. 1. The result of this analysis is shown in Fig. 2. For clarity, we show only the data for the three water models on MoS_2 and for SPC/E on gold and graphite. It can be seen that for SPC/E on gold, $n_{1L} = 11.5$ nm^{-2}, whereas $n_{1L} = 10.5$ nm^{-2} on MoS_2 and on graphite. With the AT resolution of SPC/E, the variation of n_{1L} with respect to W_{SL} on the three surfaces takes the form of a narrow band on the plot. It can also be observed that $n_{1L} \approx 9.7$ nm^{-2} for SPC/E at $W_{SL} \approx 50$ mJ/m^2. This value of W_{SL} is what is observed in experiments on surfaces like hydrophobic polymers such as polyethylene or polytetrafluoroethylene which yield contact angle values of about 105°-110°.[48] That value of n_{1L} is only about 15% lower than on fully wettable surfaces like gold. We conclude that the difference in n_{1L} between surfaces with opposite wetting behavior (hydrophobic for polymers as opposed to hydrophilic for metals) varies in a narrow range compared to the corresponding range of values for W_{SL} (about one order of magnitude). This conclusion confirms that maximizing the number of molecules next to the surface is the basic microscopic mechanism by which the free energy of the solid-liquid system is minimized. It also explains why the intensity of the first maximum or the value of n_{1L} is a poor indicator of the wetting behavior of a given surface as noted by other authors (see, for example, the review by Jamadagni *et al.*[18]). It can be seen in Fig. 2 that ELBA leads to values of n_{1L} that are significantly lower than for SPC/E and mW. Moreover, Fig. 1 shows that the distance between the second and third water layers is shorter for ELBA than for the other two models. These two observations show that the ELBA molecules tend to pile up more closely perpendicular to the interface than SPC/E or mW but with a larger distance between the molecules within the layers. Although n_{1L} plays a crucial role in determining W_{SL}, molecules at larger distances from the interface within the interaction cutoff distance r_{cut} also have a contribution. The average number of water molecules within r_{cut} (1.2 nm) from the surface n_{rcut} is shown in Fig. 2 for MoS_2. This quantity is the average total number of molecules that contribute to $\langle \mathcal{U}_{SL} \rangle_\lambda$ at a given λ. It can be seen that n_{rcut} quickly increases with W_{SL} for all water models. Similar to the behavior of n_{1L}, it can be observed that both SPC/E and mW yield very similar variations of n_{rcut}, while ELBA tends to lead to lower values.

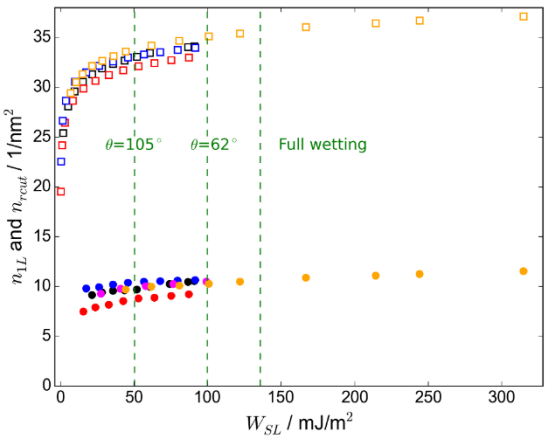

FIG. 2. Filled circles: Average total number of water molecules in the first adsorbed layer (n_{1L}) on MoS_2 surfaces. Empty squares: Average total number of water molecules within a distance of 1.2 nm from the surfaces (n_{rcut}). The black, red, and blue colors refer to the models SPC/E, ELBA, and mW, respectively. The orange and magenta colors refer to simulations of SPC/E on gold and graphite, respectively. The dashed green lines represent values of W_{SL} for which the corresponding experimental contact angles are 105° (W_{SL} = 50 mJ/m^2) and 62° (W_{SL} = 100 mJ/m^2) at 323 K. Systems for which $W_{SL} > 2\gamma_L$ = 135.8 mJ/m^2 have full wetting behavior with an apparent contact angle equal to 0°. The simulations corresponding to the data are performed at 323 K. The relative uncertainty on both n_{1L} and n_{rcut} is of the order of 0.1%.

To summarize the study on the structure of water quantified in Figs. 1 and 2, it can be concluded that the AT model and both CG models yield the typical oscillatory spatial distribution of water on surfaces that are sufficiently attractive. However, some discrepancies between ELBA and the other two models can be observed. These differences are related to the fact that ELBA imposes a short-range order that is more labile than with mW or SPC/E. In regard of Eq. (9), it is expected that the AT and CG models yield similar values of ΔU_{SL} and W_{SL}, as this quantity is dominated by its energy component. The corresponding simulation results are discussed in Sec. IV B. Finally, it should be mentioned that the layer structure tends to disappear when the coupling between the liquid and surface is weakened (see, for example, Fig. 10 of Ref. 42). Indeed, in the limit of very weak interactions, the system has no energy to gain compared to the reference free interface through the formation of liquid layers. As predicted by Eq. (9) and shown below, ΔU_{SL} takes small values in this limit.

B. How the layer structure influences interfacial thermodynamic quantities

In the foregoing discussion, it was shown that n_{1L} weakly increases with W_{SL}. We may even approximate it as a constant. Indeed, after a certain number of molecules are packed in the already dense first layer, excluded volume interactions come into play and deter more molecules from being packed or adsorbed in the same layer. Therefore, the incoming molecules are forced to adsorb in the adjoining layers. Given that the width of the well of V_{SL} is of the order of the size of a water molecule for Lennard-Jones potentials, it can be anticipated that the molecules of the first adsorbed layer have the largest contribution to $\langle \mathcal{U}_{SL} \rangle_\lambda$ and consequently to ΔU_{SL} and W_{SL}. Owing to the use of Lennard-Jones pair potentials, the depth of the well of V_{SL} is proportional to λ. This information combined with the idea that n_{1L} is roughly constant leads to the conclusion that ΔU_{SL} varies approximately linearly with λ. This is exactly what is shown in Fig. 3 for λ larger than 0.4 for AT and CG water on MoS_2, graphite, and CG graphite. Although n_{1L} is an important quantity to understand qualitatively the role of the liquid layer structure, n_{rcut} is more suitable to understand the overall variation of ΔU_{SL} with λ. Following the observation that the depth of the well of V_{SL} is proportional to λ, it is reasonable to assume that all water molecules within r_{cut} contribute to ΔU_{SL} with an energy value proportional to λ. Thus, one has $\Delta U_{SL}(\lambda) \propto n_{rcut}(\lambda)\,\lambda$. We

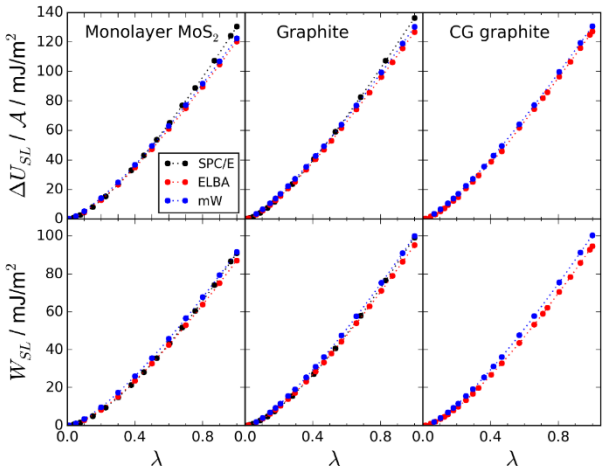

FIG. 3. Three top panels: Variation of $\Delta U_{SL}/\mathcal{A}$ against λ for the models SPC/E (black circles), ELBA (red circles), and mW (blue circles). Three bottom panels: Variation of W_{SL} against λ for the models SPC/E, ELBA, and mW. The same color code applies for all panels. In all cases, the dashed lines are a guide to the eye. The corresponding simulations are carried out at 323 K. The statistical uncertainty on W_{SL} at a given value of λ is of the order of 1%-2%. The statistical uncertainty on $\Delta U_{SL}/\mathcal{A}$ at a given λ is of the order of 0.1%-0.2%.

found that the variation of n_{rcut} with λ could be empirically described by $n_{rcut}(\lambda) = a \ln \lambda + b$, with $a = 3.19 \pm 0.07$ and $b = 33.8 \pm 0.1$ for SPC/E (see Fig. S5 in the supplementary material). This result leads to $\Delta U_{SL}(\lambda) \propto \lambda \ln \lambda^a + b\lambda$, whose analytical form is consistent with the curvature of the variations of ΔU_{SL} with λ in Fig. 3. Thus, the nonlinearity of ΔU_{SL} with λ is a direct consequence arising from the non-linearity of $n_{rcut}(\lambda)$.

We now discuss the variation of W_{SL} with λ shown in Fig. 3 for SPC/E, mW, and ELBA on MoS_2, graphite, and CG graphite. The trends obtained are essentially the same as for ΔU_{SL}. The rate at which W_{SL} increases with λ increases up to $\lambda \approx$ 0.4-0.5. Beyond this value, W_{SL} increases almost linearly with λ. This result is the consequence that ΔU_{SL} is the main contribution to W_{SL}. Note also that $\Delta U_{SL} > W_{SL}$, which implies that $T\Delta S_{SL} > 0$ as shown in previous studies.[34,46] Because γ_L is a constant for a given water model at a given temperature, the variation of $\cos\theta$ with λ follows the variation of W_{SL} against λ [Eq. (1)]. It is thus clear that $\cos\theta$ increases with λ in a non-linear way if the whole range of values for λ is considered. Such variations have been reported in several simulation studies, like Refs. 42, 47, and 49 or Ref. 50. However, to the best of our knowledge no explanation has been given to the deviation from linearity observed for the systems with the weakest liquid-substrate coupling. The reasoning above about how the variation of n_{rcut} with respect to λ influences ΔU_{SL} provides the basic explanation for the variation of W_{SL} and $\cos\theta$ against the solid-liquid coupling strength reported in the studies mentioned above.

It can be seen in Fig. 3 that although for a given λ, $\Delta U_{SL}/\mathcal{A}$ follows the order SPC/E > mW > ELBA on MoS_2 and graphite, W_{SL} follows the order mW ≈ SPC/E > ELBA on the same respective surfaces. Thus, the difference between W_{SL} and $\Delta U_{SL}/\mathcal{A}$ obviously depends on the water model. According to Eq. (6) and the related discussion in Sec. III, $T\Delta S_{SL}/\mathcal{A}$ is the distance between the curves for W_{SL} and $\Delta U_{SL}/\mathcal{A}$ at a given λ. The entropy $T\Delta S_{SL}/\mathcal{A}$ relates to the cumulated variance of $\mathcal{U}_{SL}$ between λ_0 and λ. It is thus expected that models that induce the largest values of the variance $\left\langle(\delta\mathcal{U}_{SL})^2\right\rangle = \left\langle\mathcal{U}_{SL}^2\right\rangle - \langle\mathcal{U}_{SL}\rangle^2$ have the largest values for $T\Delta S_{SL}/\mathcal{A}$. We compare in Fig. 4 the variations of $\left\langle(\delta\mathcal{U}_{SL})^2\right\rangle$ with respect to λ for SPC/E, ELBA, and mW on MoS_2. It can be seen that at a given λ, $\left\langle(\delta\mathcal{U}_{SL})^2\right\rangle$ follows the order SPC/E > ELBA > mW [Fig. 4(b)]. The same ordering is observed for $T\Delta S_{SL}/\mathcal{A}$ obtained from the difference $\Delta U_{SL}/\mathcal{A} - W_{SL}$ [Fig. 4(a)], confirming the expectation above. It can be noted that the magnitude of $T\Delta S_{SL}/\mathcal{A}$ is consistent with several experiments summarized in Ref. 51 for the available range of work of adhesion. The basic microscopic mechanism that influences the variation of $\left\langle(\delta\mathcal{U}_{SL})^2\right\rangle$ relates to the liquid density fluctuations in the vicinity of the substrate. The role of density fluctuations on hydrophobic hydration and on the wetting behavior of surfaces has been abundantly commented on (see Ref. 18 for a review). In short, it was found that water density "*fluctuations are enhanced near hydrophobic surfaces.*"[18] In connection with density fluctuations, Evans and successive co-workers recently suggested that liquid compressibility in the vicinity of a given surface may be "*a useful measure of solvophobicity and hydrophobicity.*"[19,50] These authors found that the compressibility of liquids perpendicular to surfaces depends on the distance from the surface. The spatial distribution of compressibility exhibits oscillations that are qualitatively similar to the oscillations in the spatial density distribution in Fig. 1. Evans and co-workers also found that liquid compressibility in the vicinity of a given substrate increases when the liquid-surface coupling is weakened. In the light of these findings, the behavior of $T\Delta S_{SL}/\mathcal{A}$ in Fig. 4(b) can be qualitatively explained through the comparison of the values for the isothermal compressibility of bulk water. This quantity at ambient conditions for SPC/E,[52] ELBA,[53] and mW[25] is ≈4.1 10^{-11} Pa^{-1}, ≈2.9 10^{-11} Pa^{-1}, and ≈1.9 10^{-11} Pa^{-1},

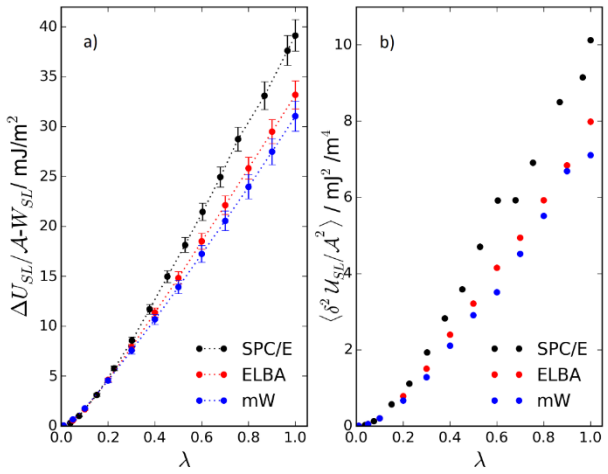

FIG. 4. (a) Variation of the entropy $T\Delta S_{SL}/\mathcal{A}$ with λ obtained from the difference $W_{SL} - \Delta U_{SL}/\mathcal{A}$ for the three water models. The dashed line is a guide to the eye. (b) Variation with λ of the variance of the solid-liquid interaction energy $\mathcal{U}_{SL}/\mathcal{A}$ for the three water models. The corresponding simulations are carried out at 323 K.

respectively. Assuming that the compressibility of the models in the vicinity of MoS_2 follows the same order as in the liquid bulk, the findings of Evans *et al.* and the statement of Jamagdani *et al.* quoted above imply that the magnitude of the water density fluctuations follow the order SPC/E > ELBA > mW, which is the order observed for $T\Delta S_{SL}/\mathcal{A}$. Finally, it can be seen that $\left\langle(\delta\mathcal{U}_{SL})^2\right\rangle$ is a monotonic function of the liquid-surface coupling parameter. Since this variance is straightforward to calculate, it may be used as a measure of the wetting nature (hydrophilic/hydrophobic) of a given surface that can complement the local compressibility analysis suggested by Evans *et al.*

To summarize the thermodynamic analysis above, we report in Table II the values of W_{SL}, $\Delta U_{SL}/\mathcal{A}$, and $T\Delta S_{SL}/\mathcal{A}$ with other thermodynamic quantities that will be discussed in Sec. IV C. At a given temperature, it can be seen that $\Delta U_{SL}/\mathcal{A}$ follows the order SPC/E > mW > ELBA. To explain this observation, we need to reconsider the structural properties discussed in Sec. IV A where it was shown that n_{1L} and n_{rcut} follow the order SPC/E ≈ mW > ELBA. Figure 1 shows that the position of the minimum around 0.5 nm is slightly shifted to larger distances for mW compared to SPC/E. Thus, the average number of water molecules in a narrow interval around the well of the potential V_{SL} is slightly lower with mW than with SPC/E. The energy change $\Delta U_{SL}/\mathcal{A}$ is lower for mW than for SPC/E because there are less molecules with mW that contribute with the lowest solid-liquid interaction energies. It can also be observed in Table II that $T\Delta S_{SL}$ follows the order SPC/E > ELBA > mW, which was explained through the behavior of the variance of $\mathcal{U}_{SL}$ and the compressibility of the water models. Combined, the variations of $\Delta U_{SL}/\mathcal{A}$ and $T\Delta S_{SL}/\mathcal{A}$ yield the observed values of W_{SL}. The models, mW and SPC/E have comparable $\Delta U_{SL}/\mathcal{A}$, but SPC/E induces larger fluctuations in $\mathcal{U}_{SL}$ and therefore the resulting values for W_{SL} follow the order mW > SPC/E. In conclusion, the liquid interfacial structure plays an important role as far as the solid-liquid work of adhesion is concerned, but fluctuations in energy need to be considered to explain the variation of W_{SL} between the water models.

TABLE II. Thermodynamic quantities obtained from the thermodynamic integration calculations of W_{SL} with respect to temperature. All quantities are given in mJ/m^2, except for $\Delta S/\mathcal{A}$, which is given in mJ/m^2 K.

	SPC/E (298 K)		mW (298 K)
W_{SL}	96.6 ± 1.4	...	94.8 ± 1.4
$\Delta U_{SL}/\mathcal{A}$	135.3 ± 0.2	...	125.2 ± 0.2
$T\Delta S_{SL}/\mathcal{A}$	38.7 ± 1.6	...	30.4 ± 1.5
$\Delta U/\mathcal{A}$	168 ± 3	...	133 ± 2
$\Delta U_L/\mathcal{A}$	32.8 ± 3.2	...	8.0 ± 1.6
$\Delta S/\mathcal{A}$	0.240 ± 0.015	...	0.129 ± 0.010
	SPC/E (323 K)	ELBA (323 K)	mW (323 K)
W_{SL}	90.9 ± 1.4	87.0 ± 1.3	91.4 ± 1.4
$\Delta U_{SL}/\mathcal{A}$	130.2 ± 0.2	120.2 ± 0.1	122.5 ± 0.1
$T\Delta S_{SL}/\mathcal{A}$	39.3 ± 1.6	33.2 ± 1.4	31.1 ± 1.5
$\Delta U/\mathcal{A}$	169 ± 3	170 ± 2	136 ± 2
$\Delta U_L/\mathcal{A}$	38.4 ± 3.2	49.3 ± 2.1	13.6 ± 0.6
$\Delta S/\mathcal{A}$	0.241 ± 0.014	0.255 ± 0.010	0.138 ± 0.009
	SPC/E (348 K)	ELBA (348 K)	mW (348 K)
W_{SL}	85.0 ± 1.3	80.6 ± 1.2	88.1 ± 1.3
$\Delta U_{SL}/\mathcal{A}$	124.2 ± 0.2	114.6 ± 0.1	119.6 ± 0.1
$T\Delta S_{SL}/\mathcal{A}$	39.3 ± 1.5	34.0 ± 1.3	31.5 ± 1.4
$\Delta U/\mathcal{A}$	169 ± 3	167 ± 2	137 ± 2
$\Delta U_L/\mathcal{A}$	45.0 ± 3.2	52.1 ± 2.1	16.9 ± 1.6
$\Delta S/\mathcal{A}$	0.242 ± 0.012	0.247 ± 0.009	0.139 ± 0.008

C. Temperature dependence of W_{SL}

We now discuss how temperature affects W_{SL}. The range of values between 298 and 348 K is considered. For the ELBA model, 298 K is too close to its melting point and therefore suspecting any possible metastable states, the results are not presented here, although nothing atypical that would indicate freezing of liquid has been observed in the simulations. We show in Fig. 5 the variation of W_{SL} with respect to T for the three water models on monolayer MoS_2. It can be seen that W_{SL} decreases with temperature, with $\Delta U > 0$ and $\Delta S > 0$. Assuming linear variation of W_{SL} with T as previously observed in simulations[35,47] and experiments,[51] a linear function is fitted to the corresponding data to obtain both $\Delta U/\mathcal{A}$ and $\Delta S/\mathcal{A}$. The values obtained are reported on the plot. The values for ΔU are also obtained from the trajectories of the thermodynamic integration calculations through the difference $\Delta U = \langle\mathcal{U}_{SL} + \mathcal{U}_L\rangle_{\lambda_0} - \langle\mathcal{U}_{SL} + \mathcal{U}_L\rangle_{\lambda=1}$ at the different temperatures. These estimates are employed to obtain $\Delta S/\mathcal{A}$ from the subtraction $(\Delta U/\mathcal{A} - W_{SL})/T$. The results of these calculations are reported in Table II. For all water models, it can be seen that good agreement is found between the results obtained with the linear fit and the results at the individual temperatures. This observation suggests that both the energy and entropy of adhesion $\Delta U/\mathcal{A}$ and $\Delta S/\mathcal{A}$ may be obtained with reasonable accuracy from the calculation of W_{SL} at a single temperature.

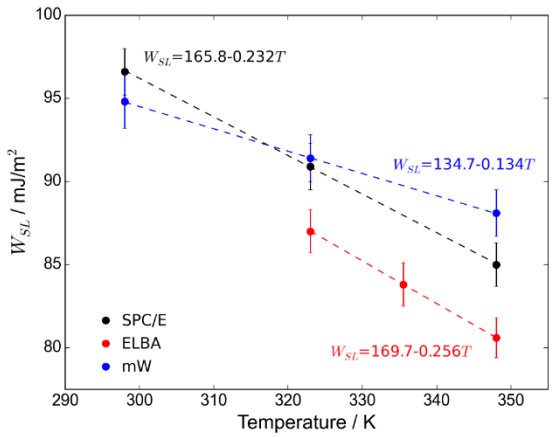

FIG. 5. Temperature dependence of W_{SL} for SPC/E (black circle), ELBA (red circle), and mW (blue circle). The dashed lines are linear fits to the data points. The equations are the results of these fits. The color code employed for the equation is the same as for the symbols. In all cases, the regression coefficient is very close to 1. The uncertainty on the fitting parameters in the equations is at most equal to 0.86%. The error bars on the data points are not considered in the fitting procedure.

It can be observed in Fig. 5 and Table II that both SPC/E and ELBA yield similar values for the entropy of adhesion on MoS_2 in the temperature range considered. The plot in Fig. 5 indicates that the adhesion energy of these models differs by 2%-3%. In contrast, SPC/E and mW yield values for $\Delta U/A$ with a larger difference. To understand these observations, we report the quantity ΔU_L in addition to ΔU_{SL} in Table II. The energy difference ΔU_L is the change in the liquid-liquid interaction energy when λ is decreased to λ_0. It quantifies the change in the liquid-liquid intermolecular interaction energy when the highly structured interface on the actual surface is turned into a liquid-vapor-like structure on the surface with λ_0. It can be noted that in all cases, $\Delta U_L > 0$. This result means that the liquid-liquid interaction is more favorable on the substrates than when the liquid and solid are uncoupled. Indeed, the molecules are arranged more closely in the adsorbed layers than at the liquid-vapor-like interface. It can also be seen that ΔU_L increases with temperature in all cases. To explain this observation, it is reasonable to assume that the ordered water distribution on the surfaces is less sensitive to temperature variations than the less structured liquid-vapor-like reference interface. Thus, the difference between $\mathcal{U}_L$ on the actual surface and on the reference interface at λ_0 increases with T. While ΔU_L increases with temperature for the three models, the magnitude of this quantity depends on the model. The fact that ELBA has the largest ΔU_L can be explained by the large change in the liquid structure when the actual solid-liquid interface (Fig. 1) is turned into a less structured interface at λ_0. In contrast, mW presents a maximum next to the liquid-vacuum interface that is not obtained with ELBA and SPC/E. Note that such a maximum is also visible in the density profiles for the TIP4P models as shown in Fig. S5 of the supplementary material of Ref. 28. This feature may explain why ΔU_L is lower for this model than for the other two. It is worth noting that although SPC/E and mW deliver very similar properties at 298 K, they behave in a quite different manner in the temperature dependence of these properties. The peculiar temperature dependence of mW should not come as a surprise, as this model was developed strictly to be used at room temperature. Compared with AT models, the temperature transferability of the properties of mW is hampered by its lack of rotational degrees of freedom. For example, differences between models in the temperature dependence of density were discussed in Ref. 25.

D. Droplet simulations

In the literature about water-surface interactions on nonpolar substrates, the wetting behavior of a given system is almost exclusively addressed through droplet calculations in which the contact angle θ of water nanodroplets is measured. In two recent publications,[21,22] one of us argued that quantitative comparison with experimental contact angle measurements requires at least that the surface tension γ_L of the liquid model in the droplet simulations equals the corresponding experimental value. Indeed, the shape of a droplet strongly depends on γ_L in addition to the solid-liquid interaction. Therefore it is unwise to try to reproduce a given experimental value of θ with a model that is not able to reproduce a quantity (γ_L) that drives the shape of the droplet. That requirement on γ_L is rarely met because liquid models are generally not optimized to reproduce this quantity and because size effects related to the curvature of both the liquid-vapor interface and the three-phase contact line are rarely quantified, not to say poorly understood. An example of the influence of the water model on γ_L is illustrated here again with ELBA and mW, which yield 74.8 mJ/m^2 (at 298 K) and 66 mJ/m^2 (at 300 K), respectively, according to Refs. 28 and 25. Note that γ_L = 60.6 mJ/m^2 at 298 K for the present SPC/E model[54] whereas γ_L = 72 mJ/m^2 at 298 K in experiments.[55] Because the influence of the water model on γ_L cannot be ignored, it was suggested that the wetting behavior of water models on a given nonpolar surface should be compared through W_{SL} rather than through θ.[21] The present work is an illustration that W_{SL} is influenced by the distribution of water molecules in the interaction potential generated by the surface and by the water-substrate energy fluctuations. Therefore, if two models have similar such properties, it is expected that they lead to similar values of the free energy of adhesion. We conclude that if two water models yield values of W_{SL} that differ by only a few percent points, but their γ_L values differ rather significantly, as is the case, for example, for SPC/E and ELBA at 323 K, it is expected that θ also strongly differs between both models [Eq. (1)]. Therefore, based solely on θ values obtained from droplet simulations, one could erroneously conclude that SPC/E and ELBA markedly differ in their solid-liquid thermodynamic behavior, while the difference arises from the difference in γ_L between the models, i.e., from the liquid-liquid interactions. We report in Table III the contact angle values θ_d measured in cylindrical droplet simulations as explained in Sec. II for the three water models at different values of T. We also report the result of our own determination of γ_L for the CG models. The values for SPC/E are taken from Ref. 54 with the procedure detailed in Ref. 22. As mentioned above, W_{SL} for SPC/E and ELBA differ only by about 4%, whereas the difference in γ_L amounts to approximately 20%. It should thus not be surprising to observe a difference of nearly 15° for θ_d between SPC/E and ELBA. Note also that mW yields values of θ_d intermediate between SPC/E and ELBA, in agreement with the variation of γ_L between the models.

The quantities W_{SL} and γ_L obtained from simulations correspond to flat interfaces. In contrast, the liquid-vapor interface

TABLE III. Contact angle and thermodynamic values from droplet and free energy calculations. The contact angles θ_d are given in degree (°). The surface tension γ_L and work of adhesion W_{SL} are given in mJ/m^2.

	SPC/E	ELBA	mW
θ_d (298 K)	55.1 ± 0.8	...	69.6 ± 0.6
θ_d (323 K)	54.4 ± 0.6	79.4 ± 0.6	70.1 ± 0.6
θ_d (348 K)	53.7 ± 2.0	78.5 ± 0.6	71.2 ± 0.5
γ_L (298 K)	60.6 ± 1.3	...	65.2 ± 1.4
γ_L (323 K)	57.0 ± 1.3	70.9 ± 0.5	63.4 ± 1.2
γ_L (348 K)	53.1 ± 1.3	65.9 ± 1.6	61.5 ± 1.2
$W_{SL,d}$ (298 K)	95.3 ± 2.7	...	87.9 ± 2.5
$W_{SL,d}$ (323 K)	90.2 ± 2.5	83.9 ± 2.7	85.0 ± 2.2
$W_{SL,d}$ (348 K)	84.5 ± 3.6	79.0 ± 2.6	81.3 ± 2.1

in the droplet simulations is curved. If the effect of curvature of the liquid-vapor interface can be neglected, Eq. (1) suggests that W_{SL} obtained from droplet simulations and free energy calculations should be equal. We report in Table III the values of W_{SL} (denoted $W_{SL,d}$) obtained from the measured θ_d and γ_L and calculated through Eq. (1). Comparison with the data in Table II shows that the agreement is quantitative for SPC/E and ELBA, although the values of $W_{SL,d}$ for ELBA tend to underestimate the actual free energy results. In the case of mW, the discrepancy between W_{SL} from the droplet and free energy calculations is larger than the estimated statistical uncertainty, suggesting that size effects are stronger in the case of mW than for the other two models. The curvature and size affects are indeed crucial as explained in Ref. 56. Further studies are needed to clarify theses possible effects on nanodroplets modeled with mW.

In summary, the discussion above shows that free energy calculations may be consistent with droplet simulations if size effects are negligible and if the actual value of γ_L for the water model is properly taken into account. This conclusion was already reached from studies on atomistic models.[21,22] The use of CG models does not affect it.

It is interesting to note that, when converted into contact angles, the values of W_{SL} obtained from free energy calculations contain the information confirmed by droplet simulations that θ seems to be temperature independent. Thus, it is expected according to Eq. (1) that the temperature dependence of W_{SL} follows the temperature dependence of γ_L. The fact that SPC/E and ELBA yield the same entropy of adhesion [slope of $W_{SL}(T)$] is explained from the fact that both models have the same slope for the variation of γ_L with T (see Fig. 3 of Ref. 28 and Fig. 4 of Ref. 54, for ELBA and SPC/E, respectively).

V. CONCLUSIONS AND OUTLOOK

The behavior of one atomistic water model (SPC/E) and two coarse-grained single-site water models (ELBA and mW) on nonpolar surfaces is studied through MD simulations. The three models represent three different approaches to modeling the intermolecular interactions in water. While the atomistic model explicitly represents the hydrogen bonds, the short range tetrahedral order in mW is obtained through an explicit three-body potential. This short-range order is not represented at all in ELBA. These models interacted with nonpolar surfaces through Lennard-Jones interaction potentials, which were parametrized against recent experimental measurements of the contact angle of water. All models yield the typical layer structure with oscillations in the spatial distribution of the water number density perpendicular to the substrate. Owing to the explicit constraint of short range tetrahedral order, SPC/E and mW yield similar spatial distributions of the number density and similar populations of the adsorbed layers close to room temperature. In contrast, ELBA tends to increase the number of layers but decreases their population when compared with the other two models. The interfacial thermodynamic behavior of the models, which is quantified through the solid-liquid work of adhesion W_{SL}, is driven by the principles of statistical thermodynamics that are summarized in Sec. III. It is shown that the ability of a given model to pile up a given number of water molecules in the solid-liquid interaction potential controls the solid-liquid energy component of W_{SL}. The solid-liquid entropy component is controlled by the fluctuations in the solid-liquid energy whose origin is found in the liquid density fluctuations in the adsorbed layers. To a first approximation, the difference between the models as far as this entropy component is concerned can be understood through the liquid bulk isothermal compressibility, which quantifies the liquid density fluctuations that induce the solid-liquid energy fluctuations.

In the light of the general mechanisms that control W_{SL} described above, the temperature transferability of properties like mass density and isothermal compressibility as well as surface tension seems to be necessary so that W_{SL} is also transferable over a broad temperature range. In this context, it is interesting to note that despite the fact that SPC/E and ELBA lead to different layer structures, they yield very similar temperature variations of W_{SL}. In contrast, SPC/E and mW (and therefore ELBA and mW) have values for the entropy of adhesion that differ by a factor of about two and show variations of W_{SL} that diverge when temperature increases. The reason most likely resides in the fact that the temperature dependence of properties like mass density and surface tension is not well represented in the studied range.

In the general context of coarse-graining, one may conclude that the CG potentials for solid-liquid systems with consistent thermodynamic properties do not necessarily need to reproduce the interfacial structure of a reference atomistic model. Our study suggests that CG potentials for the solid-liquid interactions should have a width and a shape which resemble reference atomistic systems. Indeed, these two parameters directly affect the average and variance of the solid-liquid interaction energies, which strongly influence W_{SL}. This conclusion remains valid independent of the coarse-graining method employed, i.e., for models with analytical potentials parametrized based on experiments as employed here, or models obtained through top-down approaches like in Refs. 11, 14, and 15. It can be anticipated that this constraint is challenging to meet as models become coarser. Additionally, the choice of the CG model for the liquid-liquid interactions should be driven by the ability of the model to generate excluded volume interaction and density fluctuations in the most relevant way.

SUPPLEMENTARY MATERIAL

See supplementary material for the parameters of the simulation setup for the free energy calculations, the interfacial tensions of the reference interfaces for the CG water models, the interaction potentials $V(x,y)$ and $V_{SL}(z)$ for graphite and CG graphite, the spatial number density for SPC/E on gold, and the fitting function of n_{rcut} depending on λ for SPC/E on MoS_2.

ACKNOWLEDGMENTS

Both authors thank Florian Müller-Plathe for his long-standing support. F.L. thanks Nico van der Vegt for previous collaborations without which this work would not have been

possible and especially for drawing his attention to the concept of energy-entropy compensation discussed in Sec. III. We acknowledge financial support from the German Research Foundation (DFG) through the collaborative research center TRR 146 Multiscale Simulation Methods for Soft Matter Systems. The HPC Center at Technische Universität Darmstadt is gratefully acknowledged for computer time on the Lichtenberg HPC. We also thank the Jülich Supercomputing Center at Forschungszentrum Jülich for computer time on JURECA.

[1]J. Baschnagel, K. Binder, P. Doruker *et al.*, in *Viscoelasticity, Atomistic Models, Statistical Chemistry*, Volume 152 of Advances in Polymer Science, edited by A. Abe (Springer, 2000), p. 41.
[2]T. Murtola, A. Bunker, I. Vattulainen *et al.*, Phys. Chem. Chem. Phys. **11**(12), 1869 (2009).
[3]C. Peter and K. Kremer, Faraday Discuss. **144**, 9 (2010).
[4]E. Brini, E. A. Algaer, P. Ganguly *et al.*, Soft Matter **9**(7), 2108 (2013).
[5]L. Lu, J. F. Dama, and G. A. Voth, J. Chem. Phys. **139**(12), 121906 (2013).
[6]S. Riniker, J. R. Allison, and W. F. van Gunsteren, Phys. Chem. Chem. Phys. **14**(36), 12423 (2012).
[7]W. G. Noid, J. Chem. Phys. **139**(9), 090901 (2013).
[8]S. J. Marrink, H. J. Risselada, S. Yefimov *et al.*, J. Phys. Chem. B **111**(27), 7812 (2007).
[9]N. J. H. Dunn, T. T. Foley, and W. G. Noid, Acc. Chem. Res. **49**(12), 2832 (2016).
[10]D. Reith, M. Putz, and F. Müller-Plathe, J. Comput. Chem. **24**(13), 1624 (2003).
[11]V. R. Ardham, G. Deichmann, N. F. A. van der Vegt *et al.*, J. Chem. Phys. **143**(24), 243135 (2015).
[12]T. T. Foley, M. S. Shell, and W. G. Noid, J. Chem. Phys. **143**(24), 243104 (2015).
[13]A. A. Louis, J. Phys.: Condens. Matter **14**, 9187 (2002).
[14]S. Y. Mashayak and N. R. Aluru, J. Chem. Phys. **137**(21), 214707 (2012).
[15]S. Y. Mashayak and N. R. Aluru, J. Chem. Theory Comput. **8**(5), 1828 (2012).
[16]J. N. Israelachvili, *Intermolecular and Surface Forces*, 2nd ed. (Academic Press, 1991).
[17]M. Kanduč and R. R. Netz, J. Chem. Phys. **146**, 164705 (2017).
[18]S. N. Jamadagni, R. Godawat, and S. Garde, Annu. Rev. Chem. Biomol. Eng. **2**, 147 (2011).
[19]R. Evans and M. C. Stewart, J. Phys.: Condens. Matter **27**(19), 194111 (2015).
[20]F. Leroy and F. Müller-Plathe, Langmuir **31**(30), 8335 (2015).
[21]F. Leroy, S. Y. Liu, and J. G. Zhang, J. Phys. Chem. C **119**(51), 28470 (2015).
[22]F. Leroy, J. Chem. Phys. **145**(16), 164705 (2016).
[23]H. J. C. Berendsen, J. R. Grigera, and T. P. Straatsma, J. Phys. Chem. **91**(24), 6269 (1987).
[24]M. Orsi and J. W. Essex, PLoS ONE **6**(12), e28637 (2011).
[25]V. Molinero and E. B. Moore, J. Phys. Chem. B **113**(13), 4008 (2009).
[26]K. R. Hadley and C. McCabe, Mol. Simul. **38**(8-9), 671 (2012).
[27]W. H. Stockmayer, J. Chem. Phys. **9**, 398 (1941).
[28]M. Orsi, Mol. Phys. **112**(11), 1566 (2014).
[29]B. Song and V. Molinero, J. Chem. Phys. **139**(5), 054511 (2013).
[30]H. Wang, C. Junghans, and K. Kremer, Eur. Phys. J. E **28**(2), 221 (2009).
[31]A. Govind Rajan, V. Sresht, A. A. H. Pádua *et al.*, ACS Nano **10**(10), 9145 (2016).
[32]H. Heinz, R. A. Vaia, B. L. Farmer *et al.*, J. Phys. Chem. C **112**(44), 17281 (2008).
[33]J. G. Kirkwood, J. Chem. Phys. **3**, 300 (1935).
[34]H. A. Yu and M. Karplus, J. Chem. Phys. **89**(4), 2366 (1988).
[35]F. Taherian, V. Marcon, N. F. A. van der Vegt *et al.*, Langmuir **29**(5), 1457 (2013).
[36]E. Gallicchio, M. M. Kubo, and R. M. Levy, J. Phys. Chem. B **104**(26), 6271 (2000).
[37]N. F. A. van der Vegt and W. F. van Gunsteren, J. Phys. Chem. B **108**(3), 1056 (2004).
[38]D. Ben-Amotz, F. O. Raineri, and G. Stell, J. Phys. Chem. B **109**(14), 6866 (2005).
[39]A. Ben-Naim, *Molecular Theory of Water and Aqueous Solutions* (World Scientific, Singapore, 2009).
[40]M. Makaremi, M. S. Jhon, M. S. Mauter *et al.*, J. Phys. Chem. C **120**(21), 11528 (2016).
[41]H.-J. Butt and M. Kappl, *Surface and Interfacial Forces* (Wiley-VCH, Weinheim, 2010).
[42]F. Sedlmeier, J. Janecek, C. Sendner *et al.*, Biointerphases **3**(3), FC23 (2008).
[43]J. R. Errington and P. G. Debenedetti, Nature **409**(6818), 318 (2001).
[44]Q. Liu and B. Xu, AIP Adv. **5**(6), 067150 (2015).
[45]J. Włoch, A. P. Terzyk, P. A. Gauden *et al.*, J. Phys.: Condens. Matter **28**(49), 495002 (2016).
[46]F. Taherian, F. Leroy, and N. F. A. van der Vegt, Langmuir **29**(31), 9807 (2013).
[47]V. Kumar and J. R. Errington, J. Phys. Chem. C **117**(44), 23017 (2013).
[48]F. D. Petke and B. R. Ray, J. Colloid Interface Sci. **31**(2), 216 (1969).
[49]J. Liu, C. Wang, P. Guo, G. Shi, and H. Fang, J. Chem. Phys. **139**(23), 234703 (2013).
[50]R. Evans and N. B. Wilding, Phys. Rev. Lett. **115**(1), 016103 (2015).
[51]C. Weber and H. Stanjek, Colloids Surf., A **441**, 331 (2014).
[52]K. A. Motakabbir and M. Berkowitz, J. Phys. Chem. **94**(21), 8359 (1990).
[53]W. Ding, M. Palaiokostas, and M. Orsi, Mol. Simul. **42**(4), 337 (2016).
[54]C. Vega and E. de Miguel, J. Chem. Phys. **126**(15), 154707 (2007).
[55]N. R. Pallas and Y. Harrison, Colloids Surf. **43**(2-4), 169 (1990).
[56]E. E. Santiso, C. Herdes, and E. A. Muller, Entropy **15**(9), 3734 (2013).

Supplemental material for the manuscript "Thermodynamics of atomistic and coarse-grained models of water on nonpolar surfaces"

Vikram Reddy Ardham and Frédéric Leroy

Eduard-Zintl-Institut für Anorganische und Physikalische Chemie, Technische Universität Darmstadt, Alarich-Weiss-Strasse 8, 64287 Darmstadt, Germany

In this supplementary material, the simulation parameters for the free energy calculations of W_{SL} are given in the Tables S1 and S2. The interfacial tensions between the CG water models on the surfaces for the reference interfaces together with the surface tensions of the CG models are given in Table S3. The interaction potential between water and the whole graphite surface for a water molecule at the distance $z=\sigma_{CW}$ from the surface is shown in Fig. S1 for AT graphite and in Fig. S2 for CG graphite. The *xy*-averaged interaction potential between water and the whole graphite surface depending on the distance from the surface $V_{SL}(z)$ is shown in Fig. S3. The number density distribution of SPC/E perpendicular to the surface on gold is shown in Fig. S4. In Fig. S5, the variation of n_{rcut} with respect to λ is shown.

TABLE S1. Simulation parameters for the calculation of W_{SL} for different surfaces. The number of water molecules is N_L, the number of particles for the surfaces is N_S, the cross sectional area for the solid-liquid contact is $\mathcal{A}$.

Surface	N_L / molecules	N_S / particles	$\mathcal{A}$ / nm^2
MoS_2	7100	1344	4.41×4.368
Graphite	5000	3000	4.26×3.689
Gold	3200	1440	3.466×3.002
CG graphite	5000	1500	4.26×3.689

TABLE S2. Simulation time in nanosecond for the different water models on the different surfaces for the calculation of W_{SL}. The values refer to the length of the production simulations used to calculate the ensemble averages in Eq. (4) of the manuscript. The numbers in parentheses refer to the equilibration time that preceded the production for ensemble averaging.

	SPC/E	ELBA	mW
MoS_2	2(2)	10(2)	10(2)
Graphite	2(2)	10(2)	10(2)
Gold	3(2)	…	…
CG graphite	...	10(2)	10(2)

TABLE S3. Solid-liquid interfacial tension γ_{SL} for CG water models on different surfaces at λ_0=0.001.

	γ_{SL} / mJ/m^2 (model mW)	γ_{SL} / mJ/m^2 (model ELBA)
MoS_2	64.8±1.1	71.5±1.6
Graphite	65.6±1.2	71.7±2.5
CG Graphite	65.3±1.2	72.7±1.7
γ_L / mJ/m^2	63.4±1.2	70.9±0.5

FIG. S1. Interaction potential $V(x,y)$ between a water molecule at the distance $z=\sigma_{CW}$=3.3525 Å from the AT graphite surface and the whole surface. The colored scale on the left is the energy scale in kJ/mol. The yellow spots with the greatest energy correspond to the carbon atoms.

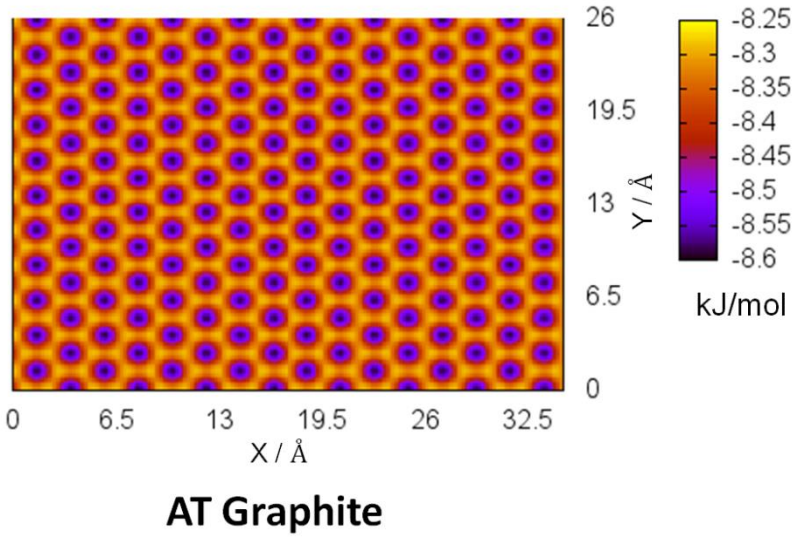

FIG. S2. Interaction potential $V(x,y)$ between a water molecule at the distance $z=\sigma_{CW}$ from the CG graphite surface and the whole surface. The colored scale on the left is the energy scale in kJ/mol. The yellow spots with the greatest energy correspond to the surface particles.

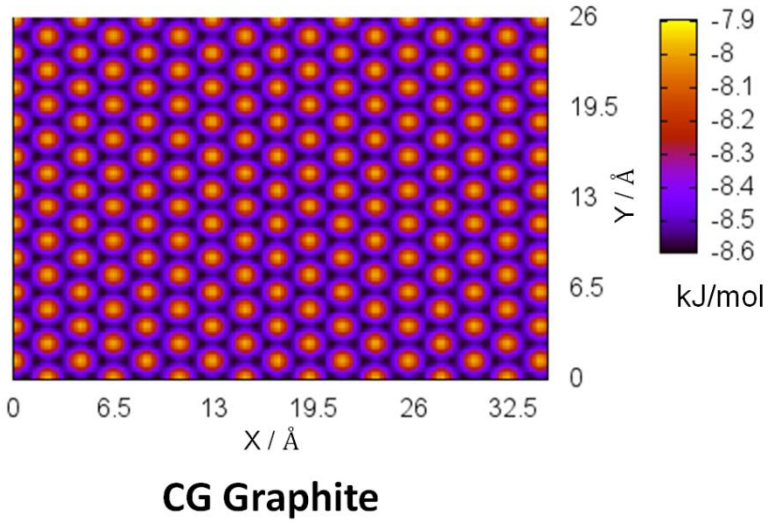

FIG. S3. Interaction potential $V_{SL}(z)$ between a given water molecule at the distance z from the graphite surface and the whole surface. The plots for AT graphite and CG graphite are indistinguishable.

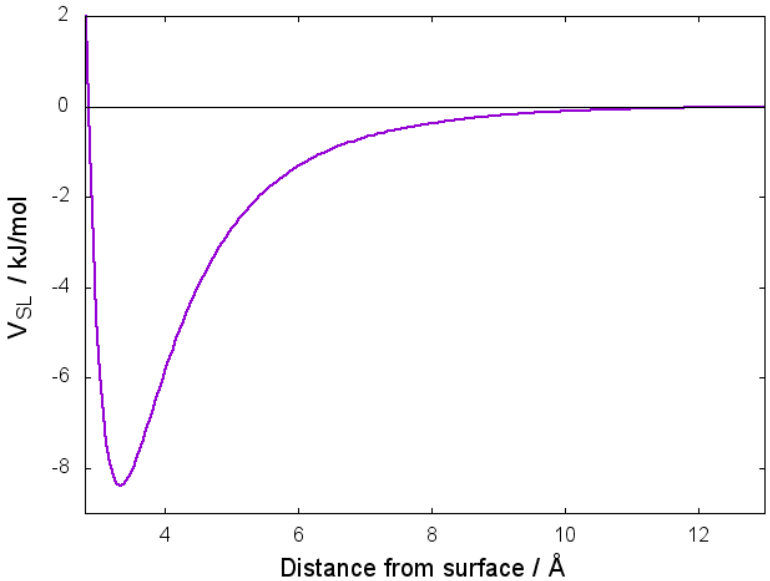

FIG. S4. Spatial distribution of the number density of SPC/E on gold at 323 K.

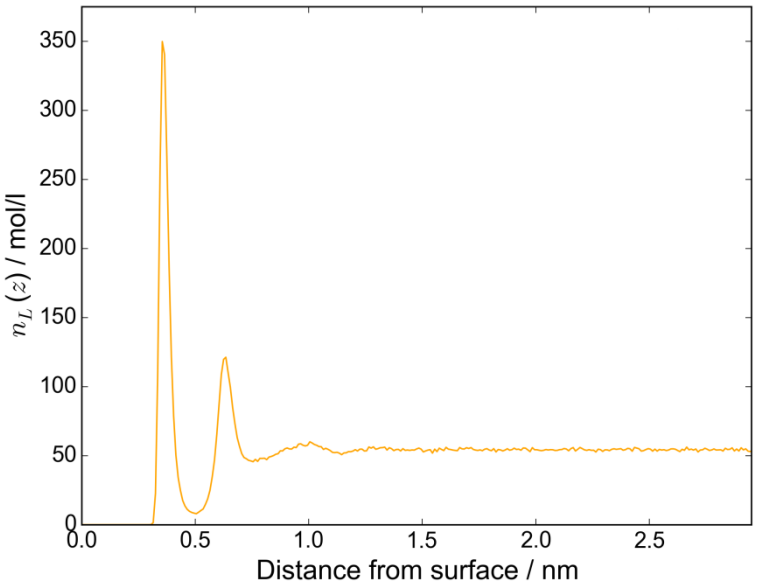

FIG. S5. Variation of n_{rcut} with respect to λ for SPC/E on the basal plane of monolayer MoS_2 at 323 K (black circles) and fitting function $n_{rcut}(\lambda)=a\ \ln\lambda+b$, with a=3.19±0.07 and b=33.8±0.1.

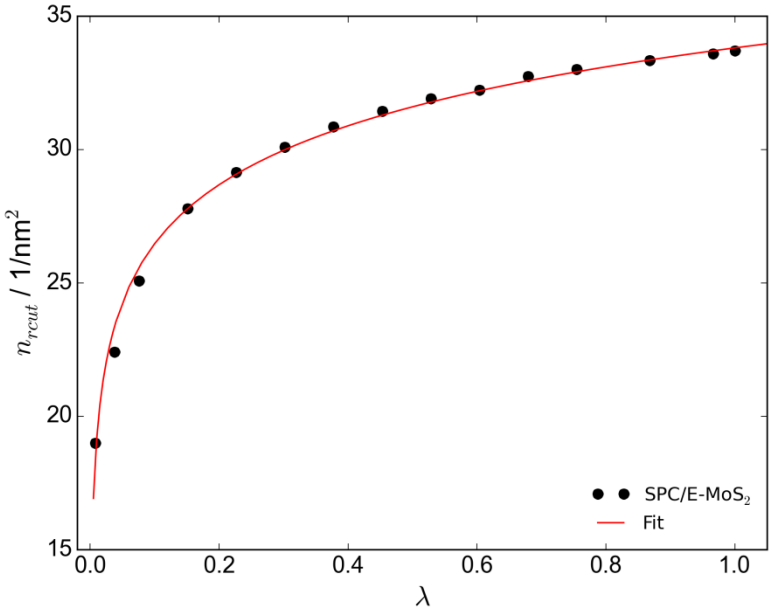

CHAPTER # 4

Atomistic and Coarse-grained Modeling of the Adsorption of Graphene Nanoflakes at the Oil-Water Interface

Vikram Reddy Ardham and Frédéric Leroy*[#]

Technische Universität Darmstadt, Eduard-Zintl-Institut für Anorganische und Physikalische Chemie, Alarich-Weiss-Strasse 8, 64287 Darmstadt, Germany

[#]Present address: Independent scientist, Île-de-France, France

ABSTRACT

The high interfacial tension between two immiscible liquids can provide the necessary driving force for the self-assembly of nanoparticles at the interface. Particularly, the interface between water and oily liquids (hydrocarbon chains) has been exploited to prepare networks of highly interconnected graphene sheets of only a few layers thick that are well suited for industrial applications. Studying such complex systems through particle-based simulations could greatly enhance the understanding of the various driving forces in action and could possibly give more control over the self-assembly process. However, the interaction potentials used in particle-based simulations are typically derived by reproducing bulk properties and are therefore not suitable to describe systems dominated by interfaces. To address this issue, we introduce a methodology to derive solid-liquid interaction potentials that yield an accurate representation of the balance between interfacial interactions at atomistic and coarse-grained resolutions. Our approach is validated through its ability to lead to the adsorption of graphene nanoflakes at the interface between water and *n*-hexane. The development of accurate coarse-grained potentials that our approach enables, will allow us to perform large scale simulations to study the assembly of graphene nanoparticles at the interface between immiscible liquids. Our methodology is illustrated through a simulation of many graphene nanoflakes adsorbing at the interface.

1. INTRODUCTION

Liquid-liquid interfaces offer a rather unique advantage for the adsorption and the self-assembly of nanoparticles. Under appropriate conditions, these nanoparticles spontaneously migrate towards the interface forming networks, patterns with definite orientations or sometimes thin films closely resembling two-dimensional structures. The high interfacial tension between immiscible liquids generates a strong driving force for a solid nanoparticle to settle down at the interface. This observation may be understood in quantitative terms through the balance of interfacial tensions between the different components of a given system. To illustrate our purpose, we consider a system made up of water (denoted *w*), an oily liquid (denoted *o*), and a thick planar solid particle (denoted by *p*), i.e., with thickness much larger than the characteristic length of the intermolecular interactions at hand. The corresponding interfacial tension is denoted by γ with the respective subscripts. In this case, the balance mentioned above is quantified through the wetting coefficient ω following:

$$\omega = \frac{\gamma_{pw} - \gamma_{po}}{\gamma_{wo}} \qquad (1)$$

A nanoparticle located initially in either of the liquid phases, spontaneously moves towards the interface when the condition $|\omega|<1$ is met, as will be shown in section 2. The large value of γ_{wo} obtained between water and oily compounds such as *n*-alkanes ($\gamma_{wo} \approx 50$ mJ/m^2 at room temperature) favors the condition $|\omega|<1$.

The adsorption of graphene particles at the interface between liquids has already been exploited experimentally, to prepare conductive thin films,[131] to obtain oil-in-water Pickering emulsions stabilized by pristine graphene sheets,[54-4] to synthesize large ultra-thin graphene sheets aided by self-assembly[132] and Pickering emulsions of graphene-oxide liquid crystals that are locally aligned,[133] just to name a few. The graphene particle networks formed by interfacial adsorption can be used as a template or as raw-material for several applications. It is worth mentioning here that, most industrial and practical applications require graphene particle networks to be very thin, i.e., only up to a few monolayers thick. Moreover, the use of pristine graphene ensures that enhanced behavior as far as physical properties are concerned is preserved when compared to functionalized graphene. It was also found that percolation of conductive particles in nanofluids or polymer composites provides a channel for enhanced heat and electron transfer.[134-11] It is thus expected that percolation in the two-dimensional liquid-liquid interface arrangement may yield a similar enhancement of transport properties.[12,13] Interested readers may find further examples and a general overview on the topic in refs 14-17 among others.

Studying the assembly of many nanoparticles at the molecular scale in the above systems may help improve our understanding of the underlying physics and enhance composite material design. However, performing particle-based simulations with atomistic resolution is impossible with the current level of computational power. The length and time scales to access all the heterogeneities these systems encompass are simply too large to be accessed with atomistic models. To mitigate this problem, models with a reduced number of degrees of freedom must be employed. Such a reduction is usually accompanied by an accelerated dynamics such that structures can be equilibrated faster than with atomistic models.[18–23] A method that may be used in this context is the dissipative particle dynamics (DPD) method.[24] However, the mesoscale DPD simulations allow only a generic description of the systems where microscopic details at the molecular scale are absent. In the present work, we derive coarse-grained (CG) models, i.e., models with a reduced number of degrees of freedom, which retain the specific chemical composition of a given system described by the parent atomistic (AT) models. We consider systems made up of pristine graphene nanoflakes at the interface between water and *n*-hexane as a prototype of water-oil interface. Note that similar systems have been studied by molecular simulation on atomistic systems and experimentally by the groups of Adamson and Dobrynin.[1,54]

As discussed above, the balance of interactions among various species determines whether the condition $|\omega|<1$ for the spontaneous migration of nanoparticles towards the liquid-liquid interface is fulfilled. Because liquid models are generally not optimized to model interfaces, it cannot be expected that the simple mixing of interaction parameters following usual mixing rules between AT models for liquids and particles yields values for the interfacial tensions such that $|\omega|<1$.[141] As for CG models, coarse-graining generally goes along with a modification of the thermodynamic properties of a reference atomistic model.[142–145] Therefore, CG models which are developed based on atomistic models do not necessarily reproduce the balance of interfacial tensions in the parent atomistic model.

In the present work, we develop a general methodology to generate AT and CG models for the liquid-particle interactions which yield controlled values of the wetting coefficient ω. The interfacial tension between a given solid and a given liquid is generally not measurable. Thus, we reformulate the definition of ω (eq 1) in terms of quantities that can be calculated with simulations and accessed through experiments (section 2). We show in section 3 one way to derive models or modify existing ones to obtain a given value of ω. In section 4.1, we address the question as to whether models for which $|\omega|<1$ lead to stable adsorption of graphene nanoflakes at the water-*n*-hexane interface. Further an illustration of the usefulness of the derived CG potentials is shown by simulating a system with

several graphene particles adsorbing at the interface in section 4.2. The conclusions are summarized in section 5.

2. THEORETICAL BACKGROUND AND CHALLENGES

In this section, the condition $|\omega|<1$ for the adsorption of a planar particle at the liquid-liquid interface is derived. Based on experiments, we show that the adsorption of graphene particles at the water-*n*-heptane interface observed in ref 1 is likely to correspond to $\omega\approx1$. We then discuss in general terms the difficulties that arise while relating ω to interaction potentials and conclude the section by proposing an approach to overcome these difficulties for AT and CG models.

To derive eq 1, a thick planar nanoparticle initially located in water is considered and boundary effects arising from the particle are ignored. When the nanoparticle is relocated to the interface between water and oil, work is required to replace half the total area of the interface between the nanoparticle and water with an interface of the same area between the nanoparticle and oil (see Figure S1 of SI), in addition to removing the existing liquid-liquid interface with the same area. The Helmholtz free energy change $\Delta F_{w\to i}$ per unit area (i denotes the interface) of this process is thus:

$$\frac{\Delta F_{w\to i}}{A} = -\gamma_{pw} - \gamma_{wo} + \gamma_{po} \qquad (2)$$

Similarly, $\Delta F_{o\to i}$ (relocation from oil phase to the interface) can be obtained as well and for a nanoparticle initially located in either of the liquids to be relocated to the liquid-liquid interface, the combined conditions $\Delta F_{w\to i}<0$ and $\Delta F_{o\to i}<0$ lead to $|\gamma_{pw}-\gamma_{po}|/\gamma_{wo}=|\omega|<1$. Note that the Helmholtz free energy was used because the pressure-volume (PV) term is usually negligible in liquid phases at ambient conditions.

In the derivation above, it is assumed that the thickness of the nanoparticle is large enough for the liquid molecules on both sides to not interact with each other. This assumption becomes questionable when a nanoparticle has the thickness of a graphene monolayer. When a graphene layer initially solvated in water moves to adsorb at the liquid-liquid interface, the intermolecular interactions between the water molecules through graphene are replaced with interactions between water and the alkane through graphene. Therefore, not only changes in solid-liquid interactions but also changes in liquid-liquid interactions occur. A closely related question was addressed by Driskill *et al.*[146] These authors calculated the adhesion free energy of water on graphene, and the work of adhesion of water on graphene with liquid water adsorbed below the graphene layer. They found a difference of 8 mJ/m^2, which is about 8-10% of the adhesion free energy. Note however that the present situation where a liquid (e.g. water) on one side of graphene replaces another liquid (e.g. an alkane) is different. In fact, when a graphene layer is relocated from water (or alkane) to the alkane-water interface, water-water

(or alkane-alkane) interactions through graphene are replaced with water-alkane interactions. Therefore, one expects the free energy contribution arising from the change of liquids to be less than 8 mJ/m^2 mentioned above and about one order of magnitude less than the interfacial tension γ_{wo}. It can thus be argued that, although the relationship $|\omega|<1$ was obtained for thick particles it can still be used as a reference criterion for studying the adsorption of particles with atomic thickness.

We now discuss the challenges that must be taken up to obtain a given value of ω in molecular simulations of graphene particles at the water-alkane interface. This is illustrated here based on experimental data for the interaction between water, *n*-heptane and graphite. From the experimental work of Fowkes,[147] it is found that $(\gamma_{pw}-\gamma_{po})/\gamma_{wo}\approx0.96$, i.e., ω is close to 1 (section S1 of SI). It can reasonably be assumed that the interaction between water and graphite and even more so between *n*-heptane and graphite is short-ranged. This assumption is confirmed by the fact that monolayer and few layer graphene have virtually the same interfacial tension (see section S1 in SI).[32] Thus, the difference, $\gamma_{pw}-\gamma_{po}$ for a graphene monolayer should be close to what it is for graphite. Based on eq 1, it can be concluded that the fact that graphene adsorbs at the water-*n*-heptane interface as observed experimentally[1] arises from a subtle balance of intermolecular interactions that leads to $\omega\approx1$. The challenge for particle-based simulations is therefore to be able to reproduce this precise balance.

The quantity $(\gamma_{pw}-\gamma_{po})/\gamma_{wo}$ depends on γ_{pw} and γ_{po}, which are not directly measurable. In the case of solid-liquid systems in the partial wetting regime with contact angle values above 60°-70° like water on graphite, one may obtain the water-surface interfacial tension γ_{pw} relative to the substrate surface tension γ_p from the independent measurements of the equilibrium contact angle θ_w and of the water surface tension γ_w through Young equation,[33] $\gamma_{pw}-\gamma_p=-\gamma_w cos\theta_w$. A similar approach may be used in molecular simulations of nanometer sized droplets to obtain the interaction potentials that are consistent with the measurement of θ_w, although very specific conditions have to be met.[34,35] A limitation of the approach of measuring contact angles is that vapor surface pressure may play a significant role[31,36,37] and size effects may require system sizes that are prohibitively large.[35,38] Moreover, certain systems are fully wetting (like alkanes on graphite) i.e., contact angles are zero and no information can be obtained by simulating droplets.

In order to overcome the limitations discussed above, we reformulate ω using the solid-liquid work of adhesion W_{pw} for the graphene-water interface, and the solid-liquid work of adhesion W_{po} for the graphene-alkane interface. Note that we assume here that the solid-liquid work of adhesion of a given liquid on a nanoparticle is equal to the solid-liquid work of adhesion on a surface with macroscopic size parallel to the surface. The solid-liquid work of adhesion is defined as the free energy change per unit area required to bring an infinite separation between liquid and solid that are initially in contact.

This operation carried out in vacuum, for the solid-water interface gives, $W_{pw}=\gamma_p+\gamma_w-\gamma_{pw}$. The definition of W_{po} is obtained by substituting the subscript w with the subscript o. Starting from eq 1, the definitions of W_{pw} and W_{po} lead to the following expression for ω:

$$\omega = \frac{(\gamma_w - \gamma_o) - (W_{pw} - W_{po})}{\gamma_{wo}} \quad (3)$$

The advantage of eq 3 is that it depends on quantities that can be calculated through molecular simulations, both with AT and CG models. Indeed, γ_w, γ_o and γ_{wo} can routinely be obtained from various methods which are reviewed for example in ref 39. As for W_{pw} and W_{po}, several methods have been derived in the recent years based on thermodynamic integration[40-42] as shown in section 3 or other enhanced sampling techniques and indirect methods.[43,44] It is important to note that most models for liquids including water and alkanes are not optimized to reproduce experimental interfacial properties like interfacial tension in the first place (see ref 45 for the example of water). Similarly, straightforward combination of force-field parameters between models for solid-liquid interface is generally not expected to yield interfacial thermodynamic properties like interfacial tensions or works of adhesion that compare to experiments in quantitative terms.[34,45] Hence, the challenge with molecular simulations is to derive models for the solid-liquid interactions (quantified through W_{pw} and W_{po} in eq 3) which compensate the differences with the experimental values for γ_w, γ_o *or* γ_{wo} by the liquid models in order to obtain a given ω. In our approach, the values for γ_w, γ_o or γ_{wo} were taken as given by the liquid models while graphene-liquid interactions were adjusted to obtain a given value of ω. This approach is presented in section 3.3.

Finally, it can be noted that the condition $|\omega|<1$ discussed above to observe the spontaneous adsorption of thin planar particles at the liquid-liquid interface has already received confirmation from experiments. Indeed, graphene adsorption was observed at the water-cyclohexane[46] and at the water-1,2-dichlorobenzene[47] (1,2-DCB) interfaces. Graphene oxide adsorption at the interfaces between water and several fluids like benzene,[48] toluene,[49,50] chloroform,[49] methyl methacrylate (MMA)[4] was observed, too. Other thin two-dimensional materials such as MoS_2 and WS_2 were found to adsorb at the interface between water and 1,2-DCB. In all the cases, we found that the condition $\omega<1$ was met (see table S1 and section SIII of the SI for the details on the calculation of ω). These experimental observations therefore strongly support our approach based on the condition $|\omega|<1$ to derive models for the adsorption of planar nanoparticles at the liquid-liquid interface. Moreover, the particular values of ω obtained enable one to compare the different organic liquids as far as adsorption at the interface with water is concerned. For example, it is expected that 1,2-DCB is more suitable than cyclohexane to stabilize graphene at the interface, whereas toluene, hexane or MMA (all with $\omega\approx0$) stabilize

graphene oxide at the interface with water better than benzene. The condition $|\omega|<1$ can thus be used to assess the ability of two liquids to yield interfacial adsorption, provided that the quantities that define ω in eq 3 are known.

3. MODELING APPROACH

Classical molecular dynamics simulations were performed using the open-source simulation package LAMMPS,[51] developed and managed at the Sandia National Laboratories. The equations of motion were integrated using the Verlet algorithm. Both AT and CG models were employed to model the liquids whereas the graphene sheet was always represented with full atomistic details. As a prototype of oily phase, *n*-hexane was chosen to form the liquid-liquid interface with water. All simulations were performed at 323 K, i.e., well above the melting point of the CG water model presented below. The technicalities of the calculations of the interfacial quantities discussed in section 3.1 and 3.2 are detailed in section 3.4. Information on the system sizes for different calculations is given in Tables S1-S3 (SI).

3.1 Models for pure components

At the AT level, *n*-hexane was represented using a united atom model with the NERD[52] force-field with a cutoff radius of 1.4 nm. No long-range corrections were used for pressure or energy. This model yields γ_o=11.2±0.4 mJ/m^2, which underestimates the experimental value (15.43 mJ/m^2 at 323 K[53]). Atomistic water was modeled with the SPC/E[54] model. The long-range dispersion and Coulomb corrections were applied using a variation of the particle-particle-particle-mesh algorithm explicitly developed for heterogeneous interfaces.[55] Interactions in the real space for water were truncated at 1 nm. The accuracy of calculations in the k-space was set to the order of 10^{-5} for forces and energies in SI units. That model of water yields γ_w=60.1±1.2 mJ/m^2. At the CG level, water was simulated using the recently developed finite-sized spherical particle-dipole ELBA[56] model, which leads to γ_w=71.2±0.8 mJ/m^2, in good agreement with the experimental value (67.9 mJ/m^2 at 323 K). The model ELBA is a single-water model, i.e., a water CG bead represents a single water molecule. The CG interactions for *n*-hexane were derived using the conditional reversible work (CRW) method.[57] More details about this approach are given in our recent work.[41] A three-bead representation was used for *n*-hexane, as shown in Figure S2 (SI). There are two types of beads in this model: one bead (A type) for the terminal CH_3-CH_2 groups of atoms and another bead (B type) for the center CH_2-CH_2 group (Figure S2). Note that in our previous study on CG *n*-hexane the all-atom model with the OPLS force-field[58] was employed instead of the NERD model. The present CG *n*-hexane model yields γ_o=16.2±0.6 mJ/m^2.

The graphene particles were modeled using the standard AIREBO[59] potential. For the purpose of developing our approach, these graphene particles have no edge hydrogen termination and therefore only contain carbon atoms. It can be noted that the graphene particles are fully flexible and that their instantaneous shape deviates from the strictly planar geometry assumed in the derivation of eq 3 for the definition of ω. We observed that these fluctuations are weak in magnitude and neglected them in our analysis. The graphene particle used in the simulations contained 294 carbon atoms. It is hexagonal in shape with an area of 8.4 nm^2.

3.2 Models for the liquid-liquid interfaces

In the AT simulations, water and *n*-hexane interacted through Lennard-Jones pair potentials. The corresponding distance and energy parameters were obtained using the Lorentz-Berthelot mixing rules. These interactions were truncated at 1.4 nm with no long-range corrections. This model leads to the value for the water-*n*-hexane interfacial tension γ_{wo}=51.4±1.8 mJ/m2, which compares well with the experimental value[60] (49.25 mJ/m^2 when linearly extrapolated to 323K).

The derivation of the water-*n*-hexane CG pair potentials was performed in two steps. Firstly, simulations with the AT models were performed to obtain these potentials using the thermodynamic perturbation variant of the CRW method.[57] The potentials thus obtained were found to give a value of γ_{wo} larger than the AT value given above, indicating that the CG potentials directly obtained from the CRW calculations were too repulsive. Thus, a second step followed in which the potentials were tuned to increase the magnitude of the corresponding interactions. This was implemented by multiplying the CRW potentials directly obtained with a mono-exponential function of the interparticle distance following:

$$u_{CRW}\left(r_{ij}\right) = u^{0}_{CRW}\left(r_{ij}\right)\exp\left(-\alpha r_{ij}\right) \tag{4}$$

In eq 4, u_{CRW} is the pair potential obtained after the second step acting between a given CG water molecule (*i*-th CG site) and either sites of CG *n*-hexane (*j*-th CG site) at a distance r_{ij} apart. The quantity u^0_{CRW} is the CG potential directly arising from the CRW calculations (first step). The quantity α is a scaling parameter, which when set to -0.4 nm^{-1} yields γ_{wo}=49.2±1.0 mJ/m^2, in agreement with the experimental and AT values. This value of -0.4 nm^{-1} was obtained by computing γ_{wo} depending on α, as shown in Figure S3 (SI). The role of the exponential function in eq 4 is to preserve the repulsive part of the original pair potential, while it scales the potential well and the attractive tail without modifying the monotonic variation.[41] Both the potentials u^0_{CRW} and u_{CRW} at α=-0.4 for the *n*-hexane-water interaction are shown in Figure S4 (SI).

At this point, it is interesting to observe that the contribution $(\gamma_w-\gamma_o)/\gamma_{wo}$ to ω is close to 1. More precisely, that quantity is 1.09 for the experimental system, 0.95±0.06 for the AT model and 1.12±0.05

for the CG model. It is thus expected according to eq 3, that $\omega \approx 1$ is obtained when the ratio $(W_{po}-W_{pw})/\gamma_{wo}$ is negligible, i.e., when the force-field parameters are adjusted to obtain $W_{po} \approx W_{pw}$.

3.3 Models for the solid-liquid interfaces

The interaction between graphene and the liquids was modeled with different potentials depending on the resolution of the models. For the AT simulations, water and *n*-hexane interacted with graphene through Lennard-Jones pair potentials. For the CG simulations, the water bead interacted with graphene also through the Lennard-Jones pair potential similarly to our previous work.[61] Only for the interaction between CG *n*-hexane and graphene a non-analytical tabulated potential was used. As already mentioned, in both the AT and CG simulations graphene was modeled at the atomistic resolution, i.e., with all the carbon atoms represented.

As discussed at the end of section 2, the models for the liquids may fail to reproduce the experimental values for surface tension. In the present case, it was discussed at the end of section 3.2 that the AT and CG liquid models yield values for the ratio $(\gamma_w-\gamma_o)/\gamma_{wo}$ that are in good agreement with experiments. Therefore, the interaction potentials between the liquids and graphene have to be constructed in such a way that they yield values for the work of adhesion that can easily be adjusted to obtain a given ω. Such a constraint was dealt with by adjusting the depth of the well of the graphene-liquid interaction pair potentials. In concrete terms, the solid-liquid work of adhesion was made dependent on a parameter that controls the depth of the potentials wells. We discuss below how this approach was implemented in simulations with AT and CG potentials, although it has already been illustrated in previous works by us with others.[41]

For the AT systems which interact through the 12-6 Lennard-Jones pair potential, the depth of the water-carbon and of the CH_2-carbon and CH_3-carbon pair potentials was adjusted through the energy parameter for the carbon atoms of graphene ε_C. Following the dry-surface approach,[40] the solid-liquid work of adhesion between a carbon surface and a given liquid, here denoted by liquid 1, is obtained from:

$$W_{p1}(\varepsilon_C) = -\frac{1}{A}\int_{\sqrt{\varepsilon_0}}^{\sqrt{\varepsilon_C}} \left\langle \sum_{i=1}^{N_L}\sum_{j=1}^{N_C} \varepsilon_i \left(\frac{\sigma_{ij}^{12}}{r_{ij}^{12}} - \frac{\sigma_{ij}^{6}}{r_{ij}^{6}} \right) \right\rangle d\sqrt{\varepsilon} \qquad (5)$$

In eq 5, N_L is the number of atoms in the liquid. For water, N_L is the number of water molecules, for hexane it is the total number of CH_3 and CH_2 united atoms. The quantity N_C is the number of carbon atoms on a given graphene surface. The quantity ε_i is the Lennard-Jones energy parameter for the *i*-th liquid atom, and σ_{ij} is the distance parameter for the interaction between the *i*-th liquid atom and the *j*-th solid atom. Finally, ε_0 is a reference value for the energy parameter of the carbon atoms that defines

a reference state. It was chosen such that the average total solid-liquid interaction energy is of the order of -0.01 mJ/m^2, as prescribed in the dry-surface approach.[40] The variation of W_{po} and W_{pw} depending on ε_C for the atomistic systems on graphene is given in Figures S5 and S6 (SI), respectively.

The interaction between graphene and the CG water bead was also modeled through the Lennard-Jones potential whose distance and energy parameters are σ_{CW} and ε_{CW}, respectively. The solid-liquid work of adhesion between water and graphene depends on ε_{CW} following:[41]

$$W_{pw}(\varepsilon_{CW}) = -\frac{1}{A}\int_{\varepsilon_{CW,0}}^{\varepsilon_{CW}} \left\langle \sum_{i=1}^{N_W}\sum_{j=1}^{N_C}\left(\frac{\sigma_{CW}^{12}}{r_{ij}^{12}} - \frac{\sigma_{CW}^{6}}{r_{ij}^{6}}\right)\right\rangle d\varepsilon \tag{6}$$

where N_W is the total number of CG water beads, $\varepsilon_{CW,0}$ is the carbon-water energy parameter that defines the reference state for the CG water-graphene system. The value $\varepsilon_{CW,0}$=0.0031 kJ/mol was employed. This value is small enough to render graphene-water interactions negligible and therefore provides a reference state as detailed in our earlier work.[41] The variation of W_{pw} for ELBA on graphene is given in Figure S7 (SI).

The solid-liquid work of adhesion W_{po} between CG *n*-hexane and graphene was made dependent on a parameter α as prescribed in ref 41, such that:

$$W_{po}(\alpha) = -\frac{1}{A}\int_{\alpha_0}^{\alpha} \left\langle \sum_{i=1}^{N_L}\sum_{j=1}^{N_C} - r_{ij}u_{SL,j}^{0}(r_{ij})\exp(-\alpha' r_{ij})\right\rangle d\alpha' \tag{7}$$

where $u^0_{SL,j}$ is the CG pair interaction potential between either of the *n*-hexane CG beads and the carbon atoms of graphene, and α_0=10 nm^{-1} defines the reference state for the system. Similar to the CG potential for the water-*n*-hexane interaction, the CRW method was employed to obtain u^0_{SL}. In the corresponding reference atomistic model, the simulations were performed on graphite modeled with four carbon layers. The energy parameter ε_C for the graphite carbon atoms was set to 0.3123 kJ/mol, so that the solid-liquid work of adhesion of *n*-hexane on graphite is 115 mJ/m^2. The experimental value for this system can only be approximated due to the scattered experimental data.[31] Therefore, it was chosen to reproduce the value previously calculated by us with the all-atom OPLS force-field which yields 115 mJ/m^2.[41] This value is consistent with experimental results. The CG pair potentials $u^0_{SL,j}$ on graphite were employed without modification on graphene. The variation of $W_{po}(\alpha)$ is shown in Figure S8 (SI).

3.4 Simulation Details

The various initial configurations were generated using PACKMOL.[62] To evaluate the liquid-vapor surface tension, the system was first equilibrated at constant number of particles, constant temperature and constant pressure (1 atm) (*NPT*) for 1 ns and then stretched perpendicular to the interface to thrice

its size. A subsequent simulation at constant volume and constant temperature *(NVT*) was performed. For the liquid-liquid interfacial tensions, the same first step as above was performed and *NVT* simulations were performed at the volume obtained in the first step. The interfacial tensions were evaluated using the mechanical route given by the pressure anisotropy equation[45] while collecting the data over at least 50 ns. The system sizes for these calculations are reported in Table S2 (SI).

For the adsorption-desorption simulations with graphene particles at the interface discussed in section 4, immiscible layers of water and hexane were equilibrated giving rise to two water-oil interfaces as illustrated in Figure S9 (SI). Then a graphene particle interacting only through soft-core interactions (with finite interaction at zero separation) was introduced into the system. The system was equilibrated for one picosecond to move aside the liquid molecules that were too close to graphene. Despite this action, in some cases a few molecules remained connected through graphene. These molecules were deleted from the system forcefully. Finally, the interactions between graphene particle and liquid were switched to the normal hard-core interactions based on the model being used before equilibrating further. All the simulations with the graphene particles were performed under *NVT* conditions after the *NPT* equilibration at T=323 K and pressure P=1 atm of the liquid-liquid interface. Simulations were performed with a single graphene particle with hexagonal shape. For the AT systems, Nosé-Hoover thermostat and barostat were used, with time constants 0.05 ps and 2 ps, respectively. In the CG systems where ELBA water is present, Langevin thermostat and Berendsen barostat were used with the time constants equal to 0.1 ps and 4 ps respectively. The equations of motion were integrated with a time step of 0.5 fs in all cases. A smaller timestep was used for equilibrating random initial configurations. Such short timestep values combined with the use of computationally expensive long-range electrostatics in the AT simulations represent a drastic limitation on such high-resolution simulations. Simulations with the Umbrella sampling method[63] in the *NVT* ensemble were used to compute the potential of mean force (PMF) on the graphene particle. A spring was attached to the graphene particle's center of mass with a force constant of 52300 kJ/mol/nm^2. Water's center of mass was also tethered to a spring (with a spring constant six times the above value) to maintain the interface stationary. Several windows were utilized by fixing the graphene particle's z-coordinate in space at various locations close to the interface. A window separation of 0.02 nm was chosen and at each window, the system was equilibrated for 100 ps and statistics were collected for 500 ps. The trajectories obtained for each window were combined using the Umbrella integration method[64] to finally compute the PMFs. More details about the calculations are provided in the SI (section SVIII).

4 RESULTS & DISCUSSION

4.1 Single graphene particle at the oil-water interface

It can be noted that *n*-hexane and *n*-heptane have surface tension values that differ only by 2 mJ/m^2 and interfacial tensions with water differ by 0.5 mJ/m^2. Thus, it is straightforward to show (see SI) that the value $\omega \approx 1$ for graphene at the *n*-heptane-water interface inferred from experiments in section 2 is also applicable for the *n*-hexane-water interface. We show below through PMF calculations that both AT and CG simulations performed around $\omega=1$ with interaction potentials developed as indicated in section 3 also yield graphene adsorption at the water-*n*-hexane interface. We performed additional simulations to find out what other values of ω also yield adsorption at the interface and tested whether the transition from adsorption to desorption is in accord with the PMF calculations and the condition $|\omega|<1$.

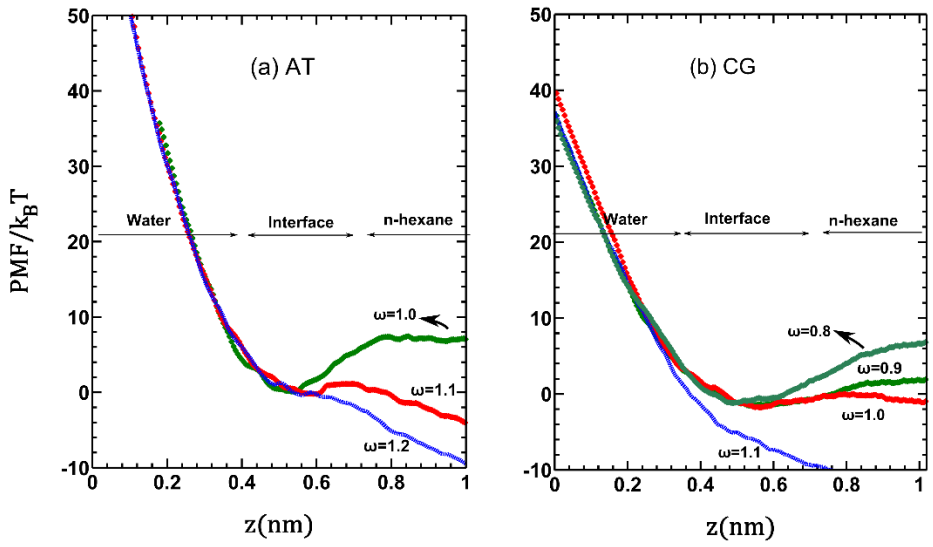

Figure 1. PMF profiles for systems (a) AT and (b) CG illustrating the value of ω at which the transition from adsorption to desorption takes place. Curves that possess a clear minimum at the interface support adsorption at the interface ($\omega=1.0$ for the AT system and $\omega=0.8$ and 0.9 for the CG system) whereas curves that lack a global minimum ($\omega=1.1$ and 1.2 for the AT system and $\omega=1.0$ and 1.1 for the CG system) result in graphene particle migration to the bulk-oil phase. The coordinate (z) perpendicular to the interface is shifted for clarity. k_BT is the thermal energy.

To perform simulations around $\omega=1$, γ_o, γ_w and γ_{wo} were taken as given by the models (section 3) while values for W_{pw} and W_{po} and the related force-field parameters were tuned. In this context, it can be noted that W_{pw} is relatively well known owing to the considerable experimental work that has been performed to characterize the wetting behavior of highly-ordered pyrolitic graphite.[65] Recent experiments suggest that $\theta=64°$ for water on graphite.[66] It can also be assumed that the temperature change between 298 K at which the measurements were carried out and 323 K which is the temperature of our simulations, did not affect θ.[61] Combined with the experimental value for the surface tension of water at 323 K $\gamma_W=67.9$ mJ/m^2, this contact angle leads to $W_{pw}=97.7$ mJ/m^2 for the work of adhesion

of water on graphite. The simulation parameters ε_C for atomistic water and ε_{CW} for CG water introduced in section 3.3 were tuned to reproduce this value. The parameters obtained lead to W_{pw}=84.2 mJ/m^2 for the AT system and W_{pw}=87 mJ/m^2 for the CG system on a graphene monolayer. Finally, W_{po} was tuned to obtain different values of ω around 1. The corresponding parameters used can be seen in Table S4 (SI).

The PMF calculations were performed for the AT and CG systems using the Umbrella sampling simulations. The plots in Figures 1a and 1b show the variation of the PMF relative to the thermal energy as the graphene particle changes its location perpendicular to the interface, at different values of ω. For the AT system shown in Figure 1a, when ω becomes ≥1.1, the minimum in the free energy profile that was present at ω=1.0, disappears. Note that the depth of the corresponding well at ω=1.0 is around 8 k_BT. Accordingly, at ω=1.1 and beyond, the graphene particle is expected to preferentially stay in the *n*-hexane phase. This observation is consistent with the fact that when ω is increased from 1 to 1.1, graphene is made more soluble in *n*-hexane by increasing the interaction between these compounds. Further, it is worth noting that the free-energy profiles with a minimum for the AT system are very similar to the profiles obtained in ref [54], where similar systems were studied. In Figure 1b, we plot the variation of PMF/k_BT, as ω changes from 0.8 to 1.1 to illustrate the transition of the free energy landscape for the CG system. As ω increases, one can clearly see the transformation of the curve with a strong minimum at the interface to its complete absence. In this case, the boundary for interfacial adsorption was found at ω=0.9. At ω=1.0 and beyond, the minimum either becomes a local minimum or completely disappears. However, at ω=0.9 the well depth is rather shallow (≈2-3 k_BT), when compared to ω=0.8, where the well depth is about 7-8 k_BT. Therefore, in this case, ω=0.8 might be a better choice for performing large scale simulations. In can be concluded that, ω values 1.0 and 0.9 mark a transition in the free energy landscape for the AT and CG systems respectively. As ω exceeds these critical values, the graphene particle becomes stabilized in the *n*-hexane phase and fails to adsorb at the interface. It should be mentioned that the values of ω are given with a statistical uncertainty of at least about 10%, i.e., ±0.1 (Table S5 of SI) arising from uncertainties in various quantities in eq 3.

The PMFs confirm that the estimate ω≈1 obtained under the assumption of a thick graphitic particle can be applied to monolayers of graphene as well. These calculations also validate our approach for the derivation of the AT and CG potentials. There are a few reasons which explain why the condition ω≈1 applies to obtain interfacial adsorption of graphene particles while it was primarily derived for thick particles. It can be noted from eq 3 that ω was defined from differences between several quantities. Thus, there may be cancellation of errors that contribute to make the condition apply to graphene adsorption. More importantly, the short-range nature of the interactions at hand plays an important role. We found that when a graphene particle is surrounded by liquid molecules on both the

sides, the corresponding liquid-liquid interactions are negligibly small compared with the solid-liquid interactions. For example, the water-*n*-hexane interaction energy through graphene amounts to less than 2% of the total solid-liquid interaction energy. Therefore, when the graphene particle changes its location from either phase to the interface or conversely from the interface to the oil or water phase, the dominant change in energy arises from the solid-liquid interaction as if the particle were infinitely thick, i.e., as assumed in the derivation of $|\omega|<1$. Furthermore, it should be noted that changes in the liquid-liquid interactions when one liquid replaces the other on a side of the graphene particle amounts to less than the upper boundary of 8 mJ/m^2 obtained by Driskill *et al.* (see section 2). Such a value is equivalent to ≈0.1 in terms of ω, i.e., it is equivalent to the statistical uncertainty in ω.

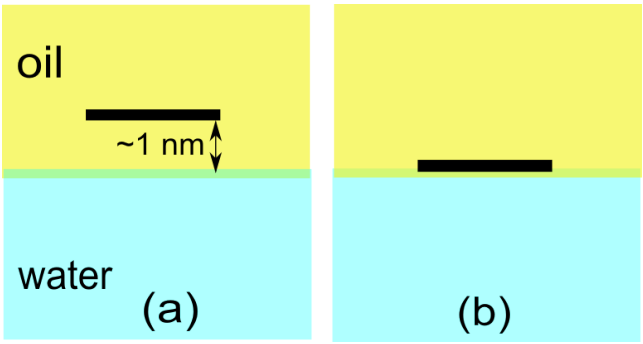

Figure 2. Schematic representations of initial location used to study the adsorption of a graphene particle at the water-*n*-hexane interface: a) graphene particle in *n*-hexane, b) at the interface.

To test the generality of the criterion $|\omega|<1$, for nanoparticle adsorption and to validate qualitatively the results of the PMF calculations additional simulations were performed. Simulations at various ω were performed and the adsorption behavior of a graphene particle was scrutinized through protocols detailed below. The quantities W_{po} and W_{pw} were changed through the corresponding force-field parameters ε_C, ε_{CW} and α, while γ_o, γ_w and γ_{wo} were taken as given by the models. In the first set of simulations denoted by stage A, several randomly chosen values of ω in the range [-1.8: 2.0] were sampled. In most cases, W_{pw} was set to 84.2 mJ/m^2 for the AT system, W_{pw} was set to 87.0 mJ/m^2 for the CG system while W_{po} was varied to tune ω. To obtain the most negative values of ω, W_{pw} had to be increased in addition to the use of extremely low values of W_{po} as can be seen in Table S5 (SI). Indeed, $\omega<0$ (although unrealistic) corresponds to an increased solubility of graphene in water and thus enhanced water-graphene interaction combined with poor *n*-hexane-graphene interaction. At each value of ω between -1.8 and 2.0, the initial location of the graphene particle was chosen either within 0.3 nm from the interface or in either of the bulk phases at around 1 nm from the interface as shown in Figure 2. Note that, in both these cases the separation distance between the graphene particle and the interface was less than the cutoff distance used for the dispersion interactions. It should also be noted that, this distance is rather approximate as the interface cannot be defined sharply. The central

idea was to insert the particle in two different locations, one close to the minimum in the free-energy profile (if it exists) and the other, reasonably far away from it. The solid-particle interactions were set to soft-core potentials when the graphene particle was initially inserted and later switched to the usual LJ interactions, as discussed in section 3.4. In the second set of simulations denoted by stage B, an equilibrated structure with graphene particle at the interface was chosen as a starting point and the solid-liquid interactions were instantaneously switched to obtain new values of ω. A range of values for ω was scanned until a value that marks transition from adsorption to desorption was identified. The complete list of parameters used in each stage is summarized in Table S5 of the SI. The results obtained for stages A and B are summarized in Figure 3 where each colored square refers to a given value of ω in Table S5.

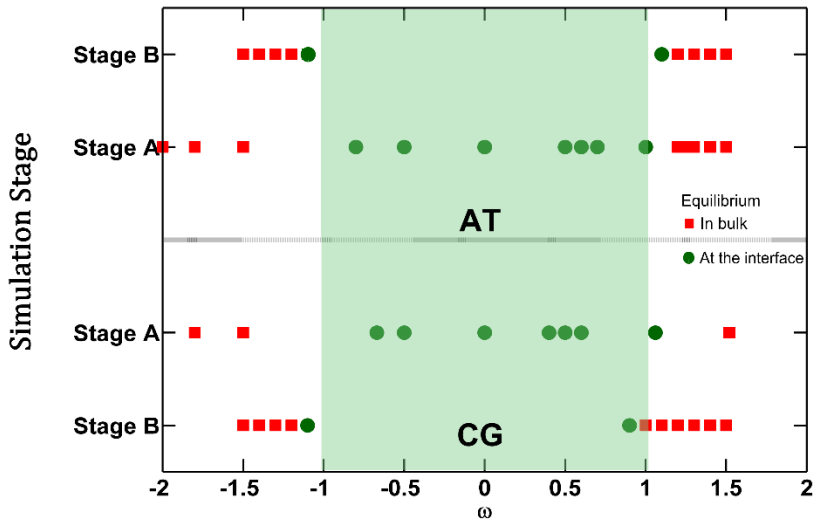

Figure 3. Summary of the results that describe the location of the graphene particle at the end of stage A (graphene particle initially close to the interface or in the bulk of either phases) and stage B (graphene particle initially at the interface) depending on the wetting coefficient ω. The green circle indicates that the graphene particle finally adsorbs at the interface. The red square indicates that the graphene particle is stabilized in either of the bulk phases. Shaded area in green marks the region $|\omega| <1$.

For the points indicated in red in stage A, the graphene particle equilibrium was found in one of the bulk phases, irrespective of whether the graphene particle was initially located close to the interface or away from it. The graphene particle when initially placed at the interface, hovered close to the interface but was unable to adsorb there and eventually jumped into the bulk phase never to return. On the other hand, for the values indicated in green in stage A, the graphene particle was found to migrate spontaneously to the interface no matter what the initial location was. Once the graphene particle settled down at the interface, it remained stable there without making any jumps into the bulk even for

a period of around 10 ns. Figure 4 illustrates these two scenarios. For conciseness, only cases with ω>0 are presented. It can be seen for example in Figures 4a-4d and Figures 4i-4l (ω>1) that the graphene particle remains in the *n*-hexane phase after 2 ns, while it migrates to the interface in a shorter time in Figures 4e-4h and Figures 4m-4p (ω<1). The direct stage-A simulations confirm that the graphene particle adsorbs at the liquid-liquid interface for ω<1 for the AT and CG models as already predicted by the PMF calculations. Interestingly, negative values such as -1.5<ω<0 also yield interfacial adsorption.

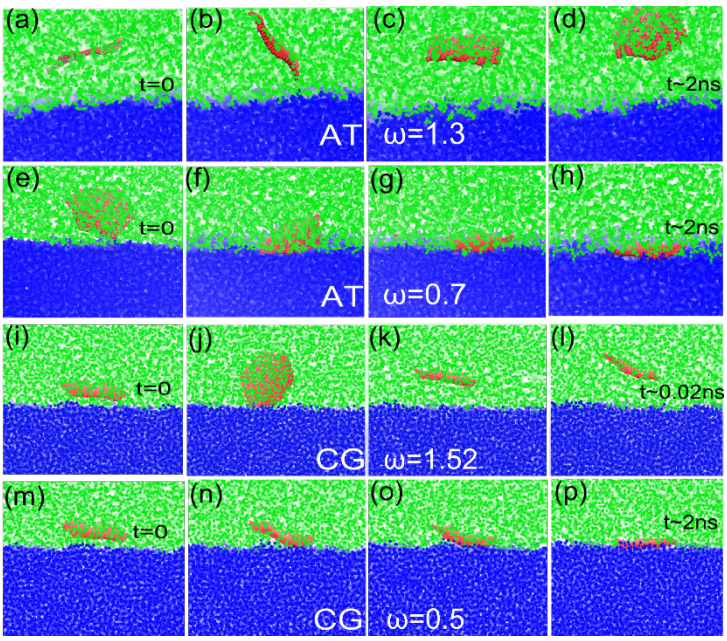

Figure 4. Representative snapshots taken from AT (figures a-h) and CG simulations (figures i-p) in stage A. For figures a-d, ω=1.3, for e-h, ω=0.7, for i-l, ω=1.52, for m-p ω=0.5. For a given row, time increase from left to right. Water is shown in blue, oil yellow and graphene particle in black.

In stage B, the simulations were initialized with graphene particle at the interface and then solid-liquid interactions were instantaneously modified to give new values of ω. The initial configurations chosen were equilibrated first for about 10 ns under *NVT* conditions with interactions set at ω=0.5 for both AT and CG systems. Starting from this arrangement, the force-field parameters were instantaneously switched to new values (Table S5). After the interactions were switched, simulations with the pressure perpendicular to the liquid-liquid interface maintained constant were performed for 200 ps to allow the system's density to relax. Simulations at constant volume and temperature (*NVT*) were performed then on. For the set of values indicated by red symbols in stage B in Figure 3, the graphene particle was found to spontaneously migrate to the bulk. For the ω values indicated by green symbols, the graphene particle just stayed at the interface for several nanoseconds, without moving into the bulk. Representative trajectories for both these cases are shown in Figure S10 (SI).

The stage-B simulations confirm the findings of the stage-A simulations. They show that the graphene particle does not spontaneously desorb from the interface when $|\omega| \leq 1 \pm 0.1$, whereas it desorbs when $|\omega| > 1.0 \pm 0.1$ for both the AT and CG systems. Given the statistical uncertainty in ω, these relatively simple simulations also confirm the PMF results, namely that a monolayer graphene particle adsorbs at the water-*n*-hexane interface for $\omega \approx 1$, both with the AT and CG resolutions. It should also be mentioned that there is a certain ambiguity, as to where the particle finally adsorbs when $|\omega|$ was chosen in the interval [1.0: 1.1] for the AT system and [0.9: 1.0] for the CG system, as seen by the contrasting results between stage A, B simulations, and PMFs. This could be attributed to the presence of a local minimum in the PMF like one at ω=1.1 as shown in Figure 1a in addition to the uncertainties in ω. In this interval of time, either the driving force or the sampling time may be too small to cross this barrier, preventing a jump from the initial position of the particle at the interface to be observed. Interestingly, adsorption was also observed for ω<0, possibly within $-1 \leq \omega < 0$. Although this observation tends to confirm the generality of the criterion $|\omega| < 1$ discussed in section 2, negative values of ω are not consistent with experiments. Indeed, ω<0 is interpreted as graphene having a better affinity for water than for *n*-alkanes, in contradiction with the observation that graphene interacts with water in the partial wetting regime, while alkanes tend to interact with graphene in the full wetting regime.

An additional observation to be made is that, the graphene particle diffuses at a much faster rate in the CG system when compared to the graphene particle in an AT system. This kind of behavior is much expected as the CG potentials are known to have smoother potential energy surfaces and therefore accelerated dynamics. As indicated by the approximate time scales in Figure 4, an acceleration of up to a couple of orders of magnitude was seen for the smallest of the particle sizes. The time-dependent variation of the mean-square displacements of the center of mass of the graphene particle parallel to the water-oil interface (at ω=0.5) in Figure S11 (SI) shows that, the diffusion of the graphene particle in the CG system is faster that the AT system by orders of magnitude. According to Stokes-Einstein law, diffusivity of a particle is inversely proportional to the surrounding fluid's viscosity. The CG *n*-hexane model derived using the CRW method[67] possesses significantly low viscosity when compared to its atomistic counterpart and thus speeds up the dynamics of the graphene particle. This observation means that, systems that are thermodynamically consistent with the AT systems can be simulated at a much faster rate at a fraction of the computational cost. Such CG models could be used to simulate and equilibrate much larger interfacial systems giving access to a great degree of heterogeneity, length, and time scales.

4.2 Many particles simulation

In the previous subsection, we discussed how one can reasonably use ω as a criterion to suitably model oil-water interfaces close to the experimental conditions. As already suggested via stages A and B simulations, the approach seems to be general and may yield interfacial adsorption as long as the condition $|\omega| \leq 1$ is satisfied. We performed simulations with several graphene particles at the interface as an illustration of the applicability of the potentials derived with ω=0.8 as suggested by the PMFs. The simulation cell consisted of a two water-*n*-hexane interfaces. The simulation procedure is detailed in section SXII of the SI. We observed that, all the graphene particles spontaneously migrated towards either of the liquid-liquid interfaces, regardless of whether they were initially placed in water or *n*-hexane phases. This behavior is the result of the imposed condition ω=0.8, i.e., ω<1. Graphene particles that were introduced far away from the interface did not feel the presence of the interface and diffused until they came near the interface where they finally adsorbed, as is illustrated in Figure 5. We noticed that, graphene particles stack on top of each other to form few-layer graphene particles. In Figures 5a-5d, a new graphene particle (black) is seen to join two graphene particles stacked by sandwiching hexane layer in between. The sandwiched hexane layer was found to be stable (for ~50 ns) and hints that this formation could significantly hamper energy transport and is a relevant occurrence that cannot be ignored while studying energy or electron transport through network of particles. In Figure 5e, a typical formation of a junction between two adjacent graphene particles is shown and further Figure 5f shows a snapshot of the water-oil interface crowded with several adsorbed particles.

The simulation discussed above is only an illustration of the capability of our approach. In principle, much larger interfaces spanning a great degree of heterogeneity in terms of graphene particle size and shape can be constructed. Such simulations are possible owing to the very fast dynamics of the CG models. A possible application of our approach is to study percolation in the two-dimensional arrangement of liquid-liquid interfaces or the formation of emulsions stabilized by interfacial nanoparticle adsorption through large scale CG simulations.

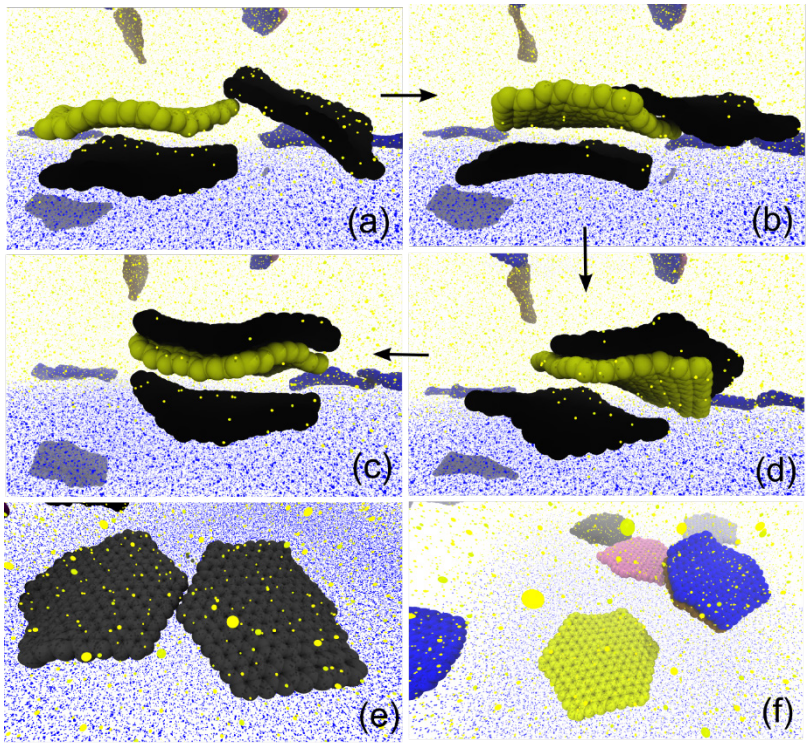

Figure 5. Snapshot of several graphene particle simulations near the water-oil interface. (a)-(d) show a set of graphene particles forming stacks. Interestingly, there is a hexane layer sandwiched between lower and center graphene particles (e) A typical connectivity between two adsorbed graphene particles is shown (f) A top view shows an interface crowded with several graphene particles.

5. CONCLUSIONS

A methodology was developed to derive atomistic and coarse-grained potentials to simulate the adsorption of nanoparticles at the interface between immiscible liquids. Although our approach aims to be general, we focused on the specific and experimentally relevant case of the adsorption of graphene nanoflakes at the interface between water and oily liquids, here represented by *n*-hexane. In such multi-component systems, one cannot rely on the usual mixing rules between force-field parameters to obtain accurate potentials. Therefore, the interaction potentials have to be optimized. Our methodology focuses on deriving the interaction potentials for the nanoparticle-liquid interactions while leaving the liquid-liquid interactions intact. The target quantity for the related optimization process is the wetting coefficient ω introduced in eq 1. This coefficient expresses the balance of interactions in a system where a thick planar nanoparticle adsorbs at the liquid-liquid interface. The challenge for atomistic and coarse-grained simulations is to be able to generate potentials that represent the balance of interactions that yield a given precise value of ω. To this end, we introduced an expression of ω which depends on measurable quantities that can be calculated through free-energy

calculations. These quantities directly depend on the force-field parameters to optimize and thus establish a connection between the models and the experimental system.

It was found that graphene adsorbs at the water-*n*-hexane interface for $\omega \approx 1$. Interestingly, such a value is also obtained based on interfacial thermodynamic quantities for the interaction between *n*-hexane, water and graphite, i.e., a stack of graphene layers. This observation suggests that the definition of ω is independent of the thickness of the particle as long as the interactions are short-ranged in nature.

It was also found that the coarse-grained potentials yield simulations that are at least an order of magnitude faster than atomistic simulations. An illustration of the applicability was shown by simulating many graphene particles adsorbing at the interface using a model system. Our approach to derive such potentials will thus be very useful in large scale simulations of systems like emulsions or molecular models for oil recovery where water, oily liquids and carbon particles are involved.

ASSOCIATED CONTENT

Supporting Information

The Supporting Information is available free of charge on the ACS Publications website at DOI: XXXX.

Estimates of the wetting coefficient from experiments. System sizes in the different simulations. Wetting coefficients of some chosen systems. Atomistic and coarse-grained representations of *n*-hexane. Interaction potentials and force-field parameters. Simulation cell. Potential of Mean Force calculations. Solid-liquid work of adhesion values and force field parameters used in the adsorption-desorption simulations. Trajectories in stage B simulations. Time dependence of the mean squared displacement of the graphene particles.

AUTHOR INFORMATION

Corresponding author

*v.ardham@theo.chemie.tu-darmstadt.de

Notes

The authors declare no competing financial interests.

ACKNOWLEDGEMENTS

We are grateful for financial support from the Collaborative Research Center Transregio TRR 146 Multiscale Simulation Methods for Soft Matter Systems funded by the Deutsche Forschungsgemeinschaft (DFG). We also would like to thank the HPC Center of Technische Universität Darmstadt for allocating computer time on the Lichtenberg Hochleistungsrechner and to the John von Neumann Institute for Computing at the Jülich Supercomputing Center for allocating computer time on JURECA. FL thanks the village of Maurach (Austria) and the Cité des Sciences et de l'Industrie (France) for providing access to the Internet and thus enabling him to achieve decisive steps in the preparation of this work.

REFERENCES

(1) Woltornist, S. J.; Oyer, A. J.; Carrillo, J. M. Y.; Dobrynin, A. V.; Adamson, D. H. Conductive Thin Films of Pristine Graphene by Solvent Interface Trapping. *ACS Nano* **2013**, *7*, 7062–7066.

(2) Woltornist, S. J.; Carrillo, J. M. Y.; Xu, T. O.; Dobrynin, A. V; Adamson, D. H. Polymer/pristine Graphene Based Composites: From Emulsions to Strong, Electrically Conducting Foams. *Macromolecules* **2015**, *48*, 687–693.

(3) He, Y.; Wu, F.; Sun, X.; Li, R.; Guo, Y.; Li, C.; Zhang, L.; Xing, F.; Wang, W.; Gao, J. Factors That Affect Pickering Emulsions Stabilized by Graphene Oxide. *Appl. Mater. Interfaces* **2013**, *5*, 4843–4855.

(4) Gudarzi, M. M.; Sharif, F. Self Assembly of Graphene Oxide at the Liquid–liquid Interface: A New Route to the Fabrication of Graphene Based Composites. *Soft Matter* **2011**, *7*, 3432-3440.

(5) Biswas, S.; Drzal, L. T. A Novel Approach to Create a Highly Ordered Monolayer Film of Graphene Nanosheets at the Liquid-Liquid Interface. *Nano Lett.* **2009**, *9*, 167–172.

(6) Wan, W.; Zhao, Z.; Hughes, T. C.; Qian, B.; Peng, S.; Hao, X.; Qiu, J. Graphene Oxide Liquid Crystal Pickering Emulsions and Their Assemblies. *Carbon* **2015**, *85*, 16–23.

(7) Kuilla, T.; Bhadra, S.; Yao, D.; Kim, N. H.; Bose, S.; Lee, J. H. Recent Advances in Graphene Based Polymer Composites. *Prog. Polym. Sci.* **2010**, *35*, 1350–1375.

(8) Wang, P.; Chong, H.; Zhang, J.; Lu, H. Constructing 3D Graphene Networks in Polymer Composites for Significantly Improved Electrical and Mechanical Properties. *ACS Appl. Mater. Interfaces* **2017**, *9*, 22006–22017.

(9) Zheng, R.; Gao, J.; Wang, J.; Feng, S.-P.; Ohtani, H.; Wang, J.; Chen, G. Thermal Percolation in Stable Graphite Suspensions. *Nano Lett.* **2012**, *12*, 188–192.

(10) Bento, J. L.; Brown, E.; Woltornist, S. J.; Adamson, D. H. Thermal and Electrical Properties

of Nanocomposites Based on Self-Assembled Pristine Graphene. *Adv. Funct. Mater.* **2017**, *27*, 1604277.

(11) Woltornist, S. J.; Varghese, D.; Massucci, D.; Cao, Z.; Dobrynin, A. V.; Adamson, D. H. Controlled 3D Assembly of Graphene Sheets to Build Conductive, Chemically Selective and Shape-Responsive Materials. *Adv. Mater.* **2017**, *29*, 1604947.

(12) Wang, Y.; Shan, J. W.; Weng, G. J. Percolation Threshold and Electrical Conductivity of Graphene-Based Nanocomposites with Filler Agglomeration and Interfacial Tunneling. *J. Appl. Phys.* **2015**, *118*, 065101.

(13) He, L.; Tjong, S. C. Carbon Nanotube/epoxy Resin Composite: Correlation between State of Nanotube Dispersion and Zener Tunneling Parameters. *Synth. Met.* **2012**, *162*, 2277–2281.

(14) Booth, S. G.; Dryfe, R. A. W. Assembly of Nanoscale Objects at the Liquid/Liquid Interface. *J. Phys. Chem. C* **2015**, *119*, 23295–23309.

(15) Böker, A.; He, J.; Emrick, T.; Russell, T. P. Self-Assembly of Nanoparticles at Interfaces. *Soft Matter* **2007**, *3*, 1231.

(16) Shao, J.; Lv, W.; Yang, Q. Self-Assembly of Graphene Oxide at Interfaces. *Adv. Mater.* **2014**, *26*, 5586–5612.

(17) Patra, D.; Sanyal, A.; Rotello, V. M. Colloidal Microcapsules: Self-Assembly of Nanoparticles at the Liquid-Liquid Interface. *Chem. - An Asian J.* **2010**, *5*, 2442–2453.

(18) Depa, P.; Chen, C.; Maranas, J. K. Why Are Coarse-Grained Force Fields Too Fast A Look at Dynamics of Four Coarse-Grained Polymers. *J. Chem. Phys.* **2011**, *134*, 14903.

(19) Carbone, P.; Varzaneh, H. A. K.; Chen, X.; Müller-Plathe, F. Transferability of Coarse-Grained Force Fields: The Polymer Case. *J. Chem. Phys.* **2008**, *128*, 64904.

(20) Depa, P. K.; Maranas, J. K. Speed up of Dynamic Observables in Coarse-Grained Molecular-Dynamics Simulations of Unentangled Polymers. *J. Chem. Phys.* **2005**, *123*, 94901.

(21) Fischer, J.; Paschek, D.; Geiger, A.; Sadowski, G. Modeling of Aqueous Poly(oxyethylene) Solutions. 2. Mesoscale Simulations. *J. Phys. Chem. B* **2008**, *112*, 13561–13571.

(22) Nielsen, S. O.; Lopez, C. F.; Srinivas, G.; Klein, M. L. Coarse Grain Models and the Computer Simulation of Soft Materials. *J. Phys. Condens. Matter* **2004**, *16*, 481–512.

(23) Hong, B.; Chremos, A.; Panagiotopoulos, A. Z. Dynamics in Coarse-Grained Models for Oligomer-Grafted Silica Nanoparticles. *J. Chem. Phys.* **2012**, *136*, 204904.

(24) Dallavalle, M.; Calvaresi, M.; Bottoni, A.; Melle-Franco, M.; Zerbetto, F. Graphene Can Wreak Havoc with Cell Membranes. *ACS Appl. Mater. Interfaces* **2015**, *7*, 4406–4414.

(25) Leroy, F. Revisiting the Droplet Simulation Approach to Derive Force-Field Parameters for Water on Molybdenum Disulfide from Wetting Angle Measurements. *J. Chem. Phys.* **2016**,

145, 164705.

(26) Riniker, S.; Allison, J. R.; van Gunsteren, W. F. On Developing Coarse-Grained Models for Biomolecular Simulation: A Review. *Phys. Chem. Chem. Phys.* **2012**, *14*, 12423.

(27) Müller-Plathe, F. Coarse-Graining in Polymer Simulation: From the Atomistic to the Mesoscopic Scale and Back. *ChemPhysChem* **2002**, *3*, 754–769.

(28) Louis, A. A. Beware of Density Dependent Pair Potentials. *J. Physics-Condensed Matter* **2002**, *14*, 9187–9206.

(29) Brini, E.; Algaer, E. A.; Ganguly, P.; Li, C.; Rodríguez-Ropero, F.; Vegt, N. F. A. Van Der. Systematic Coarse-Graining Methods for Soft Matter Simulations – a Review. *Soft Matter* **2013**, *9*, 2108–2119.

(30) Driskill, J.; Vanzo, D.; Bratko, D.; Luzar, A. Wetting Transparency of Graphene in Water. *J. Chem. Phys.* **2014**, *141*, 18C517.

(31) Fowkes, F. M. Attractive Forces at Interfaces. *Ind. Eng. Chem.* **1964**, *56*, 40–52.

(32) van Engers, C. D.; Cousens, N. E. A.; Babenko, V.; Britton, J.; Zappone, B.; Grobert, N.; Perkin, S. Direct Measurement of the Surface Energy of Graphene. *Nano Lett.* **2017**, *17*, 3815–3821.

(33) Kanduč, M.; Netz, R. R. Atomistic Simulations of Wetting Properties and Water Films on Hydrophilic Surfaces. *J. Chem. Phys.* **2017**, *146*, 164705–164704.

(34) Taherian, F.; Marcon, V.; van der Vegt, N. F. A.; Leroy, F. What Is the Contact Angle of Water on Graphene? *Langmuir* **2013**, *29*, 1457–1465.

(35) Kanduč, M. Going beyond the Standard Line Tension: Size-Dependent Contact Angles of Water Nanodroplets. *J. Chem. Phys.* **2017**, *147*, 174701.

(36) Schlangen, L. J. M.; Koopal, L. K.; Cohen Stuart, M. A.; Lyklema, J. Wettability: Thermodynamic Relationships between Vapour Adsorption and Wetting. *Colloids Surfaces A Physicochem. Eng. Asp.* **1994**, *89*, 157–167.

(37) Giro, R.; Bryant, P. W.; Engel, M.; Neumann, R. F.; Steiner, M. Adsorption Energy as a Metric for Wettability at the Nanoscale. *Sci. Rep.* **2016**, *7*, 46317.

(38) Santiso, E. E.; Herdes, C.; Müller, E. A. On the Calculation of Solid-Fluid Contact Angles from Molecular Dynamics. *Entropy* **2013**, *15*, 3734–3745.

(39) Ghoufi, A.; Malfreyt, P.; Tildesley, D. J. Computer Modelling of the Surface Tension of the Gas–liquid and Liquid–liquid Interface. *Chem. Soc. Rev.* **2016**, *45*, 1387–1409.

(40) Leroy, F.; Müller-Plathe, F. Dry-Surface Simulation Method for the Determination of the Work of Adhesion of Solid–Liquid Interfaces. *Langmuir* **2015**, *31*, 8335–8345.

(41) Ardham, V. R.; Deichmann, G.; van der Vegt, N. F. A.; Leroy, F. Solid-Liquid Work of

Adhesion of Coarse-Grained Models of N-Hexane on Graphene Layers Derived from the Conditional Reversible Work Method. *J. Chem. Phys.* **2015**, *143*, 243135.

(42) Leroy, F.; dos Santos, D. J. V. A.; Müller-Plathe, F. Interfacial Excess Free Energies of Solid-Liquid Interfaces by Molecular Dynamics Simulation and Thermodynamic Integration. *Macromol. Rapid Commun.* **2009**, *30*, 864–870.

(43) Bai, X.-M.; Li, M. Calculation of Solid-Liquid Interfacial Free Energy: A Classical Nucleation Theory Based Approach. *J. Chem. Phys.* **2006**, *124*, 124707.

(44) Hashimoto, R.; Shibuta, Y.; Suzuki, T. Estimation of Solid-Liquid Interfacial Energy from Gibbs-Thomson Effect: A Molecular Dynamics Study. *ISIJ Int.* **2011**, *51*, 1664–1667.

(45) Vega, C. Surface Tension of the Most Popular Models of Water by Using the Test-Area Simulation Method. *J. Chem. Phys.* **2007**, *126*, 154707.

(46) Tang, Z.; Zhuang, J.; Wang, X. Exfoliation of Graphene from Graphite and Their Self-assembly at the Oil−Water Interface. *Langmuir* **2010**, *26*, 9045–9049.

(47) Hirunpinyopas, W.; Rodgers, A. N. J.; Worrall, S. D.; Bissett, M. A.; Dryfe, R. A. W. Hydrogen Evolution at Liquid|Liquid Interfaces Catalyzed by 2D Materials. *Chem. Nano. Mat.* **2017**, *3*, 428–435.

(48) Lee, S. H.; Kim, H. W.; Hwang, J. O.; Lee, W. J.; Kwon, J.; Bielawski, C. W.; Ruoff, R. S.; Kim, S. O. Three-Dimensional Self-Assembly of Graphene Oxide Platelets into Mechanically Flexible Macroporous Carbon Films. *Angew. Chemie Int. Ed.* **2010**, *49*, 10084–10088.

(49) Kim, F.; Cote, L. J.; Huang, J. Graphene Oxide: Surface Activity and Two-Dimensional Assembly. *Adv. Mater.* **2010**, *22*, 1954–1958.

(50) Hoseini, S. J.; Bahrami, M.; Dehghani, M. Formation of Snowman-like Pt/Pd Thin Film and Pt/Pd/reduced-Graphene Oxide Thin Film at Liquid-Liquid Interface by Use of Organometallic Complexes, Suitable for Methanol Fuel Cells. *RSC Adv.* **2014**, *4*, 13796–13804.

(51) Plimpton, S. Fast Parallel Algorithms for Short-Range Molecular Dynamics. *J. Comput. Phys.* **1995**, *117*, 1–19.

(52) Nath, S. K.; Escobedo, F. A; de Pablo, J. J. On the Simulation of Vapor – Liquid Equilibria for Alkanes. *J. Chem. Phys.* **1998**, *108*, 9905–9911.

(53) Aguila-Hernandez, J.; Hernandez, I.; Trejo, A. Temperature Dependence of the Surface Tension for Binary Mixtures Of n-Butanenitrile +n-Alkanes. *Int. J. Thermophys.* **1995**, *16*, 45–52.

(54) Berendsen, H. J. C.; Grigera, J. R.; Straatsma, T. P. The Missing Term in Effective Pair Potentials. *J. Phys. Chem.* **1987**, *91*, 6269–6271.

(55) Isele-Holder, R. E.; Mitchell, W.; Hammond, J. R.; Kohlmeyer, A.; Ismail, A. E. Reconsidering Dispersion Potentials: Reduced Cutoffs in Mesh-Based Ewald Solvers Can Be Faster Than Truncation. *J. Chem. Theory Comput.* **2013**, *9*, 5412–5420.

(56) Ding, W.; Palaiokostas, M.; Orsi, M. Stress Testing the ELBA Water Model. *Mol. Simul.* **2016**, *42*, 337–346.

(57) Brini, E.; van der Vegt, N. F. A. Chemically Transferable Coarse-Grained Potentials from Conditional Reversible Work Calculations. *J. Chem. Phys.* **2012**, *137*, 154113.

(58) Jorgensen, W. L.; Maxwell, D. S.; Tirado-rives, J. Development and Testing of the OPLS All-Atom Force Field on Conformational Energetics and Properties of Organic Liquids. *J. Am. Chem. Soc* **1996**, *118*, 11225–11236.

(59) Stuart, S. J.; Tutein, A. B.; Harrison, J. A. A Reactive Potential for Hydrocarbons with Intermolecular Interactions. *J. Chem. Phys.* **2000**, *112*, 6472.

(60) Saien, J.; Rezvani Pour, A.; Asadabadi, S. Interfacial Tension of the *N* -Hexane–Water System under the Influence of Magnetite Nanoparticles and Sodium Dodecyl Sulfate Assembly at Different Temperatures. *J. Chem. Eng. Data* **2014**, *59*, 1835–1842.

(61) Ardham, V. R.; Leroy, F. Thermodynamics of Atomistic and Coarse-Grained Models of Water on Nonpolar Surfaces. *J. Chem. Phys.* **2017**, *147*, 74702.

(62) Martinez, L.; Andrade, R.; Birgin, E. G.; Martínez, J. M. PACKMOL: A Package for Building Initial Configurations for Molecular Dynamics Simulations. *J. Comput. Chem.* **2009**, *30*, 2157–2164.

(63) Torrie, G. M.; Valleau, J. P. Nonphysical Sampling Distributions in Monte Carlo Free-Energy Estimation: Umbrella Sampling. *J. Comput. Phys.* **1977**, *23*, 187–199

(64) Kästner, J.; Thiel, W. Bridging the Gap between Thermodynamic Integration and Umbrella Sampling Provides a Novel Analysis Method: “Umbrella Integration”. *J. Chem. Phys.* **2005**, *123*, 144104.

(65) Kozbial, A.; Trouba, C.; Liu, H.; Li, L. Characterization of the Intrinsic Water Wettability of Graphite Using Contact Angle Measurements: Effect of Defects on Static and Dynamic Contact Angles. *Langmuir* **2017**, *33*, 959–967.

(66) Kozbial, A.; Li, Z.; Sun, J.; Gong, X.; Zhou, F.; Wang, Y.; Xu, H.; Liu, H.; Li, L. Understanding the Intrinsic Water Wettability of Graphite. *Carbon* **2014**, *74*, 218–225.

(67) Deichmann, D.; Marcon, V.; van der Vegt N. F. A. Bottom-up Derivation of Conservative and Dissipative Interactions for Coarse-grained Molecular Liquids with the Conditional Reversible Work Method. *J. Chem. Phys.* **2014**, *141*, 223109.

Supporting Information for the article "Atomistic and Coarse-grained Modeling of the Adsorption of Graphene Nanoflakes at the Oil-Water Interface"

Vikram Reddy Ardham[1,*] *and Frédéric Leroy*[1,#]

[1]Eduard-Zintl-Institut für Anorganische und Physikalische Chemie, Technische Universität Darmstadt, Alarich-Weiss-Strasse 8, 64287 Darmstadt, Hessen, Germany

[#]Present address: Independent scientist, Île-de-France, France

*v.ardham@theo.chemie.tu-darmstadt.de

SI. Estimates of the wetting coefficient from experiments

The wetting coefficient ω for the particle at the water-*n*-hexane interface is defined following:

$$\omega = \frac{\gamma_{pw} - \gamma_{po}}{\gamma_{wo}}$$

where γ_{po} is the graphene-alkane interfacial tension, γ_{pw} the graphene-water interfacial tension and γ_{wo} the water-alkane interfacial tension. We estimate ω for graphite at the water-*n*-heptane interface using the experimental data of Fowkes.[S1] According to this work, $\gamma_{po}=\gamma_p+\gamma_o-2\ (\gamma_p^d\gamma_o^d)^{1/2}$ and $\gamma_{pw}=\gamma_p+\gamma_w-2\ (\gamma_p^d\gamma_w^d)^{1/2}$, where γ_p, γ_o and γ_w are the surface tensions of graphite, *n*-heptane and water, respectively. The quantities γ_p^d, γ_o^d and γ_w^d are the dispersion components of γ_p, γ_o and γ_w, respectively. According to Fowkes, at 20°C $\gamma_o=\gamma_o^d=20.4$ mJ/m^2, $\gamma_w=72$ mJ/m^2, $\gamma_w^d=21.8$ mJ/m2, $\gamma_{wo}=50.2$ mJ/m^2 and $\gamma_p^d=115$-132 mJ/m^2. Combining these values according to the equations above leads to $\omega=0.96$. According to van Engers *et al.* graphene (115 mJ/m^2) and graphite (119 mJ/m^2) have similar values of the surface energy γ_p.[S2] We thus conclude that $\omega\approx0.96$ for monolayer graphene at the water-*n*-heptane interface. For *n*-hexane $\gamma_o=\gamma_o^d=18.4$ mJ/m^2 and $\gamma_{wo}=51.1$ mJ/m^2, thus $\omega\approx0.89$ for graphene at the water-*n*-hexane interface.

SII. Illustration of the free energy change up on adsorption

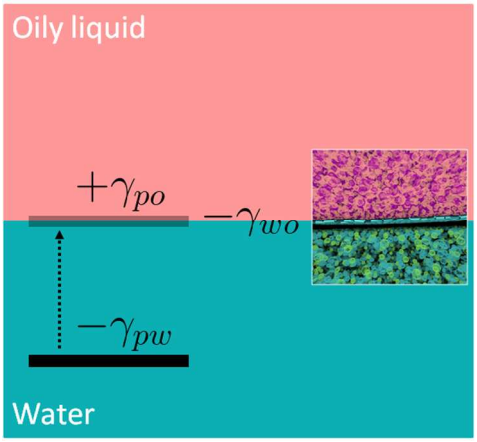

Figure S1. Illustration of the free energy change per unit area when a planar nanoparticle initially in water is relocated to the interface between water and an oily liquid. The inset is an atomic scale rendering of a graphene monolayer at the *n*-hexane-water interface. Here γ is the interfacial free tension and the subscripts, *p*, *o* and *w* refer to the graphene particle, oily phase (*n*-hexane here) and water respectively.

SIII. Wetting Coefficients of some chosen systems

	γ_O ($\gamma^d o$)	γ_{WO}	*Wpw*	*Wpo*	$\lvert\omega\rvert$	Ref
Cyclohexane/GR	25.5[S3] (25.5)	50.2[S1]	104.7	108.3	0.99	[S4]
1,2 DCB /GR and MoS_2	35.7[S5] (15.35)	40[S6]	104.7	84.02	0.39	[S7]
1,2 DCB /WS_2	35.7 (15.35)	40	104.7	74.09	0.40	[S7]
Water	72.8[S1] (21.8)	-	-	-	-	-
Benzene/GO	28.85[S1] (27.4)	34.1[S8]	116.06	69.46	0.74	[S9]
$CHCl_3$/GO	26.56[S10] (25.03)	31.6[S8]	116.06	67.15	0.73	[S11]
Hexane/GO	18.4[S1] (18.4)	51.1[S1]	116.06	48.04	0.07	[S12]
Toluene/GO	28.4[S3] (26.1)	36.1[S8]	116.06	70.86	0.04	[S11, S13]
MMA/GO	27[S14] (23.3)	50.3[S14]	116.06	71.60	0.04	[S14]

Table S1. Values of ω (based on eq 1 of the main manuscript) for various oil-water interfaces found in literature that lead to adsorption of a nanoparticle at the interface. GR is graphene and GO is graphene oxide. Values are at RT. First column is the surface tension of the oil and its dispersion component, other symbols have their usual meanings, with *w* referring to water, *o* to

oil and *p* to particle. Last column is the experimental reference where particle adsorption was seen at the water-oil interface.

The work of adhesion for water-graphene was chosen as, W_{pw}=104.7 mJ/m^2, assuming a contact angle of 64° and using $W_{pw}=\gamma_W(1+\cos\theta)$. W_{po} is approximated using the relation proposed by Good,[S15] $W_{op} = 2\sqrt{\gamma_p^d\gamma_o^d} + 2\sqrt{\gamma_p^p\gamma_o^p}$. Where superscripts, *d* and *p* refer to the dispersion and polar components of the interfacial tension. The dispersion and polar components of GO are taken from ref S8 and for GR, the polar component is equal to zero. The dispersion components of liquids are taken from the literature and in cases where they were not available (benzene and chloroform), equation 6 in ref S3 has been applied by using the values of known total surface-tension and interfacial tension with water. The values computed here are only approximate due to the scattered/unavailable experimental data and the approximate nature of the equations used to compute work of adhesion.

SIV. System sizes in different simulations

The system sizes for the calculation of the water and *n*-hexane surface tension as well as the water-*n*-hexane interfacial tension are given in Table S2 below.

	Atomistic	Coarse-grained
Water	10000 (4.8×4.8 nm^2)	10000 (6.2×6.2 nm^2)
n-hexane	1500 (5.1×5.1 nm^2)	1500 (4.4×4.3 nm^2)
Water-*n*-hexane	11500 (4.5×4.5 nm^2)	11500 (6.4×6.4 nm^2)

Table S2. System sizes in number of molecules for the calculations of the liquid surface tensions and water-*n*-hexane interfacial tension in the AT and CG simulations are given. The numbers in the parenthesis indicate the dimensions of the simulation cell parallel to the interface.

The system sizes for the PMF calculations are given in Table S3 below. The same simulation box was also used for the adsorption-desorption simulations.

	Atomistic	Coarse-grained
Number of water molecules	5450	5450
Number of n-hexane molecules	1200	1200
Cross sectional area	5.2×5.2 nm^2	5.2×5.2 nm^2

Table S3. System sizes in number of molecules and cross-sectional area of the simulations cell for the PMF calculations.

SV. Atomistic and coarse-grained representations of *n*-hexane

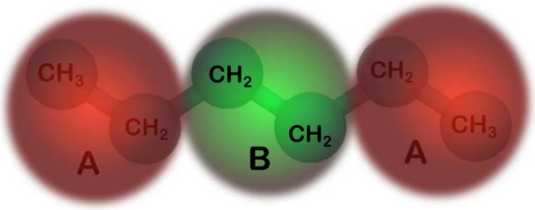

Figure S2. CH_3-CH_2-CH_2-CH_2-CH_2-CH_3 is the united atom representation of *n*-hexane with atomistic resolution. A-B-A is the coarse-grained representation of *n*-hexane.

SVI. Interaction potentials and force-field parameters

For the CG system, the water-*n*-hexane pair interaction potentials obtained from the CRW calculations were further optimized by varying the scaling parameter α (as defined in eq 7 of the manuscript) to reproduce the water-*n*-hexane interfacial tension γ_{wo} at 323 K. The variation of γ_{wo} with respect to α is shown in Figure S2 below.

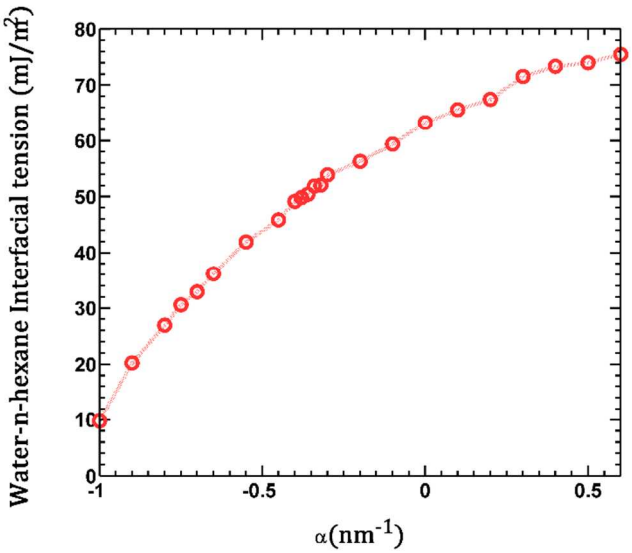

Figure S3. Variation of γ_{wo} depending on α. The error bars are around 2-3 mJ/m^2.

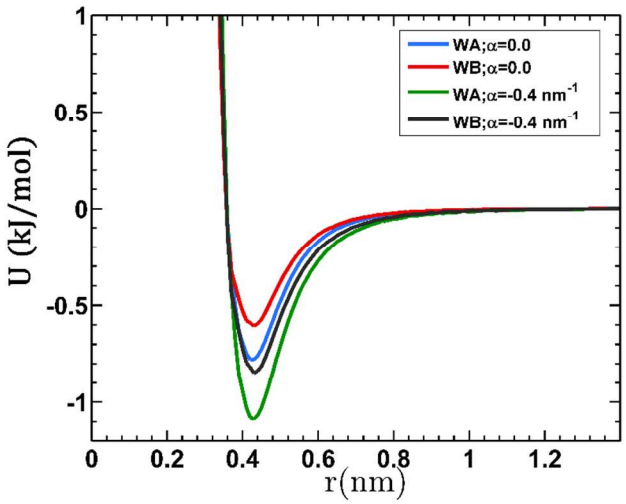

Figure S4. Coarse-grained interaction potentials between water (W) and either the A or B bead of *n*-hexane. The blue and the red curves are the potentials obtained through the CRW method. The green and black curves are the rescaled potentials obtained with α=-0.4 nm^{-1}.

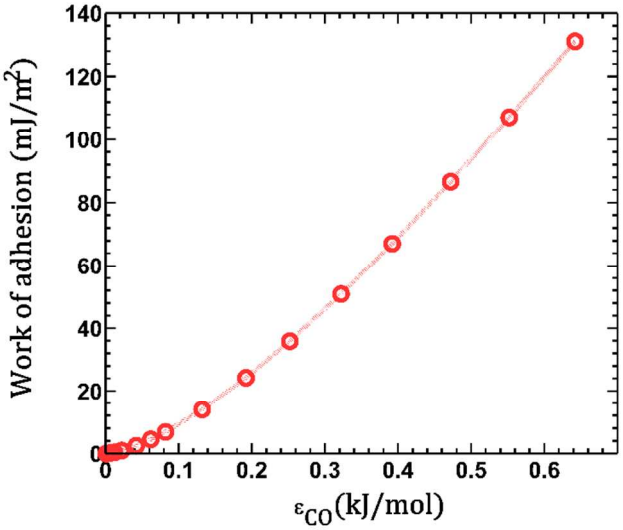

Figure S5. Graphene-water work of adhesion depending on the water-carbon Lennard-Jones energy parameter for the atomistic system. The curve was obtained through the approach formalized in eq 8 of the manuscript. ε_{CO} is the corresponding LJ energy parameter.

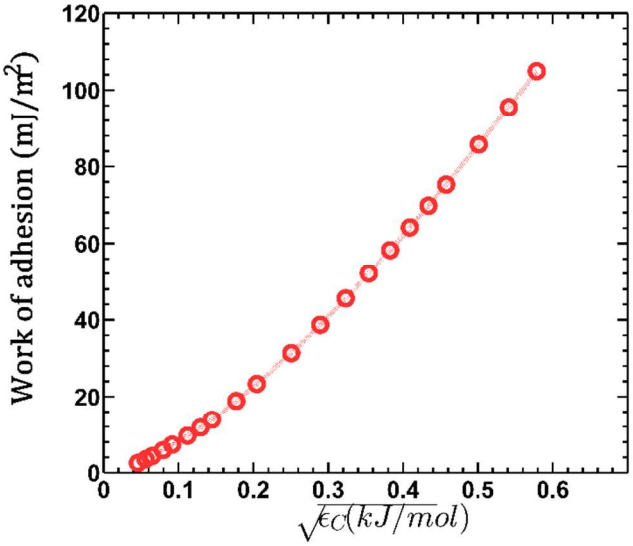

Figure S6. Graphene-*n*-hexane work of adhesion depending on the Lennard-Jones energy parameter for carbon for the atomistic system. The curve was obtained through the approach formalized in eq 9 of the manuscript. ε_C is the corresponding LJ energy parameter.

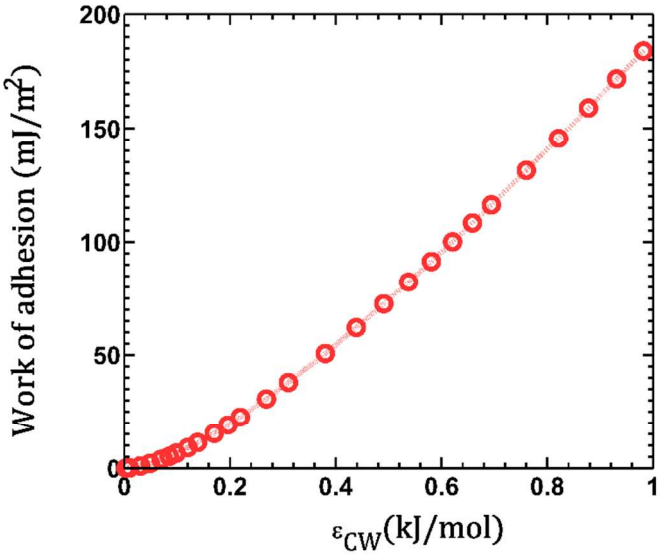

Figure S7. Graphene-water work of adhesion depending on the Lennard-Jones energy parameter between graphene carbon and water bead for the coarse-grained system. The curve was obtained through the approach formalized in eq 8 of the manuscript. ε_{CW} is the corresponding LJ energy parameter.

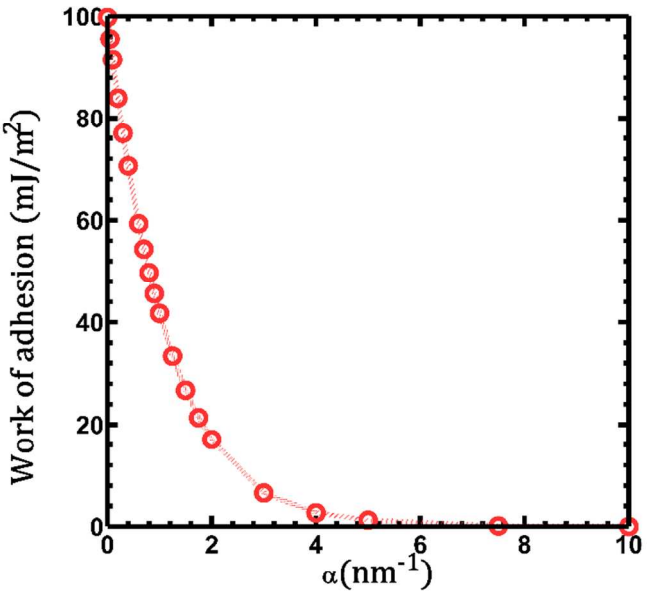

Figure S8. Graphene-*n*-hexane work of adhesion depending on the potential scaling parameter α for the coarse-grained system. The curve was obtained through the approach formalized in eq 10 of the manuscript.

SVII. Simulation cell

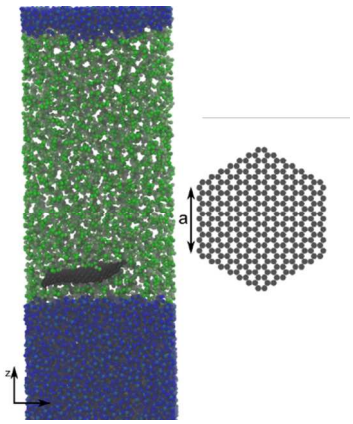

Figure S9. Left: Illustration of the simulation cell arrangement with *n*-hexane in green, water in blue, and the graphene particle in black. Right: A separate instance of the particle with hexagonal shape.

SVIII. Potential of Mean Force (PMF) calculations

The PMFs were computed using the Umbrella Integration method by combining the several windows sampled by applying a spring force to the center of mass of the graphene particle. The simulations were performed under *NVT* conditions with a Langevin thermostat with a time constant of 0.1 ps. The potential (U) applied by the spring is given by

$$U_{Spring} = \frac{K}{2}(z_{com} - z^*)^2$$

where K was set to 52300 kJ/mol/nm^2 and z_{com} is the center of mass of the graphene sheet. A similar spring with a force constant of 313800 kJ/mol/nm^2 was attached to the center of mass of water molecules to prevent the interface from moving. Several windows were simulated around the interface by choosing z* appropriately with a spacing of 0.02 nm. The initial structure for the

simulations consisted of a particle that was at the interface obtained after equilibration with same set of interactions. The PMFs were also computed with the standard WHAM method and no significant difference was seen. The interaction parameters used are given below.

Atomistic				
ε_C/ kJ/mol	W_{po} /mJ/m^2	ε_{CO}/ kJ/mol	W_{pw} / mJ/m^2	ω
0.2582	87	0.4627	84.2	1.00
0.2785	92	0.4627	84.2	1.10
0.2988	97	0.4627	84.2	1.20
Coarse-grained				
α/ nm^{-1}	W_{po} /mJ/m^2	ε_{CW}/ kJ/mol	W_{pw} / mJ/m^2	ω
0.3828	71.6	0.5598	87	0.80
0.3060	76.5	0.5598	87	0.90
0.2373	81.2	0.5598	87	1.00
0.1693	86.2	0.5598	87	1.10

Table S4. Parameters used for the PMF calculations. ε is the corresponding LJ energy parameter, W is the work of adhesion, ω is the wetting coefficient and subscripts, p, o and w refer to graphene particle, *n*-hexane and water respectively. Subscripts C, O and W denote the graphene carbon atom, oxygen atom in water and the water bead of the ELBA model respectively.

SIX. Graphene-liquid work of adhesion values and force field parameters used in the adsorption-desorption simulations (stage A and stage B simulations)

Atomistic, Stage A					
ε_C kJ/mol	W_{po} mJ/m^2	ε_{CO} kJ/mol	W_{pw} mJ/m^2	ω	Approx. Error in ω
0.01027	5.9	0.7390	160.0	-2.04	0.12
0.01027	5.9	0.6978	147.5	-1.80	0.11
0.01027	5.9	0.6444	132.0	-1.50	0.1
0.0222	13.9	0.5430	104.5	-0.81	0.08
0.0151	9.55	0.4627	84.2	-0.50	0.07
0.0719	35.3	0.4627	84.2	0.0	-
0.1568	61	0.4627	84.2	0.50	0.09
0.1743	65.7	0.4627	84.2	0.59	0.09

0.1965	71.5	0.4627	84.2	0.70	0.09
0.2582	87	0.4627	84.2	1.0	0.10
0.2988	97	0.4627	84.2	1.20	0.10
0.3110	100	0.4627	84.2	1.25	0.11
0.3200	102.2	0.4627	84.2	1.30	0.11
0.3406	107.3	0.4627	84.2	1.40	0.11
0.3616	112.5	0.4627	84.2	1.50	0.11
Atomistic, Stage B					
0.01027	5.9	0.6266	127.0	-1.40	0.1
0.01027	5.9	0.6085	122.0	-1.30	0.09
0.01027	5.9	0.5901	117.0	-1.21	0.09
0.01027	5.9	0.5692	111.4	-1.10	0.09
0.2784	92	0.4627	84.2	1.10	0.10
0.2988	97	0.4627	84.2	1.20	0.11
0.3200	102.2	0.4627	84.2	1.30	0.11
0.3406	107.3	0.4627	84.2	1.40	0.11
0.3616	112.5	0.4627	84.2	1.50	0.12
Coarse-grained, Stage A					
α nm^{-1}	W_{po} mJ/m^2	ε_{CW} kJ/mol	W_{pw} mJ/m^2	ω	Approx. Error in ω
3	6.5	0.8318	150.0	-1.80	0.1
3	6.5	0.7731	135.3	-1.50	0.09
1.8256	20.0	0.6555	107.8	-0.67	0.08
2.7391	7.4	0.5598	87.0	-0.50	0.06
1.296	32.0	0.5598	87.0	0.0	-
0.7665	51.3	0.5598	87.0	0.39	0.08
0.6630	56.2	0.5598	87.0	0.49	0.08
0.5652	61.2	0.5598	87.0	0.59	0.08
0.1933	84.4	0.5598	87.0	1.06	0.09
0	100.0	0.5263	80.0	1.52	0.09
Coarse-grained, Stage B					
3	6.5	0.7731	135.3	-1.50	0.09
3	6.5	0.7525	130.3	-1.39	0.09
3	6.5	0.7319	125.4	-1.30	0.08
3	6.5	0.7111	120.5	-1.20	0.08
3	6.5	0.6899	115.6	-1.10	0.07
0.2373	81.2	0.5598	87.0	1.00	0.10
0.1693	86.2	0.5598	87.0	1.10	0.09
0.1078	91	0.5598	87.0	1.20	0.09
0.0459	96	0.5598	87.0	1.30	0.09
0.0520	95.5	0.5321	81.2	1.40	0.09
0	100.0	0.5321	81.2	1.50	0.09

Table S5. Force-field parameters and the corresponding work of adhesion values employed to vary the wetting coefficient ω in the atomistic and CG simulations. ε is the corresponding LJ energy parameter, W is the work of adhesion, ω is the wetting coefficient and subscripts, p, o and w refer to graphene particle, *n*-hexane and water respectively. Subscripts C, O and W denote the graphene carbon atom, oxygen atom in water and the water bead of the ELBA model respectively.

SX. Trajectories in stage B simulations

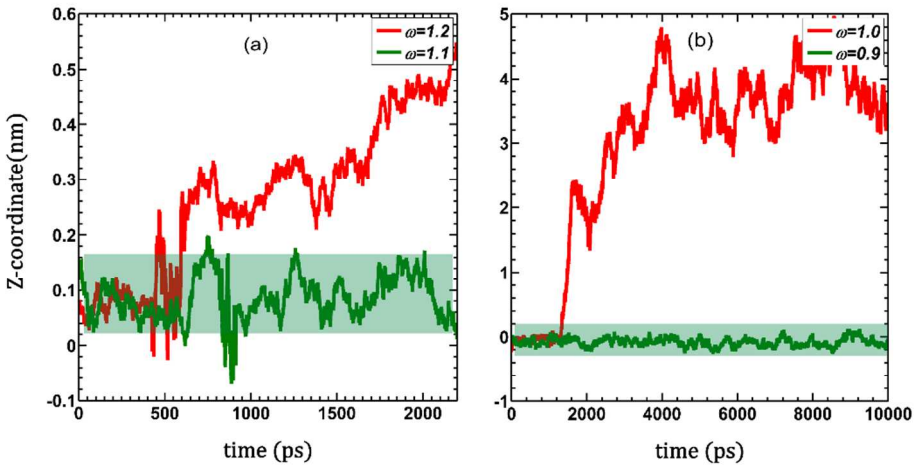

Figure S10. Typical trajectory of the center of mass of the particle in the direction perpendicular to the interface (z-axis) is shown for AT (a) and CG (b) systems in stage B. At time=0 ps, the ω (wetting coefficient) values were switched from 0.5 to the values indicated in the plot. The shaded region in green roughly denotes the interfacial region. The region above the shaded region is *n*-hexane and below is water.

SXI. Time dependence of the mean squared displacement of the graphene particles

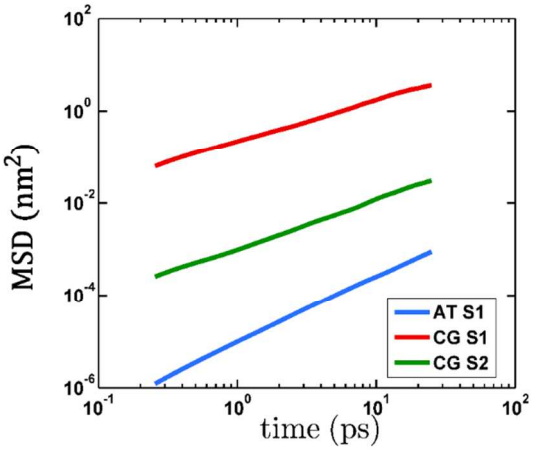

Figure S11. Mean-squared displacement (MSD) of the particle center of mass in the direction parallel to the interface, plotted with respect to time. The sizes S1 and S2 for the hexagonal graphene particles are given in Table S6 below. AT refers to atomistic system and CG refers to the coarse-grained system.

System	a / nm	N_C	N_o	N_w	A / nm^2	A_p/A
S1	1.8	294	1200	5450	5.2 × 5.2	0.31
S2	3.2	1014	2885	13350	8.2 × 8.2	0.39

Table S6. Sizes of the systems for the MSD simulations. The parameter a is the edge length of the hexagonal graphene particle, N_C is the number of carbon atoms in the particle, N_o is the number of *n*-hexane molecules, N_w is the number of water particles, A is the cross-section area of the simulation cell and A_p/A is the ratio between the area of the graphene flake and the simulation cell lateral dimension. S1 is the size of the particle that is used in the calculations discussed in the manuscript.

SXII. Many particles simulation

The cross-sectional area of the liquid-liquid interface was 14.6×14.6 nm^2. The size of the graphene particle is the same as the one presented in most of the results which is denoted by S1

in Table S3. One graphene particle was inserted randomly into the liquids every 1ns. For the 5 ps after insertion, the particle only interacted through soft potentials with the liquid and then the target interactions were switched on. A total of ten particles were inserted and the system was equilibrated under constant volume and constant temperature conditions (*NVT*). The interaction between the different graphene sheets was modelled using LJ interactions,[S16] while AIREBO interactions were retained for the interactions within the graphene sheets. The equations of motion were integrated using the multi-step integrator RESPA[S17] using a time step of 2 fs for the non-bonded interactions and 0.5 fs for the bonded and reactive force-field interactions.

References

(S1) Fowkes, F. M. Attractive Forces at Interfaces. *Ind. Eng. Chem.* **1964**, *56*, 40–52.

(S2) van Engers, C. D.; Cousens, N. E. A.; Babenko, V.; Britton, J.; Zappone, B.; Grobert, N.; Perkin, S. Direct Measurement of the Surface Energy of Graphene. *Nano Lett.* **2017**, *17*, 3815–3821.

(S3) Two-Component Surface Energy Characterization as a Predictor of Wettability and Dispersability. *Krüss GmbH* **2000**. https://www.kruss-scientific.com/fileadmin/user_upload/website/literature/kruss-ar213-en.pdf (accessed on Dec 23 2017).

(S4) Tang, Z.; Zhuang, J.; Wang, X. Exfoliation of Graphene from Graphite and Their Self-Assembly at the Oil−Water Interface. *Langmuir* **2010**, *26*, 9045–9049.

(S5) From the United States Environmental Protection Agency (EPA) Database (accessed on Dec 23 2017).

(S6) From the website: https://cameochemicals.noaa.gov/chris/DBO.pdf (accessed on Dec 23 2017).

(S7) Hirunpinyopas, W.; Rodgers, A. N. J.; Worrall, S. D.; Bissett, M. A.; Dryfe, R. A. W. Hydrogen Evolution at Liquid|Liquid Interfaces Catalyzed by 2D Materials. *Chem. Nano. Mat.* **2017**, *3*, 428–435.

(S8) Moghaddam, S. Z.; Sabury, S.; Sharif, F. Supporting Information for Dispersion of rGO in Polymeric Matrices by Thermodynamically Favorable Self-Assembly of GO at Oil-Water Interfaces. http://www.rsc.org/suppdata/ra/c3/c3ra46342g/c3ra46342g.pdf (accessed on Dec 23 2017).

(S9) Lee, S. H.; Kim, H. W.; Hwang, J. O.; Lee, W. J.; Kwon, J.; Bielawski, C. W.; Ruoff, R. S.; Kim, S. O. Three-Dimensional Self-Assembly of Graphene Oxide Platelets into Mechanically Flexible Macroporous Carbon Films. *Angew. Chemie Int. Ed.* **2010**, *49*, 10084–10088.

(S10) Surface Tension of Chloroform from *Dortmund Data Bank* (accessed on Dec 24 2017).

(S11) Kim, F.; Cote, L. J.; Huang, J. Graphene Oxide: Surface Activity and Two-Dimensional Assembly. *Adv. Mater.* **2010**, *22*, 1954–1958.
(S12) Creighton, M. A.; Zhu, W.; van Krieken, F.; Petteruti, R. A.; Gao, H.; Hurt, R. H. Three-Dimensional Graphene-Based Microbarriers for Controlling Release and Reactivity in Colloidal Liquid Phases. *ACS Nano* **2016**, *10*, 2268–2276.
(S13) Hoseini, S. J.; Bahrami, M.; Dehghani, M. Formation of Snowman-like Pt/Pd Thin Film and Pt/Pd/reduced-Graphene Oxide Thin Film at Liquid-Liquid Interface by Use of Organometallic Complexes, Suitable for Methanol Fuel Cells. *RSC Adv.* **2014**, *4*, 13796–13804.
(S14) Gudarzi, M. M.; Sharif, F. Self Assembly of Graphene Oxide at the Liquid-Liquid Interface: A New Route to the Fabrication of Graphene Based Composites. *Soft Matter* **2011**, *7*, 3432–3440.
(S15) Good, R. J.; Girifalco, L. A. A Theory for Estimation of Surface and Interfacial Energies. Iii. Estimation of Surface Energies of Solids from Contact Angle Data. *J. Phys. Chem.* **1960**, *64*, 561–565.
(S16) Lindsay, L.; Broido, D. A. Optimized Tersoff and Brenner Empirical Potential Parameters for Lattice Dynamics and Phonon Thermal Transport in Carbon Nanotubes and Graphene. *Phys. Rev. B* **2010**, *81*, 205441.
(S17) Tuckerman, M.; Berne, B. J.; Martyna, G. J. Reversible Multiple Time Scale Molecular Dynamics. *J. Chem. Phys.* **1992**, *97*, 1990–2001.

CHAPTER # 5

THE JOURNAL OF CHEMICAL PHYSICS **147**, 151102 (2017)

Communication: Is a coarse-grained model for water sufficient to compute Kapitza conductance on non-polar surfaces?

Vikram Reddy Ardham[a)] and Frédéric Leroy
Eduard-Zintl-Institut für Anorganische und Physikalische Chemie, Technische Universität Darmstadt, Alarich-Weiss-Strasse 8, 64287 Darmstadt, Germany

(Received 4 September 2017; accepted 9 October 2017; published online 20 October 2017)

Coarse-grained models have increasingly been used in large-scale particle-based simulations. However, due to their lack of degrees of freedom, it is *a priori* unlikely that they straightforwardly represent thermal properties with the same accuracy as their atomistic counterparts. We take a first step in addressing the impact of liquid coarse-graining on interfacial heat conduction by showing that an atomistic and a coarse-grained model of water may yield similar values of the Kapitza conductance on few-layer graphene with interactions ranging from hydrophobic to mildly hydrophilic. By design the water models employed yield similar liquid layer structures on the graphene surfaces. Moreover, they share common vibration properties close to the surfaces and thus couple with the vibrations of graphene in a similar way. These common properties explain why they yield similar Kapitza conductance values despite their bulk thermal conductivity differing by more than a factor of two. *Published by AIP Publishing.* https://doi.org/10.1063/1.5003199

The Kapitza conductance G (also called thermal boundary conductance or interfacial thermal conductance) and the reciprocal quantity called Kapitza resistance are important to quantify heat transfer through interfaces at the nanoscale. Knowledge of the underlying physical principles that determine G is of great relevance in many practical situations where interfaces are present, like in nanofluids or nanocomposites. A typical technological problem that requires better understanding of interfacial heat transfer is the difficulty to dissipate heat in modern microelectronic devices. As Balandin put it, "*Heat is one of the worst enemies of electronics.*"[1] Numerous experimental and theoretical studies as well as molecular dynamics (MD) simulations have been carried out to tackle such problems. In this context, the interfacial thermal behavior of water on solid substrates has received special attention. Such systems can be seen as prototypes that can be addressed through realistic models in particle-based simulations to better understand the mechanisms of heat transfer between hard and soft materials. We briefly discuss below the related findings on which our work builds. Interested readers may refer to Refs. 2 and 3 or 4 and references therein for a broader overview.

It was observed on surfaces decorated with self-assembled monolayers with different head groups that G generally increases with the water-solid interaction strength approximately through a linear relationship between G and the work of adhesion W_{SL}.[5–8] This quantity is connected to the contact angle θ, which is a visible macroscopic measure of the affinity of a given liquid for a given surface. For nonpolar surfaces, W_{SL} and θ are connected through $W_{SL} = \gamma(1 + \cos\theta)$, where γ is the liquid surface tension. In MD simulations, such a linear relationship was found on solids like graphite or silicon whose interaction strength with water was tuned through force-field parameters.[2,3] However, it was also found that G strongly depends on the thickness of the substrate[2] and on its crystallographic orientation.[9]

Recent studies on nonpolar surfaces have demonstrated that G is strongly influenced by the water molecules in the immediate vicinity of the substrate.[2,9] In this region, water adopts a layer structure with oscillations in the number density perpendicular to the surface. However, the layer structure tends to disappear when W_{SL} decreases.[10] Some of the water properties within the layers like orientation dynamics[11] and local compressibility[12,13] are altered compared to their bulk counterparts. In fact, local compressibility in the layers decreases when W_{SL} increases. Thus, although these water layers are liquid, changes induced by the interaction with the surface indicate rigidification compared with bulk water. In a contribution inspired by a phonon theory of liquids,[14,15] Mérabia *et al.* noted that "*interfacial energy transport at solid/water interfaces is to a very large extent mediated by high-frequency vibrations, for which liquid water behaves as a solid.*"[4] Note that these authors developed their approach based on bulk water vibration properties. However, the special role played by the high-frequency vibrations they mention suggests that the increased rigid character of the water structure within the adsorbed layers associated with the rise of W_{SL} may promote interfacial heat conduction.

In a recent work,[16] we showed that single-site coarse-grained (CG) models may also adopt the layer structure of water next to nonpolar surfaces like few-layer graphene. More precisely, we found that the atomistic model SPC/E and the CG model mW described below yield very similar layer structures and values of W_{SL} on graphene surfaces upon varying the strength of the water-carbon interaction. In light of the reasoning above that connects the water layer structure on surfaces

[a)]Author to whom correspondence should be addressed: v.ardham@theo.chemie.tu-darmstadt.de

with W_{SL} and G, we hypothesize that mW might yield variation of G against W_{SL} similar to SPC/E despite the missing atomistic details and the corresponding reduced number of degrees of freedom. The validity of this assumption is demonstrated and rationalized below.

We performed simulations in which water was represented by the SPC/E[17] and mW[18] models. While SPC/E is a rigid atomistic model with the three atoms of water, mW is a single-site single-molecule CG model. Hydrogen bonds are explicitly represented in SPC/E through electrostatic interactions. As for mW, Molinero and Moore mentioned that "*mW mimics the hydrogen-bonded structure of water through the introduction of a nonbonded angular dependent term* (i.e., a Stillinger-Weber three-body potential[19]) *that encourages tetrahedral configurations.*" Graphene was modeled with atomistic details following Alexeev *et al.*[2] Water and graphene interacted through a 12-6 Lennard-Jones potential. The wetting strength was changed by tuning the potential energy parameter ε_{SL} to obtain work of adhesion values ranging from 6 to about 100 mJ/m^2 (see the supplementary material for detailed information). Note that $W_{SL} \approx 100$ mJ/m^2 corresponds to $\theta \approx 65°$, which is a value typically obtained in experiments on highly ordered pyrolytic graphite that take surface contamination by airborne compounds into account.[20] On monolayer graphene free of contamination, $\theta = 85° \pm 5°$ ($W_{SL} = 78 \pm 6$ mJ/m^2).[21] Note that the carbon surfaces with the lowest values of W_{SL} in our study should be regarded as model systems employed to enhance our understanding.

The Kapitza conductance between water and few-layer graphene was computed at an average temperature of 300 K and a pressure of 1 atm using the MD simulation package LAMMPS.[22] The non-equilibrium MD (NEMD) setup employed was similar to the implementation used in Ref. 2 with 12 carbon layers on each side of the simulation cell, as shown in Fig. S1 of the supplementary material. Further information on the simulation procedure is given in the supplementary material. The thermal conductivity k of water in the sandwiched films was evaluated as the ratio of the heat flux Q and the temperature gradient in the film. For both SPC/E and mW at all W_{SL}, the values obtained were in quantitative agreement with the corresponding liquid bulk thermal conductivity simulations (see below). Finally, it should be mentioned that the thermal conductance measured by the setup above yields the combined conductance of the graphene-graphene and graphene-water interfaces as explained in Ref. 23. Further, the absolute values of thermal properties may depend on the force field and the method employed.[24] However, these facts should not alter the conclusions we draw as we compare two models with the exact same setup. The way the number of graphene layers influences G should be identical for both the studied water models, and what we refer to as G in fact accounts for the contribution of the solid-liquid and the inter-layer graphene conductances.

We briefly discuss some bulk and interfacial structure properties of SPC/E and mW that are relevant for the question we address. Both models yield very similar densities (990 kg/m^3 for SPC/E and 998 kg/m^3 for mW). They also lead to the typical short-range tetrahedral order of water that

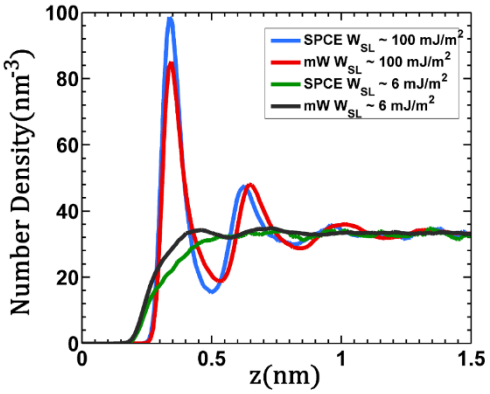

FIG. 1. Number density distribution of water on graphite (located at $z \leq 0$) calculated at two different wetting strengths for both the models. The coordinate z is the distance from the surface.

arises from hydrogen bonds (not shown). Owing to these similarities, it can be seen in Fig. 1 that SPC/E and mW lead to comparable distributions of the number density of water on graphene layers with the typical liquid layer structure perpendicular to the interface. When the water-surface coupling decreases, the water layer structure gradually disappears for both models and vanishes for $W_{SL} \approx 15$–20 mJ/m^2. At $W_{SL} \approx 6$ mJ/m^2 in Fig. 1, no layer structure is visible for SPC/E, while the maximum at about 0.45 nm for mW is not representative of the solid-liquid interaction but of the liquid-vapor interface. When water interacts with nonpolar substrates like graphene, tetrahedral order in the first layer of adsorbed molecules is perturbed due to the surface. However, for both water models, we found that molecules in the second adsorbed layer and beyond adopt short-range tetrahedral order like in the liquid bulk, independently of the solid-liquid interaction strength. Thus, despite the difference in the number of degrees of freedom between SPC/E and mW, these models adapt their structure in response to the presence of a nonpolar surface in a similar way. Furthermore, both models yield very similar structures of water at the interface. In contrast, the lack of degrees of freedom in mW strongly affects the properties related to thermal transport. We found through equilibrium simulations (see the supplementary material) that the isobaric specific heat capacity of SPC/E and mW was 84.9 J/mol K and 33.2 J/mol K, respectively. Both models yield different values of the thermal conductivity k. It was found through NEMD simulations that k = 0.83 ± 0.04 W/Km for SPC/E and k = 0.34 ± 0.01 W/Km for mW (see the supplementary material).

We now discuss the variation of G for SPC/E and mW depending on W_{SL}. It can be seen in Fig. 2 that G increases with W_{SL} for both SPC/E and mW. The variation is linear for $W_{SL} > 40$ mJ/m^2. These observations are in line with several earlier studies on solid-liquid systems.[2,8,9,25] Moreover, the numerical magnitude of G is in close proximity to the values of Alexeev *et al.*[2] It can also be observed that below W_{SL} = 40 mJ/m^2 the rate with which G increases is slightly larger than above, in agreement with the finding of Xue *et al.* on the effect of the wetting regime on $1/G$.[25] The most striking result is that SPC/E and mW lead to variations of G against W_{SL}

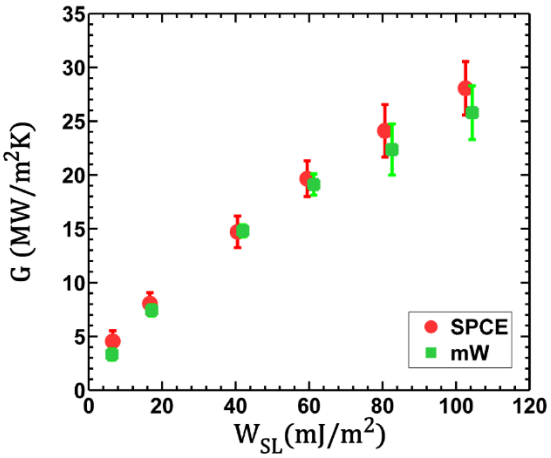

FIG. 2. Interfacial thermal conductance depending on the solid-liquid work of adhesion for SPC/E (red) and mW (green).

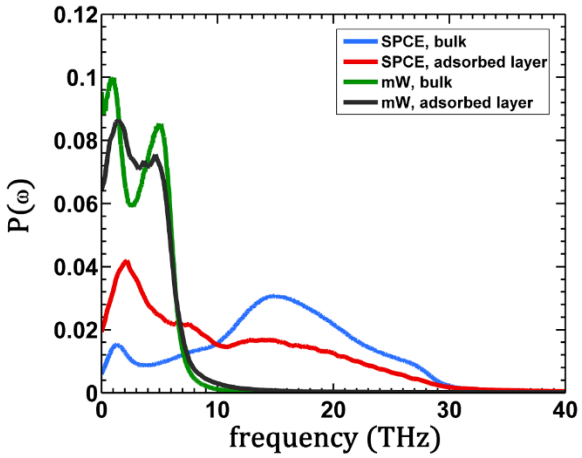

FIG. 3. Vibration spectrum for bulk water for SPC/E (blue) and mW (green) along with the vibration spectrum of the water molecules in the first adsorbed layer for SPC/E (red) and mW (black) at $W_{SL} \approx 100$ mJ/m^2. All spectra were normalized to ease the comparison.

that are quantitatively similar. Note that G seems to diverge between the two models at the greatest W_{SL} values, although the effect is weak. In fact, additional simulations in the fully wetting regime ($\theta = 0°$) at $W_{SL} \approx 230$ mJ/m^2 showed that even for such a strong solid-liquid interaction, the difference in G between SPC/E and mW is similar to the difference at 100 mJ/m^2 (note that $G \approx 45$ MW/m^2 K at that W_{SL} value). The result in Fig. 2 is therefore in strong contrast with k for the two models and is in line with the idea that interfacial properties like G cannot be trivially obtained by combining individual bulk properties.[26]

To understand the behavior of G with respect to W_{SL}, a spectral analysis was performed. We first discuss the equilibrium bulk and interfacial vibration properties of the water models through their vibration spectrum obtained from

$$P(\omega) = \sum_i m_i |\tilde{v}_i(\omega)|^2, \quad (1)$$

where the summation is performed over all liquid particles, m is their respective mass, and $\tilde{v}_i(\omega)$ is the Fourier-transform of the velocity time-series. Further information on the calculation of $P(\omega)$ is given in the supplementary material. It can be seen in Fig. 3 that SPC/E has a bulk spectrum that spans a broader frequency range than mW. The atomistic model in the bulk yields a relatively narrow band centered on 1.5 THz and a broader one centered on 15 THz. These bands correspond to translational and rotational librations, respectively.[27] When SPC/E interacts with the surface, the maximum at 1.5 THz is shifted to about 2.5 THz while the band for the rotational librations is slightly red-shifted. Due to the presence of the surface, molecular packing in the first adsorbed layer of water is tighter and rotational motions are hampered. Consequently, the magnitude of $P(\omega)$ for the rotational librations is underrepresented compared to the translational ones. In addition to a band at 1 THz for translational librations, mW in the bulk yields another narrow band centered on 5 THz, which presumably arises from the three-body interaction potential. Like SPC/E, the presence of the surface markedly influences the spectrum of mW. The bulk band at 1 THz is blue-shifted to 2 THz, while the intensity of the band at 5 THz slightly decreases.

The water vibrations on the surface in the region between 2 and 2.5 THz turn out to be of crucial importance as far as G is concerned, as revealed by the frequency-dependent heat flux $q(\omega)$ at the interfaces. Note that the frequency integral of $q(\omega)$ yields the heat flux Q used to calculate G.[28] That quantity was characterized as follows:[28,29]

$$q(\omega) = \frac{2}{A\delta t} \sum_i \left\langle \tilde{F}_i(\omega) \cdot \tilde{v}_i^*(\omega) \right\rangle, \quad (2)$$

where A is the cross-sectional area, δt is the time interval (2 fs here) between two consecutive snapshots, and the quantities in the bracket refer to the Fourier transforms of forces and velocities. The bracket refers to a non-equilibrium average. When the summation is performed on the solid atoms (index i), the force in Eq. (2) is the total force on the i-th solid atom due to the liquid particles. Conversely, the summation may be performed on liquid particles. In this case, the force on the i-th particle arises from interactions with the solid atoms. We show in Fig. 4(a) the variation of $q(\omega)$ for mW and SPC/E with the summation performed on the carbon atoms at $W_{SL} \approx 100$ mJ/m^2. The coupling between both models and the carbon atoms around 2–2.5 THz can clearly be seen. Further coupling between water models and the graphene vibrations between 20 and 40 THz can be observed. The phonon density of states of the graphene layers is reported in Fig. S4 (supplementary material), where it can be seen that substantial density of states comprising the acoustic out-of-plane modes exists in this spectral region. Strikingly, both water models' vibrations couple in a similar way with graphene. This observation explains why G takes similar values for mW and SPC/E at $W_{SL} \approx 100$ mJ/m^2. The strong effect of the water vibrations around 2–2.5 THz on G is even more clearly visible in Fig. 4(b) (red and green curves) where the flux is calculated by performing the summation on the liquid particles in Eq. (2). The curves for $q(\omega)$ for both models are similar, with a slight frequency increase for SPC/E, as discussed above regarding $P(\omega)$. When W_{SL} decreases to $\approx$6 mJ/m^2, the maximum in $q(\omega)$ appears at lower frequencies for both models [Figs. 4(b) and 4(c)]. In this weak wetting regime, the water layer structure has vanished

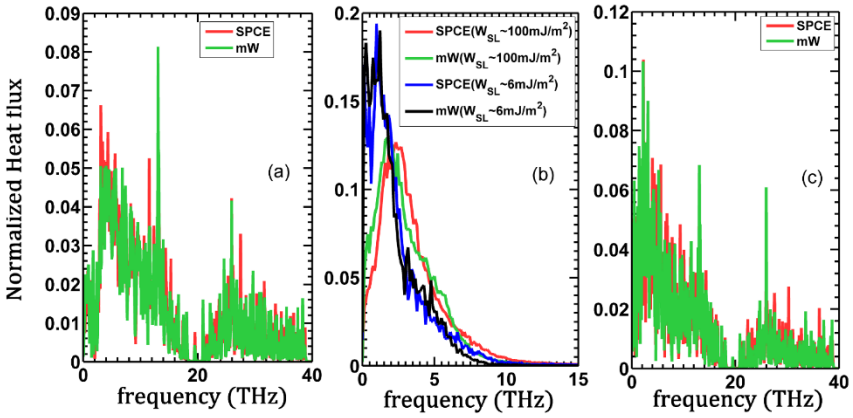

FIG. 4. The normalized frequency-dependent heat flux calculated from the carbon atoms at $W_{SL} \approx 100$ mJ/m^2 and $W_{SL} \approx 6$ mJ/m^2 is presented in (a) and (c), respectively, for SPC/E (red) and mW (green). (b) Normalized frequency-dependent heat flux calculated from water $W_{SL} \approx 100$ mJ/m^2 (red for SPC/E and green for mW) and $W_{SL} \approx 6$ mJ/m^2 (blue for SPC/E and black for mW).

(Fig. 1); the interface then closely resembles a liquid-vapor-like interface. The collisions of the water molecules with the surface occur less frequently than for larger W_{SL} values. The frequency integral of the curves for $q(\omega)$ in Figs. 4(a) and 4(c) reveals that the energy exchange at low frequency vibrations increases as W_{SL} decreases (see Fig. S5 in the supplementary material).

To conclude, the general mechanism that leads G to increase with W_{SL} (Fig. 2) may be summarized as follows. When the interaction between water and graphene increases, the packing of water molecules in the vicinity of the surface is enhanced. From the vibration point of view, tighter packing results in the increase of the frequency of the water translational librations, yielding enhanced coupling with graphene. In turn, the enhanced vibrational coupling between water and graphene yields an increase in G. Even though mW and SPC/E differ in their degrees of freedom, they lead to very similar interfacial water structures on graphene at each value of W_{SL} that covers a broad range from hydrophobic to mildly hydrophilic. This common behavior concerning structure presumably results from the representation of short-range tetrahedral order arising from hydrogen bonds by both models although through different interaction potentials. Water adsorption on the surfaces influences the vibration properties of the models in a comparable way. Owing to the fact that both SPC/E and mW vibration properties behave similarly next to the substrate at all interaction couplings, G increases with W_{SL} in a similar way for both models. Our work demonstrates the close connection between the interfacial liquid structure and Kapitza conductance. Furthermore, it takes a first step in addressing the effect of coarse-graining on interfacial heat transfer by showing that liquid CG models may in fact be able to reproduce the behavior of atomistic models under specific circumstances regarding their structure behavior. Such CG models may prove useful to address the interfacial thermal properties of large-scale systems that are out of reach of atomistic simulations. For the systems considered here, the CG simulations were roughly twice as fast as the atomistic ones with the computation time being strongly influenced by the carbon-carbon interactions.

See supplementary material for information on simulation protocols, system sizes (Sec. I), interaction parameters (Sec. II), details on the evaluation of temperature discontinuities (Secs. III and IV), details on bulk thermal conductivity and heat capacity evaluation (Sec. V), details on power spectrum evaluation (Secs. VI and VII), and cumulative heat flux corresponding to Figs. 4(a) and 4(b) (Sec. VIII).

V.R.A. thanks Professor Dr. Florian Müller-Plathe and Dr. Samy Mérabia for fruitful discussions and Dr. Haoxue Han for useful discussions. This research was funded by the German Research Foundation (DFG) through the SFB TRR 146 Multiscale Simulation Methods for Soft Matter Systems. We acknowledge the HPC Center at TU Darmstadt for computer time on the Lichtenberg Cluster and the John von Neumann Institute for Computing (NIC) at Jülich Supercomputing Center for computer time on JURECA.

[1]A. Balandin, IEEE Spectrum **46**, 34 (2009).
[2]D. Alexeev, J. Chen, J. H. Walther, K. P. Giapis, P. Angelikopoulos, and P. Koumoutsakos, Nano Lett. **15**, 5744 (2015).
[3]B. Ramos-Alvarado, S. Kumar, and G. P. Peterson, J. Phys. Chem. Lett. **7**, 3497 (2016).
[4]S. Merabia, J. Lombard, and A. Alkurdi, Int. J. Heat Mass Transfer **100**, 287 (2016).
[5]N. Shenogina, R. Godawat, P. Keblinski, and S. Garde, Phys. Rev. Lett. **102**, 156101 (2009).
[6]Z. Ge, D. G. Cahill, and P. V. Braun, Phys. Rev. Lett. **96**, 186101 (2006).
[7]H. Acharya, N. J. Mozdzierz, P. Keblinski, and S. Garde, Ind. Eng. Chem. Res. **51**, 1767 (2012).
[8]H. Harikrishna, W. A. Ducker, and S. T. Huxtable, Appl. Phys. Lett. **102**, 251606 (2013).
[9]B. Ramos-Alvarado and S. Kumar, J. Phys. Chem. C **121**, 11380 (2017).
[10]F. Sedlmeier, J. Janecek, C. Sendner, L. Bocquet, R. R. Netz, and D. Horinek, Biointerphases **3**, FC23 (2008).
[11]G. Stirnemann, P. J. Rossky, J. T. Hynes, and D. Laage, Faraday Discuss. **146**, 263 (2010).
[12]R. Evans and M. C. Stewart, J. Phys.: Condens. Matter **27**, 194111 (2015).
[13]S. N. Jamadagni, R. Godawat, and S. Garde, Annu. Rev. Chem. Biomol. Eng. **2**, 147 (2011).
[14]J. Frenkel, in *Kinetic Theory of Liquids*, edited by R. H. Fowler, P. Kapitza, and N. F. Mott (Oxford University Press, 1947).
[15]D. Bolmatov, V. V. Brazhkin, and K. Trachenko, Sci. Rep. **2**, 1 (2012).
[16]V. R. Ardham and F. Leroy, J. Chem. Phys. **147**, 074702 (2017).
[17]H. J. C. Berendsen, J. R. Grigera, and T. P. Straatsma, J. Phys. Chem. **91**, 6269 (1987).
[18]V. Molinero and E. B. Moore, J. Phys. Chem. B **113**, 4008 (2009).
[19]F. H. Stillinger and T. A. Weber, Phys. Rev. B **31**, 5262 (1985).
[20]A. Kozbial, C. Trouba, H. Liu, and L. Li, Langmuir **33**, 959 (2017).
[21]T. Ondarçuhu, V. Thomas, M. Nuñez, E. Dujardin, A. Rahman, C. T. Black, and A. Checco, Sci. Rep. **6**, 24237 (2016).
[22]S. Plimpton, J. Comput. Phys. **117**, 1 (1995).

[23]L. Hu, T. Desai, and P. Keblinski, Phys. Rev. B **83**, 195423 (2011).
[24]M. Zhang, E. Lussetti, L. E. S. de Souza, and F. Müller-Plathe, J. Phys. Chem. B **109**, 15060 (2005).
[25]L. Xue, P. Keblinski, S. R. Phillpot, S. Choi, and J. A. Eastman, J. Chem. Phys. **118**, 337 (2003).
[26]K. Gordiz and A. Henry, New J. Phys. **17**, 103002 (2015).
[27]S. T. Lin, P. K. Maiti, and W. A. Goddard III, J. Phys. Chem. B **114**, 8191 (2010).
[28]K. Sääskilahti, J. Oksanen, J. Tulkki, and S. Volz, Phys. Rev. B **90**, 134312 (2014).
[29]A. Giri, J. L. Braun, and P. E. Hopkins, J. Phys. Chem. C **120**, 24847–24856 (2016).

Supplementary material for the article "Is a coarse-grained model for water sufficient to compute Kapitza conductance on non-polar surfaces?

Vikram Reddy Ardham and Frédéric Leroy*

Eduard-Zintl-Institut für Anorganische und Physikalische Chemie, Technische Universität Darmstadt, Alarich-Weiss-Strasse 8, 64287 Darmstadt, Germany

*v.ardham@theo.chemie.tu-darmstadt.de

I. SIMULATION PARAMETERS

System size and setup

For the thermal interfacial conductance calculations, the systems contained 16000 water molecules and 32256 carbon atoms. The cross-sectional area of the simulation cell was 5.981×6.0434 nm^2. The inlayer graphene interactions were modeled using the optimized Tersoff potential.[1] The parameters given in Ref. [2] were used for the interlayer interactions. Water interacted with the carbon surfaces through the 12-6 Lennard-Jones potential. In the case of SPC/E, only the oxygen-carbon interaction was taken into account. For both SPC/E and mW, the distance parameter of the potential was set to σ_{SL}=0.335 nm. In all cases, the Lennard-Jones forces were truncated beyond 1.3 nm and when electrostatic interactions were present, interactions below 1 nm were evaluated in the real space while the interactions beyond this distance were evaluated in the reciprocal space with a relative accuracy of 10^{-4} using the particle-particle particle-mesh method.[3]

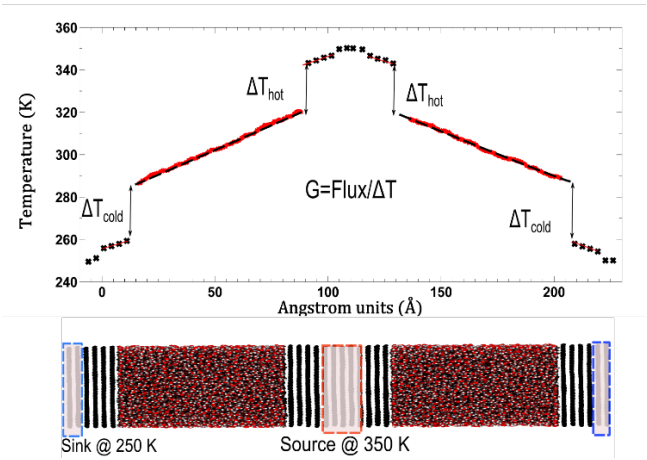

FIG. S1. Simulation setup for measuring the interfacial thermal conductance. Two slabs of liquid are sandwiched between stacks of graphene sheets. The heat source and sink are placed as shown in blue and red, respectively. The resulting temperature spatial variation perpendicular to the interfaces and measurement of the interfacial temperature discontinuities at the hot and cold interfaces are illustrated in the plot above through ΔT_{hot} and ΔT_{cold}, respectively.

Equilibration procedure prior to interfacial thermal conductance calculations

To compute the interfacial thermal conductance, the setup presented in Fig. S1 above was used. A film of liquid of 8000 molecules was first sandwiched between six layers of graphene (1344 atoms each) on each side and equilibrated in at constant number of particles, constant temperature and pressure (NPT) with the Nosé-Hoover thermostat and barostat[4] with the time constants 0.5 ps and 1 ps, respectively. Due to the heterogeneous nature of the system, different temperatures were obtained for the liquid and solid parts. To achieve constant temperature throughout the system, water and graphite were coupled to two separate Berendsen thermostats,[5] both at 300 K. Once equilibrated, the system was duplicated in the z-direction (perpendicular to the interfaces) and further equilibrated at constant volume and temperature (NVT) with a Nosé-Hoover thermostat until temperature was homogenous across the entire system. The equilibration process was typically performed for 1 ns with a timestep of 0.5 fs.

Kapitza Conductance calculations

After equilibration was performed as described above, thermal gradient was applied with the help of heat source and sink (Fig. S1) maintained at 350 K and 250 K, respectively, by means of a Nosé-Hoover thermostat with a time constant of 0.5 ps. The rest of the system was simulated at constant energy and volume (NVE). After steady-state was reached, data was accumulated to obtain the variation of temperature perpendicular to the interfaces throughout the system. Typically, the temperature profiles were constructed through the analysis of trajectories that lasted between 2-5 ns (see Table S1 below). The timestep used was 0.2 fs for all NEMD simulations. The interfacial thermal conductance G was evaluated as the ratio of the flux Q across the interface to the temperature difference ΔT between the substrate and water at the

interfaces through $G=Q/\Delta T$. The heat flux was obtained from the time dependence of the energy which was injected to the heat source and extracted from the sink. The temperature difference was evaluated first by fitting straight lines to the temperature gradient in the non-thermostatted graphene layers and to the temperature gradient in water. Note that the water region in the immediate vicinity of the carbon surfaces was not included in the fits (typically within 0.7 nm from the surface). Then ΔT was evaluated by extrapolating the fits to the surface of the interfacial graphene layer, i.e., at the average height of the carbon atoms of the layer in direct contact with water. This is a choice made because ΔT could be evaluated at any location within the 3-4 ångströms between the substrate and the adsorbed water molecules. We found that there is a weak dependence of G on the extrapolation distance as is shown in Fig. S3. Although G seems to increase with this distance, the variation is comparable with statistical uncertainty. Thus, we only present values of G which were obtained with ΔT measured at the graphene surface. Moreover, these values were obtained by averaging over the four interfaces in the system (Fig. S1). The average values of ΔT at the cold and hot interfaces depending on W_{SL} are given in Table S3. The statistical uncertainties on G were calculated as the standard deviation on the mean through block averaging with a block size of 0.5 ns. The system was simulated for 1.5 ns so that steady state was established. The simulations in steady state were used to collect data for the thermal conductance calculations. The corresponding simulations lengths are given in Table S1 below.

System	Simulations length in steady state
SPC/E	
W_{SL}=6.5 mJ/m^2	2 ns
W_{SL}=16.7 mJ/m^2	2 ns
W_{SL}=40.5 mJ/m^2	2 ns
W_{SL}=59.5 mJ/m^2	2.5 ns
W_{SL}=80.6 mJ/m^2	2.5 ns
W_{SL}=102.6 mJ/m^2	4 ns
mW	
W_{SL}=6.3 mJ/m^2	5.6 ns
W_{SL}=17.1 mJ/m^2	5.6 ns
W_{SL}=42.0 mJ/m^2	5.6 ns
W_{SL}=61.3 mJ/m^2	5.3 ns
W_{SL}=82.6 mJ/m^2	5.3 ns
W_{SL}=104.4 mJ/m^2	5.6 ns

TABLE S1. Simulation lengths for the steady state non-equilibrium simulations with SPC/E and mW. The individual systems are identified through their respective W_{SL} value, which quantifies the water-surface interaction strength.

II. INTERACTION PARAMETERS

The energy parameter ε_{SL} is varied to tune the water-surface interaction strength and assess the effect of this parameter on the Kapitza conductance. Rather than quantifying the solid-liquid interaction through ε_{SL}, this interaction is discussed in terms of W_{SL}. The calculation of W_{SL} depending on ε_{SL} was obtained through thermodynamic integration as detailed in recent publications by us.[6,7] The results of the calculations of W_{SL} together with the range of ε_{SL} values sampled are detailed in Table S2 and Fig. S2. Water and graphite interacted through the 12-6 Lennard-Jones interaction pair potential u_{LJ} following:

$$u_{LJ}(r) = 4\varepsilon_{SL}\left[\left(\frac{\sigma_{SL}}{r}\right)^{12} - \left(\frac{\sigma_{SL}}{r}\right)^{6}\right]$$

where ε_{SL} and σ_{SL} are the energy and distance parameters, respectively. σ_{SL}=0.335 nm for all systems. The solid-liquid work of adhesion W_{SL} was evaluated depending on ε_{SL} using the dry-surface method, which is detailed in our recent works.[8,9]

ε_{SL} / kJ/mol	Model mW W_{SL} / mJ/m^2	Model SPC/E W_{SL} / mJ/m^2
0.0595	6.3	6.5
0.1191	17.1	16.7
0.2382	42.0	40.5
0.3192	61.3	59.5
0.4002	82.6	80.6
0.4764	104.4	102.6

TABLE S2. Lennard-Jones energy parameter for the carbon-water pair interactions and corresponding values of W_{SL} for the mW and SPC/E models. Only the values of W_{SL} at which the interfacial thermal conductance was calculated are given.

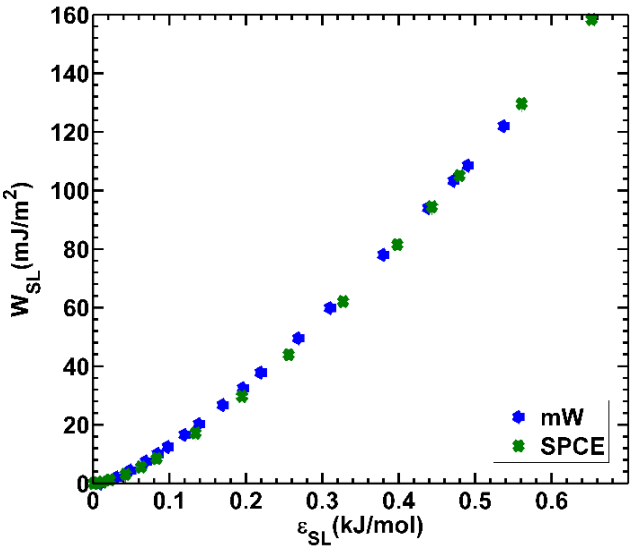

FIG. S2. Dependence of W_{SL} on ε_{SL} for the water models SPC/E (green) and mW (blue) models.

III. INTERFACIAL THERMAL CONDUCTANCE DEPENDING ON THE LOCATION AT WHICH ΔT IS MEASURED

The temperature difference between water and the graphene surface at the interface was measured depending on the distance *dx* from the average height of the top graphene layer. Consequently, the interfacial heat conductance *G* depends on dx.

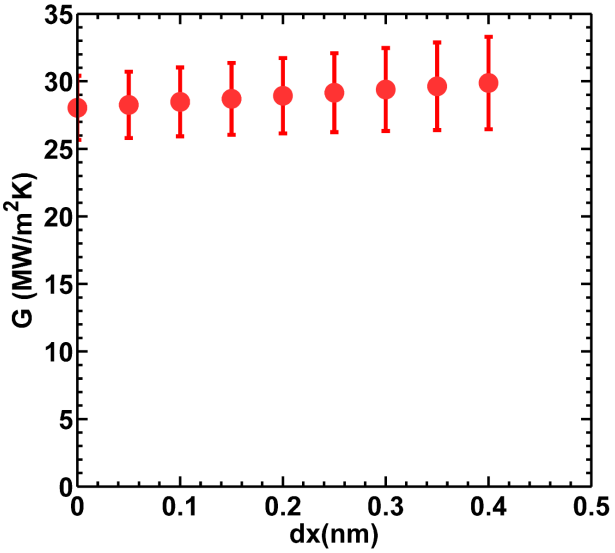

FIG. S3. Interfacial thermal conductance for SPC/E at W_{SL}≈100mJ/m^2 depending on the location where the temperature drop was measured. The quantity dx is the distance from the mean surface location. All the values presented in the manuscript were evaluated at *dx*=0.

IV. INTERFACIAL TEMPERATURE DISCONTINUITIES

SPC/E			mW		
W_{SL} / mJ/m^2	ΔT_{cold} / K	ΔT_{hot} / K	W_{SL} / mJ/m^2	ΔT_{cold} / K	ΔT_{hot} / K
6.3	47.3(2.2)	44.2(2.3)	6.5	48.0(2.8)	42.5(2.3)
17.1	42.9(2.2)	38.5(1.6)	16.7	43.6(0.9)	37.9(1.3)
42.0	37.0(1.1)	36.6(1.3)	40.5	36.5(1.0)	31.6(2.4)
61.3	36.0(1.4)	32.0(0.3)	59.5	32.8(1.0)	30.4(1.3)
82.6	33.9(2.1)	30.6(2.2)	80.6	32.1(1.0)	27.2(1.1)
104.4	32.8(1.2)	26.9(1.5)	102.6	30.4(1.7)	26.4(1.0)

TABLE S3. Average values of ΔT at the cold and hot interfaces for the calculations of G for SPC/E and mW.

V. BULK PROPERTIES

Isobaric heat capacity

The isobaric heat capacity, C_p is calculated by performing simulations in the NPT ensemble following:

$$C_p = \frac{\langle H \rangle^2 - \langle H^2 \rangle}{k_B T^2}$$

where H is the enthalpy, k_B the Boltzmann constant and T the temperature. The system consisted of 2048 water molecules. The simulations used a Nosé-Hoover thermostat and barostat with a time constant of 1ps, with a timestep of 1 fs for a total of 2ns.

Bulk thermal conductivity

The same setup used above to calculate specific heat capacity is used to compute the thermal conductivity. The equilibrated system above is then fixed at constant volume and a source and

sink are attached in the center and edge of the simulation box in the z-direction at 325 K and 275K respectively. A timestep of 0.1 fs was used and the rest of the system was simulated at constant energy (NVE). The temperature profiles are extracted during a 2ns simulation run. The thermal conductivity k is computed following Fourier law as the ratio of the net heat flux J_Q to the temperature gradient ∇T in the flux direction, following:

$$k = \frac{J_Q}{|\nabla T|}$$

VI. VIBRATION SPECTRUM OF BULK AND ADSORBED WATER

To evaluate the power spectrum of the adsorbed layer on the graphite surface (Eq. (1) of the manuscript), velocities of only the atoms within the first layer (within $2^{1/6}\ \sigma_{SL}$) are taken into account. Since, the atoms keep on adsorbing and desorbing the time-series obtained for the velocities is not continuous. To solve this problem, one can either use the traditional DFT [discrete Fourier transform without fast Fourier Transform (FFT)] and evaluate intensities at different frequencies or one can obtain the time-series as it is, split it into different windows when it is adsorbed (and ignoring when desorbed) and pad zeros at the end and finally apply the regular FFT. It was found that both methods result in no significant differences and the plots presented are using the later method as it uses efficient FFT.

VII. PHONON DENSITY OF STATES OF FEW-LAYER GRAPHENE

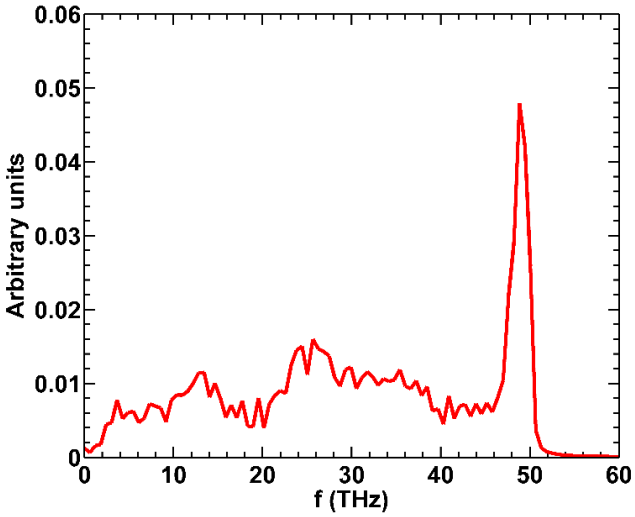

FIG. S4. Phonon density of state of graphene with 8 carbon layers. The spectrum was obtained through the Fourier transform of the velocity auto-correlation function. The quantity *f* on the x-axis is frequency.

VIII. CUMULATIVE HEAT FLUX

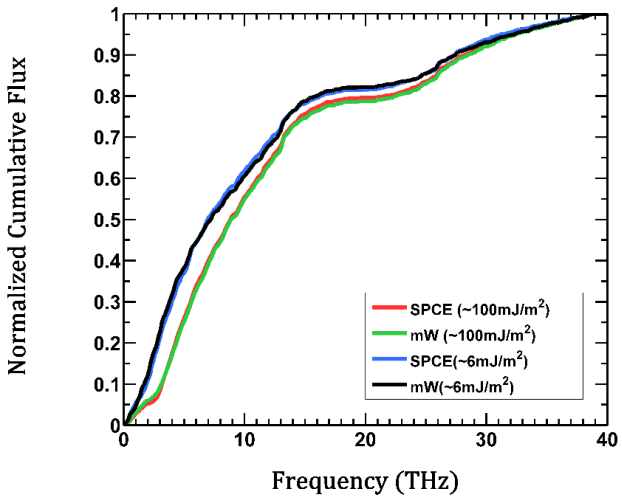

FIG. S5. Normalized cumulative heat-flux is shown for the graphite atoms at two wetting extrema.

REFERENCES

[1] L. Lindsay and D.A. Broido, Phys. Rev. B **81**, 205441 (2010).

[2] L.A. Girifalco, M. Hodak, and R.S. Lee, Phys. Rev. B **62**, 13104 (2000).

[3] R.W. Hockney and J.W. Eastwood, Bristol: Hilger (1988).

[4] W.G. Hoover, Phys. Rev. A **31**, 1695 (1985).

[5] H.J.C. Berendsen, J.P.M. Postma, W.F. van Gunsteren, A. DiNola, and J.R. Haak, J. Chem. Phys. **81**, 3684 (1984).

[6] V.R. Ardham and F. Leroy, J. Chem. Phys. **147**, 74702 (2017).

[7] F. Leroy, S. Liu, and J. Zhang, J. Phys. Chem. C **119**, 28470 (2015).

[8] F. Leroy and F. Müller-Plathe, Langmuir **31**, 8335 (2015).

[9] V.R. Ardham, G. Deichmann, N.F.A. van der Vegt, and F. Leroy, J. Chem. Phys. **143**, 243135 (2015).

CHAPTER # 6

Conclusions and Outlook

Polymer nanocomposites are of considerable interest as they offer significant improvement in physical properties over conventional materials and at the same time provide flexibility and control. These composite systems consist of a very high density of polymer-nanoparticle interfaces. These interfaces are key to determining the transport properties in these systems. A closer look at these interfaces using molecular simulations can enhance our understanding of the interfacial physics in action.

However, simulating multiphase systems is not straightforward, as a subtle balance of interaction strengths between the various species must be maintained. In addition, heterogeneities in composite systems span many length scales and simulating them using the simplest atomistic models is computationally out of reach. In this thesis, both the above problems are addressed by studying in detail the interfacial thermodynamics, the influence of coarse-graining on the interfacial free energy. Further, a simple approach was developed to accurately model graphene particles adsorbing at the water-oil interface. Coarse-graining results in loss of degrees of freedom, which means that thermal properties like heat capacity and thermal conductivity cannot be directly reproduced. However, it was not yet known, how the loss of information with coarse-graining influences heat transfer across interfaces. We took a first step in this direction by studying heat transfer and its mechanisms across water-graphitic systems using atomistic and coarse-grained models of water. We observed that, removal of certain degrees of freedom is not very relevant for the heat transfer as long as the interfacial layered structuring and wetting strengths are maintained.

These are certainly fundamental insights into interfacial thermodynamics, coarse-graining, heat-transfer, and multi-scale modeling. Through our study we have learnt that, to represent a solid-liquid interface accurately, it is not enough to simply reproduce the solid-liquid interaction energy but also its fluctuations must be reproduced. These fluctuations in the solid-liquid interaction energy are found to be very crucial, and this information in fluctuations which corresponds to the entropy, is lost when coarse-graining is performed. We further learnt that, macroscopic wetting coefficient could be used as a reasonable criterion to predict adsorption of particles as thin as graphene monolayer at liquid-liquid interfaces. This due to the short-ranged nature of the VdW interactions dominating these systems. In addition, coarse-graining the liquid was found to provide accelerated dynamics when it comes to graphene particle diffusion which is very useful in obtaining equilibrated structures of complex networks of graphene at the water-oil interface.

Since majority of the resistance to heat occurs at the interface, it is very crucial to understand the corresponding changes when the liquid is coarse-grained. We take a first stride in this direction by delving deeper into the mechanisms of heat transfer across water-graphitic systems. We observed that

wetting strength and the liquid layering at the interface are crucial in determining heat transfer across solid liquid interfaces. Therefore, by combining all the insights gained in the detailed studies performed in this thesis, one has enough knowledge and a sufficient tool kit to perform large scale simulations of two-dimensional graphene particle networks and characterize heat transfer through these networks.

A viable approach in this direction could be, to first create a network of graphene particles at the water-oil interface with a large interfacial area (up to 100 nm) at the coarse-grained resolution. After a network of particles is well equilibrated, atomistic details could be back-mapped into the coarse-grained liquid models. The back-mapping often results in quick equilibration of atomistic configurations. Now, a detailed understanding of the heat transfer could be made by performing non-equilibrium molecular dynamics simulations. Interesting aspects like, connectivity within the particle network, heat exchange across neighboring graphene sheets, corresponding fluctuations, structure of the particle-particle, particle liquid interfaces can be studied in detail. Alternatively, as we now found out that heat transfer across water-graphene is immune to water coarse-graining, heat transfer in the above network could in fact be characterized at the coarse-grained level. This however, requires that heat transfer across *n*-hexane-graphene interface be immune to the resolution of *n*-hexane model, which could be a topic of further investigation as well. In case the conclusions drawn for water-graphene interfaces are not equally applicable to liquids consisting of longer chains, one could try to implement methods by adding additional implicit degrees of freedom, for instance, by using the Dynamics with Implicit Degrees of freedom (DID) method. In this method, mesoparticles are phenomenologically assigned additional implicit degrees of freedom that are allowed to exchange heat with the external degrees of freedom. This approach could mitigate the problem and correctly reproduce the interfacial heat transfer. This method, however has been only applied to bulk systems but could be easily extended to interfacial systems.

On the other hand, the approach developed here could be used to derive coarse-grained models and extensive studies could be possibly made to study the role of graphene particle size distribution on the network formation, to understand the structure and formation of so called Pickering emulsions that are formed when nanoparticles assemble at the interface formed by droplets of water in oil (or oil in water), to study the influence of functionalization of graphene on the structure of the assembly, the corresponding heat transfer, just to mention a few interesting problems.

The studies performed in this thesis open a wide venue for several new, exciting studies to substantially improve our understanding of the self-assembly and thermal transport in graphene-based nanocomposites. The insights gained could in principle be applied not just to graphene but also to other nanoparticle inclusions like metals, semiconductors, low dimensional metal dichalcogenides as well.

In addition, the insights the thesis provides should be able to assist in developing coarse-grained models for heterogenous systems, as the essential ingredients about the equilibrium and dynamics properties are made available. For instance, liquid coarse-models that reproduce accurately the wetting strength, layered structure and the fluctuations in the interaction energy will be very good choices to model systems consisting of high density of solid-liquid interfaces. Below a rough roadmap is laid out to guide future studies using the insights gained in the thesis.

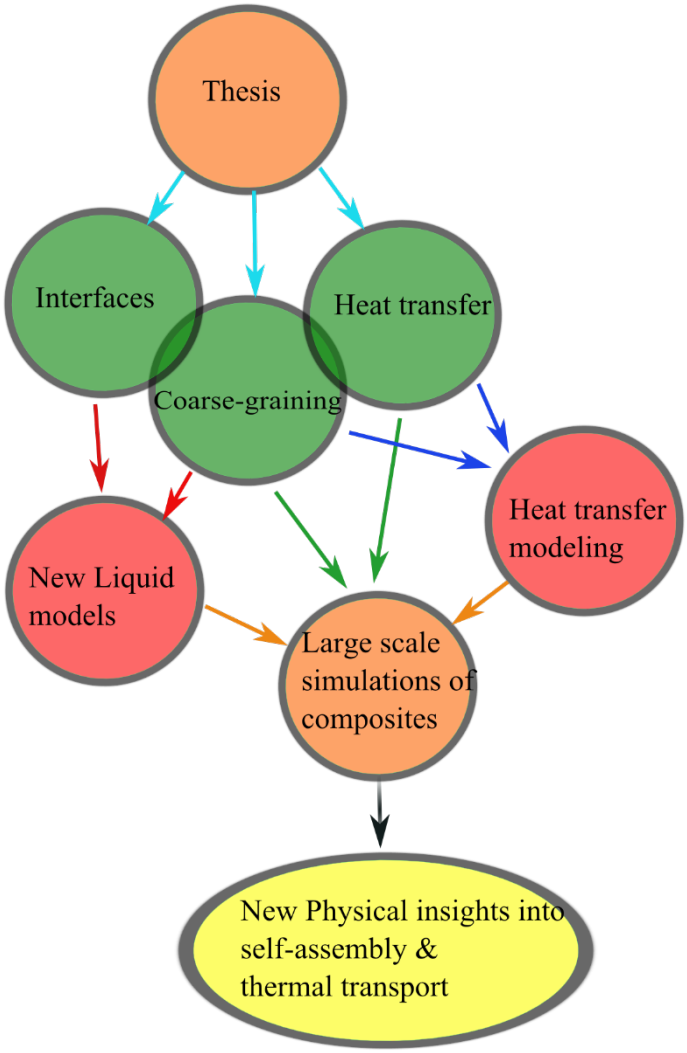

Figure 3. Possible road map for further investigations

Acknowledgements

I would like to extend my sincere gratitude to my supervisor P. D. Dr. Frédéric Leroy, who has supported me all along. His constant motivation has driven me to successfully completing this thesis and along the way I learnt numerous things, not just related to science. I am extremely indebted to him for extending his support while I was sick during my first year of PhD. He constantly inspired me to stick to only the highest scientific standards and I hope to continue doing the same throughout my career.

I cannot thank enough my co-supervisor Prof. Florian Müller-Plathe for his relentless support throughout my stay in his group. He provided all the support and resources I need, without which I could not possibly have a taken a single step in completing my thesis. I have learnt great many things directly through our discussions and through interacting with the current and former members of his group. I sincerely thank him for getting rid of all the bureaucratic hurdles and making sure that I graduate without directing my efforts towards any administrative ordeals. I only wish I could have had more scientific discussions with him during my stay.

My stay in Darmstadt would not have been complete without Prof. Nico van der Vegt and his friendly group. He often mentioned me as his adopted group member, although he said that tongue in cheek, he really treated me as his own group member and his door was always open for me. His scientific enthusiasm has always been very contagious. I thoroughly enjoyed our discussions which included both scientific and non-scientific ones (but never unscientific). I whole-heartedly thank him for his constant support and inspiration.

I thank Prof. Michael Böhm who has always shown great interest in my progress. I believe he is genuinely a nice person and cared about the well-being of people around him. Unfortunately, we did not have a lot of discussions on science, but I always enjoyed our discussions on movies and food. I also would like to thank, Ms. Dana Voss, the wonderful secretary of our group. I really don't think I will come across someone else who is good as she is at what she does. She is both professional and friendly and I thank her a million times for organizing all the group dinners, trips and other events.

Last but not the least, I am very glad to have had very friendly, motivating, and egregious colleagues. I would like to personally thank Dr. Divya Nayar, David Rosenberger, Dr. Francisco Rodriguez-Ropero, Dr. Shenguian Liu, Dr. Kenkoh Endoh, Jurek Schneider, Andreas Kalogirou, Gustavo Garcia-Rondina, Dr. Hari Krishna Chilukoti, Dr. Mashid Rahimi, Prof. Kaustubh Rane, Marvin Bernhardt, Dr. Susana Figueroa-Gesternmaier, Dr. Yang Biao, Dr. Jianguo Zhang, Dr. Donatas Surblys, Yunfeng Mao, Prof. Hong Liu, Dr. Cahit Dalgicdar, Prof. Hossein Eslami, Angelina Folberth, Dr. Haoxue Han and others.

Curriculum Vitae

Name	:	Vikram Reddy Ardham
Place of Birth	:	Nalgonda (Republic of India)
Date of Birth	:	21st May 1990
Nationality	:	Indian

Education

2007-2011	Indian Institute of Technology Roorkee, India (B. Tech in Chemical Eng.)
2011-2013	University at Buffalo, USA (M.S in Chemical Eng.)
2014-2018	Ph.D candidate, Dept. of Chemistry, Technical University of Darmstadt

_____

(Vikram Reddy Ardham)

3/27/2018,

Darmstadt,

Vikram Reddy Ardham

Heinrichstrasse 195

64287 Darmstadt

Erklärung

Ich erkläre hiermit, noch keinen Promotionsversuch unternommen zu haben.

_____

(Vikram Reddy Ardham)

3/27/2018,

Darmstadt,

Vikram Reddy Ardham

Heinrichstrasse 195

64287 Darmstadt

Eidesstattliche Erklärung

Ich erkläre hiermit, dass ich meine Dissertation selbstständig und nur mit den angegebenen Hilfsmitteln angefertigt habe.

Das in *Chapter #2* verwendete *CRW Force-field* wurde von Gregor Deichmann, einem Doktoranden der Arbeitsgruppe von Prof. Dr. N. F. A. van der Vegt (Eduard-Zintl-Institut für Physikalische Chemie, Technische Universität Darmstadt) zur Verfügung gestellt, worauf ich hiermit ausdrücklich hinweise.

_____

(Vikram Reddy Ardham)